PhD Thesis

Super- and Subradiance of Quantum Dots by Photon-Mediated Coupling

Vasiliki Angelopoulou

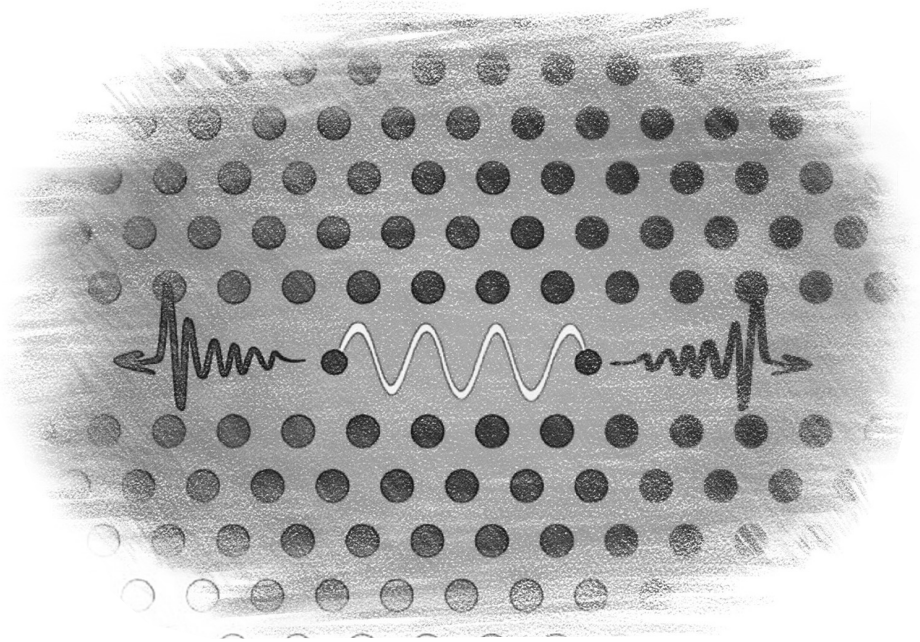

December 2023

Super- and Subradiance of Quantum Dots by Photon-Mediated Coupling

Vasiliki Angelopoulou

Supervisors:
Prof. Peter Lodahl
Junior Prof. Alexey Tiranov
Dr. Cornelis Jacobus van Diepen

UNIVERSITY OF
COPENHAGEN

Quantum Photonics
Center for Hybrid Quantum Networks
The Niels Bohr Institute

This thesis has been submitted to the PhD School of the Faculty of Science,
University of Copenhagen

Abstract

Large-scale entangled quantum states of multiple photons are considered a promising resource for measurement-based quantum computing and long-range quantum communication. Quantum emitters have proven to be a powerful tool as deterministic single-photon sources. By implementing spin inside such an emitter and applying the appropriate driving sequence, one can create a spin-photon interface capable of generating a one-dimensional entangled chain of photonic qubits. However, for a universal quantum computing resource, more complex structures are required. One approach to scaling up to higher dimensions, allowing for improved tolerance to qubit losses, involves coupling multiple emitters to create a highly entangled photon state up front. Here, we present the first demonstration of photon-mediated coupling between solid-state quantum dots.

Direct signatures of coupling between self-assembled quantum dots have been challenging to observe, primarily due to inhomogeneities in their emission frequencies and position, along with their susceptibility to decoherences from the environment. In the present work, we use InAs quantum dots embedded in a GaAs photonic crystal waveguide. The waveguide effectively extends the range of the dipole-dipole interaction, mitigating the spatial limitation. From transmission measurement of the nanophotonic device, we select three quantum dots well coupled to the mode of the shared waveguide, and spectrally close to each other. By applying an out-of-plane magnetic field, we tune the quantum dots into resonance, pairwise. The interaction between the pairs is induced by their coupling to the local polarization of the waveguide mode.

Under these conditions, the investigation of the coupling between the quantum dots is enabled. By driving a single emitter of a pair with resonant optical pulses, we observe the modification of its lifetime when the two emitters are tuned to resonance. The exhibited fast Γ_+, and slow Γ_-, components of the decay stem from the super- and subradiant collective emission from the coupled system. The ratio between the two decay rates, equal to $\Gamma_+/\Gamma_- = 4.8$ for one of the pairs, constitutes a figure of merit of the coupling strength, and is strongly sensitive to decoherences and imperfections. We further probe the coherent evolution of the collective states for a range of detunings between the emitters, and identify a predominantly dissipative coupling. Our results are in good agreement with numerical simulations conducted based on the theory developed for the present work.

By means of different excitation conditions, we additionally explore the controlled preparation of the initial collective state. We drive the system collectively and utilize the polarization of the excitation beam as the enabling parameter to impose a relative driving phase between the two emitters. We

propose to exploit this method to selectively populate the super- and subradiant states on demand.

The system is finally probed with second-order correlation measurements under coherent and continuous drive. Contrary to previous works, we drive one quantum dot of the indistinguishable pair and observe an anti-dip of $g^{(2)}(0) = 0.94$ in the photon-coincidences, along with a broadening of the single-emitter dip. We suggest that, in the single-emitter excitation scheme, the presence of the anti-dip serves as a clear indicator of coupling through the waveguide mode and can be directly associated with superradiance. The broadening of the dip, on the other hand, is attributed to the decay of the longer-lived subradiant state. These interpretations are further supported by numerical simulations.

Our work constitutes a first demonstration of coupling between distant quantum dots and lays the foundation for deterministic entanglement generation through collective excitation of the emitters.

Sammenfatning

Store sammenfiltrede kvantetilstande med flere fotoner er udset til at være en lovende resurse til en målingsbaseret kvantecomputer og langdistance kvantekommunikation. Kvantelyskilder har vist sig at være et vigtigt værktøj som deterministiske enkeltfotonkilder. Ved at implementere et spin i sådan en lyskilde, og ved anvendelse af en passende sekvens af drivsignaler, er det muligt at skabe en spin-foton grænseflade, som er i stand til at generere en endimensionel sammenfiltret kæde af fotoniske qubits. Imidlertid kræves der mere komplekse strukturer, for at have en resurse til en universel kvantecomputer. En måde at skalere op til højere dimensioner, som tillader en forbedret modstandsdygtighed mod tab af qubits, involverer kobling af flere lyskilder for at generere en særligt sammenfiltret fotonisk tilstand fra starten. Her præsenterer vi den første demonstration af fotonformidlet kobling mellem faststofkvantepunkter.

Direkte signaturer af koblingen mellem selvsamlende kvantepunker har været vanskelige at observere, primært grundet forskelle i deres emissionsfrekvenser og position, samt deres følsomhed for inkohærens fra omgivelserne. I denne afhandling bruger vi InAs kvantepunkter indlejret i GaAs en fotonisk krystal-bølgeleder. I praksis forlænger bølgelederen rækkevidden af dipol-dipol interaktionen, hvorved den omgår de rumlige begrænsninger. Fra transmissionsmålinger af den nanofotoniske struktur vælger vi tre kvantepunkter som alle er velkoblede til modet af deres fælles bølgeleder, og som er spektralt tæt på hinanden. Ved at benytte et ude-af-planet magnetfelt, kan vi bringe kvantepunkterne parvist i resonans. Interaktionen mellem parrene er induceret af deres kobling til den lokale polarisering af bølgelederens mode.

Under disse forhold er det muligt at studere af koblingen mellem kvantepunktern. Ved at drive en enkelt af lyskilderne i parret med resonante optiske pulser, observerer vi ændringer i levetiden, når også de to lyskilder er i resonans. De udviste hurtige Γ_+, og langsomme Γ_- komponenter af henfaldet stammer fra super- og subudstråling fra den kollektive emission fra det koblede system. Forholdet mellem de to henfaldsrater, som er lig $\Gamma_+/\Gamma_- = 4.8$ for det ene par, konstituere et mål for koblingsstyken, og er særligt sensitiv til inkohærens og ufuldkommenheder. Vi måler også den kohærente udvikling af de kollektive tilstande for en række detuninger mellem lyskilderne, og identificere in overvægt af dissipativ kobling. Vores resultater er i god overensstemmelse med numeriske simuleringer, som er baseret på teorien der er udledt i forbindelse med det præsenterede værk.

Ved brug af forskellige betingelser for exciteringen undersøger vi også den kontrollerede forberedelse af den oprindelige kollektive tilstand. Vi driver systemet kollektivt og benytter polariseringen af excitationsstrålen, som den aktiverende parameter til at pålægge en relativ fase mellem de to

lyskilder. Vi foreslår at tage gavn af denne metode til selektivt at okkupere den super- og subudstrålende tilstand på kommando.

Endeligt er systemet undersøgt med anden-ordens korrelationsmålinger under kohærent og kontinuert drev. I modsætning til tidligere værker, driver vi én af kvantepunkterne af det identiske par. Vi observerer et anti-dyk af $g^{(2)}(0) = 0.94$ i fotonsammenfaldene og en udvidelse af enkelt-lyskilde dykket. Vi foreslår, at i enkelt-lyskilde excitations tilfældet, er tilstedeværelsen af et anti-dyk en klar indikator for kobling gennem bølgeledermodet. Anti-dykket kan associeres direkte med superudstråling, mens udvidelsen af dykket tilskrives til

henfaldsraten af den længere-levende subudstrålingstilstand. Disse fortolkninger er yderligere understøttet af numeriske simuleringer.

Vores værk konstituerer en første demonstration af kobling mellem fjerne kvantepunkter og lægger fundamentet for deterministisk fremstilling af sammenfiltring gennem kollektiv excitation af lyskilderne.

Acknowledgments

Looking back over the past three and little more years of the PhD, there are many things that make me grateful for taking on this journey in the Quantum Photonics group at the Niels Bohr Institute. During this time, I had the chance to deepen my understanding on quantum optics, to work along side great minds, to be part of a team that knows well how to collaborate, help and respect each other, to learned how to present my work and to grow as a person.

For this experience, I would like to start by thanking my supervisor, Peter Lodahl, for giving me the opportunity to pursue my PhD within his team of experts. His scientific input to this project together with his enthusiasm about the future of quantum in the real world have been inspirational. Peter, thank you also for having the empathy to know when to encourage me to do more and for your understanding and patience when it was most needed. Next, I would like to thank Anders Søndberg Sørensen, our theory Professor. Anders, your insightful guidance on the experiments steered the work always to the right, challenging and exciting direction. Thank you for always having your door open for questions and long physics discussions. Your quotes over these past three years will be kept alive. Thank you also for your other role as the mindful and attentive section leader of the Quantum Optics. Finally, thank you for your genuine enthusiasm on pure fundamental physics! It kept on reminding me why I embarked on this journey in the first place.

I would also like to thank my two closest supervisors and lab comrades. Alexey Tiranov and Cornelis Jacobus van Diepen (Sjaak), it has been a pleasure to have worked with such bright, capable, curious and thorough researchers. To Alexey, thank you for teaching me literally everything about quantum dots at the start of my PhD. Your persistence and confidence as a researcher have been an example to me. Thank you for helping me process this entire project and for your support and guidance moving forward. To Sjaak, thank you for being my everyday lab-mate the past two years. It has been a great pleasure to have shared together all the low days -of bad SNR no matter the beam-walking, pulsed lasers being unstable and bidding early farewell to the beloved twins-BigSis sample- along with a few motivating and illuminating ones in our dark HyQ lab. Thank you for your heartwarming support, your encouragement, for showing me actively and by example how to be a complete researcher and for being open to discuss anything that came along the way. I would also like to thank Xiao-Liu Chu for all the help during the few first months we overlapped in the group, and for continuing to be present for questions and brainstorming even after she left the group.

The thesis would not have been possible without the magical B15027

wafer material grown by Sven Scholz, in the group of Arne Ludwig and Andreas Wieck, in the University of Bochum. I would also like to thank Dorte Christiane Garde Nielsen for always helping with any administrative, bureaucratic or technical matter in the most efficient and comforting way.

The experience of the PhD is owed in great part to the shared everyday life with the Quantum Photonics team and the HyQ cluster. It should not be taken for granted, the thoughtful and solidarity-driven environment that the group has built, together with the active involvement in pressing global issues, extending beyond the realm of physics. I would like to thank wholeheartedly Ying Wang, my office companion. Ying, thank you for your presence, your friendship and for sharing life till late hours inside the office and out. Your strength and perpetual caring spirit are truly inspiring. To Patrik Isene Sund, thank you for the breaks in Fælledparken with all kinds of discussions. I am glad we started our PhD quests together and shared the struggles and small wins along the way . To Oliver August Dall'Alba Sandberg, thank you for your care and your music, for your encouragement at the low and the high points and the much needed walks. Thank you Camille Pappon for always being present with heartwarming words and advice in our conversations. A big thank you to Thibault Capelle for the shared visions and triggering discussions, to Ming Lai Chan for your honesty and your inspirational diligent work, to Martin Hayhurst Appel for never running out of exciting ideas, for the exchange of music and the photo-walks, to Evi Aspropotamiti for singing together has always been a great escape, to Eva Maria Gonzalez Ruiz for your lively presence in the office and your motivating way of working, to Yijian Meng for persuading me to learn Danish and for the laughter we shared, to Nils Hauff for the lab days with music and your openness from the very beginning, to Leonardo Midolo for being a constant of knowledge and always willing to help, to Stefano Paesani for discovering together the nanostructure that filled the pages of this thesis and for the Ettore-visits in NBI, to Shikai Liu for your motivating persistence, to Celeste Qvotrup for being so resourceful with facts and my pull-up role-model, to Carlos Faubry for your soothing guitar playing in the lounge, to Kasper Nielsen for always being up for a common activity and for never running out of hiking tips, to Mikkel Mikkelsen for being a voice of sanity and comfort, to Markus Albrechtsen for lightening any discussion with his sense of humor and for the fuel in the form of candy during the writing, to Teresa Klara Pfau for making everyone feel included and to Zhe Liu for introducing me to fabrication and for your patience and kindness. My old and new office mates, Ying, Eva, Ming Lai, Johann Sebastian Kollath-Bonig, Evi, Celeste and Yu Meng thank you for always making it a welcoming space (with or without a second-hand couch). A big thank you goes also to the cycling team; Rodrigo A. Thomas, Lucio Stefan, Hanna Krystyna Salamon and Sjaak. Exploring the parts of Sjælland and my cycling limits has truly been a mindset changer. Looking forward to all the rides to come. Thank you to Ying, Ming-Lai, Sjaak, Alexey, Anders and Peter for feedback on this thesis and to Kasper for translating my abstract to Danish.

During the last year, I had a unique chance to visit the group of Rob

Thew in the University of Geneva. Thank you Rob for taking me in and for helping me integrate from day-one. My warm thanks to Alberto Rolandi and Pavel Sekatski for reviving my enthusiasm about the project with debates about their theory ideas. To Tiff, Patrik, Joe, Dmitry, Lorentzo, Towsif, Maria and the rest of the GAP team, a big thank you for making me feel part of the crew.

The PhD is a unique process for each one and can easily become a lonely journey. I am deeply happy and grateful for having people (and a dog) in my life that filled the days with music, laughter, trips, dreaming ahead and meaningful conversations. To Vaggelis thank you for dragging me out of my hole to listen to your music, for your genuine care and for lightening the heavy days. Oresti thank you for your mindfulness, for knowing what was needed and how to keep me moving forward. Bea, thank you for being present every time, for the thoughtful calls, the long recordings, for your understanding and support and the conversations over what's important in life. For always having that hike ahead of us. Giorgo, I am very lucky that I met you. Thank you for reminding me what is real and what matters, for the existential conversations, for your company that gave me a horizon to look forward to. To my family-by-choice in Copenhagen and in Greece; Myrto, thank you for your tireless and warmest support. Your kindness, the sharing of all emotions, thoughts and experiences with you, raised me up in moments I thought I couldn't. Pavlina, your love and care made me feel at home even at the most bumpy parts of this way. Your strength and will to change what needs to evolve, have been an inspiration to me. To Eleni and Kallia, thank you for being my pillars back home. I can not wait for the five of us to finally meet again soon. Chris and Lefteri, thank you for roasting me about my PhD life every now and then and for being a solid backing when you knew I needed it. And of course Vaughne, thank you for being the genuine, naive and loving soul you are. You were my stress-release every single time we met. To my mother, father and brother, you are my roots. Thank you for your unconditional love, your constant presence, your undoubted support, your endless patience and unwavering faith in me. I look up to you and love you deeply.

List of publications

The articles published during this thesis are listed in chronological order.

Journal publications

A X.-L. Chu, V. Angelopoulou, P. Lodahl, & N. Rotenberg, **"Subradiant states for two imperfect quantum emitters coupled by a nanophotonic waveguide"** Phys. Rev. A 106, 053702, (2022)

B A. Tiranov, V. Angelopoulou, C.J. van Diepen, B. Schrinski, O.A. Dall'Alba Sandberg, Y. Wang , L. Midolo, S. Scholz, A. D. Wieck, A. Ludwig, A. Søndberg Sørensen & P. Lodahl, **"Collective super- and subradiant dynamics betweendistant optical quantum emitters"** Science 379, 389–393, (2023)

In preparation

C C.J. van Diepen, V. Angelopoulou, A. Tiranov, A. Ahmad, O.A. Dall'Alba Sandberg, Y. Wang, L. Midolo, S. Scholz, A. D. Wieck, A. Ludwig, A. Søndberg Sørensen & P. Lodahl, **"Anti-dip in photon coincidences from coupled quantum dots"**

D A. Rolandi, V. Angelopoulou, C.J. van Diepen, A. Tiranov, Y. Wang, L. Midolo, S. Scholz, A. D. Wieck, A. Ludwig, P. Lodahl, A. Søndberg Sørensen & P. Sekatski **"A minimalistic proof of entanglement between quantum dots"**

Conferences

E V. Angelopoulou, A. Tiranov, C.J. van Diepen, B. Schrinski, O.A. Dall'Alba Sandberg, Y. Wang L. Midolo, S. Scholz, A. D. Wieck, A. Ludwig, A. Søndberg Sørensen & P. Lodahl, **"Coherent super- and subradiant dynamics between distant optical quantum emitters"** (Poster), ICIQP Copenhagen, 2022

F V. Angelopoulou, A. Tiranov, C.J. van Diepen, B. Schrinski, O.A. Dall'Alba Sandberg, Y. Wang L. Midolo, S. Scholz, A. D. Wieck, A. Ludwig, A. Søndberg Sørensen & P. Lodahl, **"Super- and subradiant quantum dynamics between pairs of solid-state optical emitters"** , CLEO San José, May 2023

Spring school

G Poster presentation, **Doctoral Training: Quantum Information Spring School-Near term quantum processors and simulators**, Les Houches Physics School, May 2022

Seminar talks

H **"Collective dynamics between distant optical quantum emitters"**, Annual DNRF meeting, January 2023

I **"Interactions between distant optical quantum emitters: from quantum dots in nanostructures to collective dynamics"**, Université de Genève, March 2023

Outreach

J **"Physicists criticize University of Copenhagen's new NATO ties"** Uniavisen

K **"Danish quantum physicists make nanoscopic advance of colossal significance"** Video-KU

L **"Ph.D. Profiles"** Kvinderifysik

Contents

Abstract iii

Sammenfatning v

Acknowledgments vii

List of publications xiii

Multi-emitter coupling for scalable quantum-information processing 1

1 Theory of collective dynamics 7
1.1 Introduction to super- and subradiance . . . 7
1.2 The Dicke model . . . 11
1.2.1 Superradiance in a dense atomic ensemble . . . 11
1.2.2 Two-atom collective emission . . . 14
1.3 Dissipative and dispersive coupling regimes . . . 17
1.4 Collective dynamics of two emitters in a waveguide . . . 21
1.5 Summary and Connection . . . 25

2 Experimental setup and equipment 27
2.1 Quantum dots in a photonic crystal waveguide . . . 27
2.1.1 The self-assembled quantum dot . . . 27
2.1.1.1 Optical excitation schemes . . . 29
2.1.1.2 The neutral exciton . . . 29
2.1.2 Light-matter interaction in a photonic crystal waveguide . . . 30
2.1.2.1 Spontaneous emission of a two-level system . 30
2.1.2.2 Photonic crystal waveguide . . . 31
2.1.3 Sample . . . 33
2.1.3.1 Sample growth . . . 33
2.1.3.2 Photonic chip fabrication . . . 34
2.2 Optical setup . . . 35
2.3 Excitation techniques . . . 37
2.4 Excitation lasers . . . 38
2.5 Filter boards . . . 39
2.6 Detectors . . . 40
2.7 Summary and Connection . . . 41

3 Optical Spectroscopy **43**
3.1 Identifying the emitters in resonant transmission 43
3.2 Charge plateaus 47
3.3 Magnetic field as the tuning knob 48
3.3.1 Out-of-plane magnetic field on a neutral exciton 48
3.3.2 Tuning pairs of quantum dots to resonance 49
3.4 Resonant fluorescence 51
3.5 Imaging the quantum dots 52
3.6 Parameter summary 54
3.7 Summary and Connection 54

4 Collective dynamics of two coupled quantum dots **55**
4.1 Photon-mediated coupling between two optical emitters . . . 55
4.2 Observation of super- and subradiant emission 58
4.3 Coherent evolution of the coupled system 62
4.4 Proof-of-principle controlled preparation of the collective state 68
4.5 Summary of the coupling parameters 72
4.6 Summary and Connection 72

5 Anti-dip in photon coincidences from coupled quantum dots **75**
5.1 Resonant fluorescence cross-correlation with coupled emitters 77
5.1.1 Calibration and alignment of optical setup 77
5.1.2 Resonance fluorescence spectra of coupled emitters . . 79
5.1.3 Photon coincidences from single-emitter driving 79
5.1.4 Interpretation of the photon coincidences 81
5.1.5 Numerical simulations for various experimental conditions 83
5.1.6 Driving the less noisy emitter 88
5.2 Photon coincidences in resonant transmission 89
5.2.1 Preliminary interpretation using numerical simulations 90
5.3 Summary 92

6 Conclusion and Outlook **93**
6.1 Summarizing and reflecting 93
6.2 Outlook 97
6.2.1 Improving the coupling strength 97
6.2.2 Scaling-up to multiple coupled quantum dots 98
6.2.3 Towards the generation of photonic cluster states from two coupled quantum dots 98
6.2.3.1 Generating dipole-dipole entanglement on demand 99
6.2.3.2 Independent spin-spin tuning 100

A Power tuning **103**

B Decay dynamics with excitation through higher-energy states **105**

C Decay dynamics with resonant excitation **109**

D Photon coincidences driving the less noisy emitter **111**

E Preliminary characterization of the spatial light modulator (SLM) **113**

Multi-emitter coupling for scalable quantum-information processing

Evolution of quantum mechanics in a nutshell

The development of quantum mechanics in the early decades of the 20^{th} century fundamentally transformed our understanding of the physical world. In 1900, Max Planck proposed the quantization of the energy exchanged between light and matter to explain thermal radiation [1]. He was followed shortly after by Albert Einstein who introduced the particle nature of light, later named "photon" [2], in his theory on the photoelectric effect [3, 4]. In 1913, Niels Bohr introduced his model of the atom with the quantized electronic orbits, expanded later by Louis de Broglie, who suggested that the orbiting electron has wave-like properties [5]. Building on de Broglie's approach, Heisenberg and Schrödinger formalisms were developed. The latter put forward a probabilistic view of the world, where a "wavefunction" describes the quantum state of a physical system in space and time. With these additions, the fundamental idea of the wave-particle reality was completed. This duality of the elementary constituents of nature underlies numerous scientific and technological breakthroughs in electronics and photonics. From electronic semiconductor physics, that led to the invention of the transistor, to the concept of photons used to build lasers and the atom-photon interaction for the development of atomic clocks, this First Quantum Revolution has evolved into many of the core technologies underpinning modern society.

By 1982, with the experiment [6][1] of Alain Aspect demonstrating the violation of Bell's inequalities [8], the fundamental quantum mechanical concepts of superposition and entanglement were well accepted. Quantum superposition states that a particle, like an electron or a photon, can be in two states simultaneously, while entanglement describes that two or more individual particles correlated with each other, can not be described independently. It was in the late half of the same century that scientists thought of harnessing these explored concepts for real-world applications. In the words of Jonathan P. Dowling and Gerard J. Milburn "The First Quantum Revolution gave us new rules that govern physical reality. The Second Quantum Revolution will take these rules and use them to develop new technologies" [9].

[1] The original experiment was later considered to have a potential flaw, the detection loophole. Numerous other experiments followed considered loophole free, confirming Aspect's original result [7].

From bit to qubit

Today, advancements in technology and engineering, have enabled us to apply quantum mechanics to initialize, manipulate, and measure individual quantum systems. These are physical systems that can be described by two quantized states. Aiming to leverage their properties of superposition and entanglement, in recent years researchers use such two-level systems to encode information[2]. Contrary to a classical bit of information, which can be either 0 or 1, a quantum bit or "qubit" can be in a coherent superposition of both 0 and 1 simultaneously (here $|0\rangle$ and $|1\rangle$ in Dirac's notation). A set of such information carriers hold promise for securing communications, enhancing the performance of measurements for quantum sensing and metrology and serving as elementary quantum processors for "quantum computations", solving long-standing problems exponentially faster than classical computers. An example of their most noble application is predicted to be in life science and chemistry, where complex quantum simulations of molecular systems could help in drug discovery.

Currently the development of quantum technologies for practical uses is challenged by the degree of controllability over these quantum systems, and the necessity of protecting them from a noisy environment and decoherences. Whether or not we are at a potential onset of a second quantum revolution, and if it will be as successful as anticipated, is yet to be decided. However, the first encouraging indications arrived with the development of quantum algorithms based on genuine quantum effects, that greatly speed up some classes of calculations. Two noteworthy examples are Grover's search algorithm [11] and Shor's algorithm for factoring [12], with the latter showing evidence of superpolynomial speedup compared to the best-known classical counterpart.

Solid-state quantum emitters as photonic qubit sources

Over the past years, a number of different platforms have been investigated and developed in parallel for their potential as qubits. Each comes with its own advantages and challenges. A few examples of the currently leading ones are trapped ions, superconducting circuits, neutral atoms, nitrogen vacancies in diamond, semiconductor spins and photons. Photons are attractive candidates for qubit encoding and manipulation [13]. They can encode information in various degrees of freedom, such as their number, frequency, spatial or temporal mode and polarization, while interacting very weakly with their environment. This inherent resilience against decoherence and noise makes photonic qubits promising for quantum communication applications, for secure transmission of secret messages, and for scalable, fault-tolerant quantum computations.

[2] In the words of Richard Feynman, launching quantum computing as a field of study "...nature isn't classical, dammit, and if you want to make a simulation of nature, you'd better make it quantum mechanical, and by golly it's a wonderful problem because it doesn't look so easy"[10].

However, the weak photon-photon interaction has also the drawback of prohibiting two-qubit interactions. This prevents them from fulfilling the 4^{th} condition of DiVincenzo's criteria for a universal quantum computer, requiring a universal set of quantum gates [14]. To overcome this limitation, theoretical proposals with linear optics, submitting photons to interferometric networks and using detection feedback [15] were implemented experimentally. For most, probabilistic sources of entangled photon pairs by spontaneous parametric down-conversion (SPDC) were employed. As this approach appears challenging to scale up due to its probabilistic nature in qubit generation, there was a need for a more efficient photon source. An alternative is to use quantum emitters as deterministic single photon sources and induce indirect interactions between photons via non-linear coupling to their emitter.

Solid-state quantum emitters can provide fast photon emission and be integrated into photonic nanostructures that allow enhancement of the light-matter interaction, making them particularly promising for scalable architectures [16]. The study of such photon sources is accompanied by advances in the development of integrated optical components, paving the way for a quantum computer with a hybrid platform of matter and photon qubits on chip.

Quantum dots for multi-emitter applications

Among other promising solid-state emitters stand quantum dots, artificial atoms grown inside a semiconductor host material, operating effectively as two-level systems. Embedded in photonic nanostructures, they can generate efficiently pure single photons on demand [17], while control over their charge solid-state environment leads to high indistinguishability between the photons emitted [18]. In addition, a quantum dot can posses a spin [19] which enables it to mediate the interaction between emitted photons, resulting in entanglement between the matter-spin qubit and the photons polarization degree of freedom. This allows for the generation of one-dimensional cluster states of entangled photons [20], which are valuable resource for measurement-based quantum computing.

However, for universal quantum computing, higher-dimensional entangled states are required [21]. For this purpose, protocols for fusing smaller entangled states together have been developed for fault-tolerant quantum computing [22, 23]. Nevertheless, using a single quantum emitter as the source, fusion is rather challenging as it is sensitive to photon losses, and the overall success probability decreases rapidly with the number of fusion operations [24].

To this end, a deterministic approach of scaling-up the number of emitters to generate up front highly entangled multi-photon states has been proposed, as particularly tolerant to qubit losses [25]. The theoretical proposal involves two coupled quantum dots generating a two-dimensional cluster

state of polarization-encoded photonic qubits [26]. Along these lines, protocols for spin-spin entanglement between distant emitters in subwavelength-confined structures [27] could be realized among spins of coupled quantum dots, with the interaction mediated by the mode of the nanostructure in which they are placed.

Multi-emitter coupling finds use too in quantum communication, as it can mitigate the challenge posed by photon losses. Photons appear to be naturally the information carriers for quantum communication, as they propagate with high speed and have long coherence times. Transmitted over long distances through the existing optical fiber network or free space with little decoherence, photonic qubits have been envisioned to bridge distant quantum nodes, where information would be generated, processed or stored locally, enabling a quantum internet [28]. The main limitations for its realization are owed to losses and decoherences, as photons propagate over long, usually lossy, channels. In quantum communication, due to the no-cloning theorem, quantum information can not be amplified as it is done classically. A solution to this is given by quantum repeaters, which divide the total distance between the sender and receiver into many short links. By creating entanglement between the two parties, quantum information can be teleported over long distances [29]. Quantum repeaters require either nodes with long-lived quantum memories [30], or sources of entangled photons. For the latter, a scheme for all-photonic quantum repeaters has been proposed, where the information is encoded and protected in multi-photon entangled states [31]. Explicit protocols where only two coupled quantum emitters are needed for its realization have been recently put forward [32, 33]. Yet another proposal considering the interaction between multiple emitters, suggests using the notion of "subradiance" for quantum memories or photon storage [34]. Subradiance is described as the absence of radiation resulting from destructive interference of the spontaneous collective emission from an ensemble of emitters. The authors suggest leveraging this collective effect in an array of atoms coupled to a nanophotonic structure and introduce "selective radiance" to improve the fidelity of photon storage.

Thesis objective - Collective super- and subradiant dynamics of quantum dots in photonic nanostructures

Collective effects can occur from photon-mediated interaction of indistinguishable quantum emitters, via a shared electromagnetic mode. This coupling results in the emission of identical wave packets that cannot be spatially distinguished. The coupled system is then naturally described by a set of collective states, referred to as Dicke states [35]. In dense atomic ensembles [36–40] or solid-state emitters [41–44], Dicke states can yield super- (enhanced) and subradiant (suppressed) emission with modified temporal, spectral and directional properties.

Even though these collective phenomena have already been observed in free space with atoms and ions [37, 45] or with few superconducting

or solid-state emitters coupled to one-dimensional waveguides [42, 44, 46], quantum dots have been challenging candidates for the realization of controlled, coherent optical interactions. The drawbacks inherent to their self-assembled growth (randomness in size, the strain and composition) result in large variation of their resonant frequencies, limiting the chances of finding indistinguishable emitters. In addition, inhomogeneous broadening and decoherence introduced by the solid-state environment [47] can prohibit the observation of long-lived subradiant emission [48], emphasizing the need for a highly coherent light-matter interface. Finally, for coherent interaction between the quantum dots, the coupling strength needs to be larger than the decoherence rate, implying that the inter-emitter separations should then be at nanometric distances.

In this thesis, we demonstrate direct observation of super- and subradiant emission from three pairs of quantum dots, interacting via the shared mode of a photonic crystal waveguide. The waveguide essentially mitigates the requirement for spatial proximity of the emitters, as it extends the range of interaction[3] [47]. To bring the post-selected detuned quantum dots on resonance, we employ an external magnetic field as the tuning mechanism. The observation of the super- and subradiant emission is realized by lifetime measurements. The coherent dynamics are further investigated by recording the modification of the lifetime for a continuous range of detunings between the emitters, and controlled preparation of the initial collective state is studied while driving both quantum dots. Following previous works on quantum dots, where collective emission was demonstrated by recording the modification of the second-order intensity correlations [51–54], we probe the coupled system with continuous driving of a single emitter and record the photon coincidences. In [54], the authors rightly highlight that, despite the observed modification in the coincidence measurements at zero time delay —previously interpreted as the result of superradiant emission from the coupled system— the measured lifetimes did not exhibit super- and subradiance. Hence, they argue that photon coincidences are an ambiguous proof of collective phenomena [55]. Our results show that photon coincidences can be exclusively associated with superradiance when only a single emitter is directly driven.

More precisely, the thesis is structured as follows:

- Chapter 1 introduces the concepts of super- and subradiance. We begin by explaining the emergence of these collective emission phenomena in a dense atomic ensemble in free space, and then focus on the theoretical model describing the coupling of two emitters in a waveguide.

- Chapter 2 contains a description of the platform, the experimental setup, the basic excitation techniques and the optical systems used to perform the measurements.

[3] This could allow entanglement between distant emitters [49] or the construction of deterministic two-emitter quantum phase-gates [50]

- Chapter 3 describes the spectroscopic methodology used to identify the quantum dot candidates. Basic characterization of their properties, presentation of the control knob for their relative detunings, and imaging of the quantum dots inside the photonic crystal waveguide, are included.
- Chapter 4 demonstrates experimentally the photon-mediated coupling between pairs of quantum dots, by probing the coherent dynamics with lifetime measurements. Interpretation of the mechanisms that modify the collective emission when driving one emitter is discussed, and a proof-of-principle of controlled preparation to a collective state is discussed.
- In Chapter 5 we study the coupled system with second-order correlation measurements and explain why the existence of photon coincidences at zero delay time in resonance fluorescence, serves as evidence of superradiance when a single emitter is driven.
- Finally, Chapter 6 concludes the present work and outlines future research directions.

It is important to note that the present work constitutes fundamental research. Our goal is to demonstrate the feasibility of photon-mediated coupling between two dipoles separated by multiple wavelengths, using quantum dots embedded in nanophotonic waveguides. However, transitioning from this first demonstration to envisioned applications requires substantial future work, and the currently inherent scalability limitations of the platform must be addressed.

1 Theory of collective dynamics

In this chapter, we provide a brief introduction to the concepts of super- and subradiance, starting from their discovery by R.H. Dicke in 1954 and extending to their potential applications. A qualitative treatment on these phenomena follows, initially for an ensemble of N two-level emitters in free space and close proximity. We then narrow our focus to the simplest collective system of two emitters, where the effects are fundamentally the same, but easier to understand. Next, the two regimes of coupling induced by the emitter-emitter interaction are described. To justify their origin we start with the light-matter interaction for a system of N dipoles in an external field, and shortly explain the model. The effects of each coupling regime are summarized in an illustration of the energy diagram for the two-emitter case. Finally, we conclude with the system that was used for the experiments of this thesis; two emitters in a photonic crystal waveguide. Here, the theory employed for simulating and interpreting our experimental data in Chapters 4 and 5 is being discussed. The theory model was developed by Björn Schrinski, Oliver August Dall'Alba Sandberg and Anders Søndberg Sørensen for [56]. A detailed derivation is included in the Supplementary Material of the same work and in [57].

1.1 Introduction to super- and subradiance

We begin with the simple picture of a single emitter as a two-level system in free space. The two levels are the ground $|g\rangle$ and excited $|e\rangle$ states of the emitter, with a difference in energy of $\hbar\omega_0$. An emitter prepared in the excited state will spontaneously decay to the ground state with a characteristic rate Γ, induced by the vacuum fluctuations. This decay is accompanied by the simultaneous release of a photon, exhibiting an exponential decay pulse shape. For an ensemble of N such emitters, the simplified picture assumed that the intensity of spontaneous radiation from the ensemble would be N times that of the single emitter, with a rate Γ. The model was therefore suggesting that each emitter in the ensemble decays independently from the others.

That was up until the pioneering article of R.H. Dicke in 1954, where he stated that this assumption overlooks a key fact in the process, that the emitters interact with the same radiation field. Specifically, the work examines an ensemble of atoms, starting with all in the excited state. The size of the studied ensemble is smaller than the radiation wavelength $\lambda_0 = 2\pi/\omega_0$ (with c = 1, for the speed of light), and therefore all emitters see the same coherent field. In this system, the spontaneous radiation does not follow a single exponential behavior. Instead, it manifests as a brief, bright burst that initially rises in intensity, followed by a fast decay compared to the single

emitter. That is the phenomenon of collective spontaneous emission, that Dicke called *superradiance* [35].

To explain the mechanism of how superradiance occurs, we start with the discussed system of N atoms all in the excited state and in close proximity. When the first photon is emitted, the ensemble will be in an equal superposition of states[1], where every atom has been the one that decayed, $|\psi\rangle = |gee...e\rangle + |ege...e\rangle + ... + |eee...g\rangle = \{|gee...e\rangle\}$. This photon then induces correlations between the individual emitters, causing the next photon to be emitted faster, bringing in more correlations in the system. The correlations continue to build-up, leading to an avalanche effect, that increases till the number of emitters in the ground state exceeds that of the excited state.

Looking at the emitters as dipoles, these dipole-dipole correlations are induced as each one influences the radiative environment of its neighbors. Namely, the emitters of the fully inverted ensemble, initially in an incoherent state, synchronize[2] as they emit coherently in a common radiation field, locking in phase with each other [36]. This leads to an effective macroscopic dipole, that would emit a short pulse of high intensity. In other words, the emitted in-phase fields interfere constructively, giving a superradiant burst of light. The maximum intensity of the light emitted, is proportional to the square of the number N of atoms in the cloud, increasing their decay rate to $\Gamma_+ = N\Gamma$, due to energy conservation. This means that the coherently interacting emitters radiate their energy N times faster than with incoherent emission.

For superradiance to be observed in the first place, two fundamental conditions need to be fulfilled. One of them is that the emitters should be indistinguishable from each other, such that the transitions of the dipoles are degenerate in energy, and the other that there is permutational symmetry in the exchange between any two emitters in the system. Of course, even with these requirements satisfied, superradiance could still be constrained. A fundamental limitation to superradiance is the dipole-dipole Van der Waals coupling between the emitters ($\sim 1/r_{mn}^3$, where r_{mn} the inter-emitter distance). For a big ensemble, this coupling is non-invariant by emitter permutation. The system can then evolve to states other than the maximum-correlated-symmetrical ones, deviating from the perfectly symmetrical superradiant behavior. Another factor that would restrict superradiance is dephasing. The cooperative effect of superradiance, arising from the correlated dissipation of the emitters, constitutes a macroscopic observable of the quantum coherence of the system. Coherence here, refers to both the electromagnetic field and the emitters themselves. The presence of any cause of dephasing; i.e., any inhomogeneity or noise from the environment, would restrict or prohibit this phase-locking condition between the dipoles, consequently decreasing or eliminating superradiance [58]. Furthermore, the

[1] One hole is equally spread over every single atom.

[2] This synchronization happens with the first emitted photon. If it does not happen then, it never will.

enhancement of emission can be also constrained by the presence of multiple channels, or modes, that the system can decay into. Specifically, as the spatial separation between the emitters increases, more channels become relevant for the decay, and the atomic phases get randomized after several emissions. Therefore superradiance gets diminished, as photons emitted in different channels do not enhance one-another [59].

In free space, the amount of superradiant emission and its directionality depends on the geometry of the sample [59]. That is due to constructive collective interference of the emitted fields in those directions, leading to enhanced emission in specific decay channels or modes of the electromagnetic field. However, constructive interference from the emission of an ensemble does not necessarily hint superradiance, and if one wants to be careful, would need to distinguish between the different cases. Signatures similar to the ones from superradiance have been observed in photon coincidences, for inter-emitter distances larger than the radiation wavelength [54]. Even though this too is a result of cooperative emission, it has been distinguished from superradiance as measurement-induced cooperativity [55]. In another limit, for closely spaced emitters experiencing homogeneous broadening, superradiance turns into amplified spontaneous emission (ASE), a phenomenon described as a sequence of spontaneous and stimulated emission by the individual emitters [58, 60]. Against this scenario, superradiance occurs so quickly, that makes it impossible, in principle, to treat the process as a sequence of individual events. In free space, for dimensions within a defined cooperative length, the whole collective system radiates as a single entity, leading to an overall increase of the radiative decay rate.

Up to now, within Dicke's model in free space, we have only mentioned the permutationally-symmetric states, where the in-phase emission from the dipoles leads to constructive interference. That is a single channel, and the only possible path, through which the collective excitation decays to its ground state, resulting in superradiant emission. However, there also exist anti-symmetric manifolds of collective states, where the fields emitted by the dipoles interfere destructively. Hence, photon emission from these states is highly suppressed ($\Gamma_- = 0$), giving rise to superradiance's complementary phenomenon, *subradiance*. Within the discussed model, ideal subradiant states are not possible to populate, as they are decoupled from an external drive, preventing from any observation of subradiance.

In an experimental implementation, the real conditions differ from the symmetry of the Dicke model. This occurs either due to the finite size of the ensemble of emitters, unlike the proposed point-like distribution, or the disordered positioning of the emitters, leading to variations in the interactions between the dipoles. This symmetry breaking can enable the population of the subradiant states, indirectly, through the decay of a superradiant state to a subradiant one, and directly by driving with a longer excitation pulse [40], or choosing the right angle for the driving laser [61]. Their observation has been realized in recent experiments with cold atomic ensembles, where subradiance is recorded as a slow emission, compared to the decay of the single emitter [39, 62–64].

Collective effects have also been studied in waveguide quantum electrodynamics (QED) with different emitters, where only two modes are present, the left- and right-propagating waveguide modes, with respect to the emitter's position[3]. The observation of collective effects in waveguide QED is made possible via photon-mediated interaction or *coupling* [42, 46, 65] and interference effects in an ensemble of emitters [66]. In the former case, the collective effects are leveraged by the platform, as the waveguide-mediated coupling extends the spatial range of the interaction among strongly coupled emitters to the guided mode, while suppressing other decay channels. Having the ability to increase the inter-emitter distance, ensures the probing of the "pure" Dicke superradiance effect, as the dipole-dipole dephasing due to Van der Waals coupling, becomes negligible [36]. The spatial range of the interaction is upper bounded by the losses from the propagation in the waveguide, or by retardation in case of a large ensemble ($> c/\Gamma$).

Superradiant states can be populated by driving the emitters through the waveguide. However, that is not a possibility for the subradiant states, in the absence of imperfections. Destructive interference decouples them from the electromagnetic environment of the waveguide, making them unable to drive and to decay in it. From a different perspective, the fact that the subradiant states cannot decay in the waveguide, means that they emit outside of it, through the leaky mode. This imperfection of the structure can therefore be exploited to address these otherwise inaccessible dark states, by driving the system from the top of the waveguide. In fact, with this driving scheme [46], one can control the relative driving phase between the emitters, leading the system to exhibit super- or subradiant decay.

While super- and subradiance were first introduced in the same work, the former has been comparably studied more extensively, both theoretically [36, 55, 58, 59, 67] and experimentally [37, 45, 52, 66, 68]. Over the years, superradiance has been studied as a means of enhancing the efficiency of coherent light sources [69, 70], improving precision in quantum metrology [71, 72] and as a building block for quantum information processing [73, 74][4]. On the other hand, subradiance initially received less attention, possibly due to the challenges in efficiently addressing the subradiant states. The recognition of subradiance as an exciting and valuable phenomenon came with the realization that the inability to emit photons makes subradiant states long-lived coherent states. In recent years, the study of subradiance has seen increasing interest, both from a theoretical [48, 61, 74, 75], as well as an experimental perspective [40, 42, 44, 46, 76, 77]. In addition to proof-of-principle demonstrations of subradiance, its potential as a resource for implementing quantum information protocols, and more specifically, for storing light with optimized fidelity, is being explored [34, 39].

[3] In reality, there exists also a leaky mode outside the waveguide, due to structural imperfections.

[4] Fun fact from a discussion with Anders Søndberg Sørensen: "It is superradiance that makes the windows transparent".

1.2 The Dicke model

Following the work of M. Gross and S. Haroche [36], we begin with the general case of a dense atomic ensemble in free space, and show how superradiance rises from its spontaneous emission. We then narrow the discussion down to the case of two emitters to approach the system that was experimentally investigated during this thesis.

1.2.1 Superradiance in a dense atomic ensemble

We begin with an atomic cloud in free space, consisting of N atoms in close proximity (size < λ_0). Each atom is a 2-level system with a ground $|g\rangle$ and an excited $|e\rangle$ state, separated by a transition energy of $\hbar\omega_0$. The exploration of the ensemble starts at time $t = 0$ with all the atoms in their excited state, $|\psi(0)\rangle = |eee....e\rangle$.

To look into how the system decays, we introduce the atomic raising $\hat{\sigma}_m^+ = |e\rangle_m \langle g|_m$ and lowering operators $\hat{\sigma}_m^- = |g\rangle_m \langle e|_m$ for the m^{th} atom. For that, the atomic lowering operator is applied on each emitter. Borrowing the notation often used for spin-$1/2$ systems, for an ensemble of N atoms this should result in a number of eigenstates with total angular momentum $J = N/2$, of the form

$$|J, M_J\rangle = \sqrt{\frac{(J+M_J)!}{N!(J-M_J)!}} \left(\sum_m \hat{\sigma}_m^-\right)^{(J-M_J)} |eee...e\rangle\,, \tag{1.1}$$

where M_J is the projection of the total angular momentum $-J \leq M_J \leq J$, $\sum_m \hat{\sigma}_m^-$ is the collective de-excitation operator for $m = 1, 2, 3, ..., N$ atoms, and $J - M_J$ is the number of emitters in $|g\rangle$ state for each $|J, M_J\rangle$, given by $\langle \sum_m \hat{\sigma}_m^- \hat{\sigma}_m^+ \rangle = \langle J, M_J | \sum_m \hat{\sigma}_m^- \hat{\sigma}_m^+ |J, M_J\rangle = J - M_J$.

The resulting states would be of the form,

$$|J, M_J\rangle = S\{|ggg...eee\rangle\}, \tag{1.2}$$

where each $|J, M_J\rangle$ is a symmetrical superposition of eigenstates, with respect to permutation between atoms of the ensemble and S is a symmetrization operator. Each state consists of $J - M_J$ atoms in the $|g\rangle$ state and $J + M_J$ in the $|e\rangle$. With the above operation the system results in $2J + 1$ such symmetrical eigenstates, separated by equal energy of $\hbar\omega_0$. This is known as the *Dicke ladder* and is depicted in Figure 1.1. In this picture, the system decays with a cascaded emission of photons along the ladder, and the energy emitted will be $M_J\hbar\omega_0$, depending on the initial $|J, M_J\rangle$ state.

To explain how this collective behavior affects the spontaneous emission of the ensemble, we use a qualitative description of the rate of photon emission, W. Generalizing the radiation rate of a single emitter W_1, a large effective dipole composed of N atoms gives

$$W_1 = \Gamma \left\langle \hat{\sigma}_1^+ \hat{\sigma}_1^- \right\rangle \rightarrow W_N = \Gamma \left\langle \hat{J}^+ \hat{J}^- \right\rangle, \tag{1.3}$$

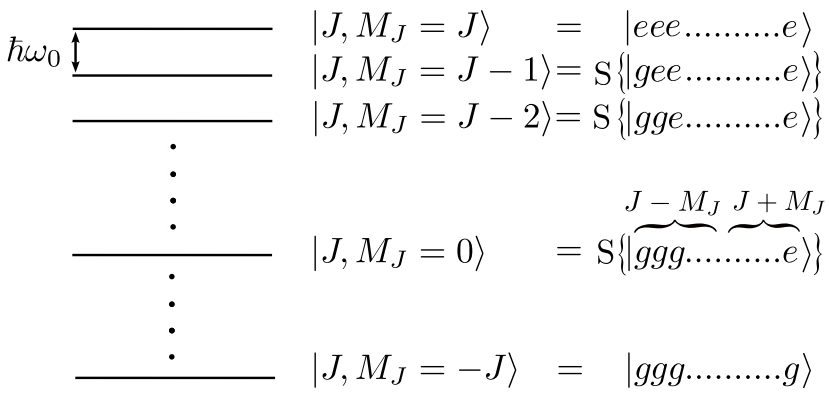

FIGURE 1.1: The Dicke ladder: Energy diagram of an atomic dense ensemble of N atoms that behave collectively. The collective states are equidistant, separated by $\hbar\omega_0$. For each $|J, M_J\rangle$ the number of atoms in $|e\rangle$ ($|g\rangle$) state is given by $J + M_J$ ($J - M_J$). Cascading down the ladder will induce superradiant emission. The Figure is directly adapted from [36].

where Γ is the decay rate of a single atom. With $\hat{J}$ representing the collective operator of the total angular momentum, $\left\langle \hat{J}^+\hat{J}^- \right\rangle = \langle J, M_J| \hat{J}^+\hat{J}^- |J, M_J\rangle$ gives the average number of excited atoms, with $\hat{J}^\pm = \sum_m \hat{\sigma}_m^\pm$. We use the $\hat{J}^2 = 1/2\left(\hat{J}^+\hat{J}^- + \hat{J}^-\hat{J}^+\right) + \hat{J}_z^2$ operator, where $\hat{J}_z = 1/2\sum_m \hat{\sigma}_m^z$, and the commutation relation between $\hat{\sigma}_m^+$ and $\hat{\sigma}_m^-$,

$$\begin{aligned} \hat{J}^2 |J, M_J\rangle &= J(J+1) |J, M_J\rangle \\ \hat{J}_z |J, M_J\rangle &= M_J |J, M_J\rangle \\ \left[\hat{\sigma}_m^+, \hat{\sigma}_n^-\right] &= 2\delta_{mn}\hat{\sigma}_m^z, \end{aligned} \tag{1.4}$$

to deduce the average number of atoms in the excited state $\left\langle \hat{J}^+\hat{J}^- \right\rangle$ as,

$$\begin{aligned} \langle J, M_J| \hat{J}^+\hat{J}^- |J, M_J\rangle &= \langle J, M_J| \hat{J}^2 - \hat{J}_z^2 + \hat{J}_z |J, M_J\rangle \\ &= J(J+1) + M_J(-M_J+1), \end{aligned} \tag{1.5}$$

Rewriting (1.5) we finally get from (1.3),

$$W_N = \Gamma(J + M_J)(J - M_J + 1), \tag{1.6}$$

From (1.6) it becomes clear that the radiation rate increases as the population cascades down the Dicke ladder. From $2\Gamma J = N\Gamma$ of the fully inverted population, $|J, M_J = J\rangle$, it reaches the maximal rate of $J(J+1)\Gamma = \frac{1}{2}N(\frac{1}{2}N+1)$ when half of the population is in the excited state, $|J, M_J = 0\rangle$[5]. From here we already see that the photon emission rate increases significantly as the system cascades down the ladder, and the system loses energy with a maximum rate proportional to N^2 for the half-excited state. From

[5]As there are no interference terms, there is no superposition state that can radiate stronger than $|J = N/2, M_J = 0\rangle$.

that state down, the decay rate decreases till it reaches $|J, M_J = -J\rangle$, where all the atoms are in the ground state and the emission stops.

The initial increase of the decay rate up to the $|J, M_J = 0\rangle$ state is a consequence of the strong correlations that build up between the interchangeable atoms. This build-up begins with the first emitted photon in the ensemble, as the which-atom-emitted information is lost. The induced correlations from this decay cause the locking of the emission phase of the atoms in the cloud, giving rise to the effective collective dipole. As they now emit collectively, the radiated intensity is proportional to N^2, and thus the emission of N photons occurs in a time N times shorter compared to the spontaneous emission rate of the single emitter, due to energy conservation. The system therefore exhibits the signatures of superradiance.

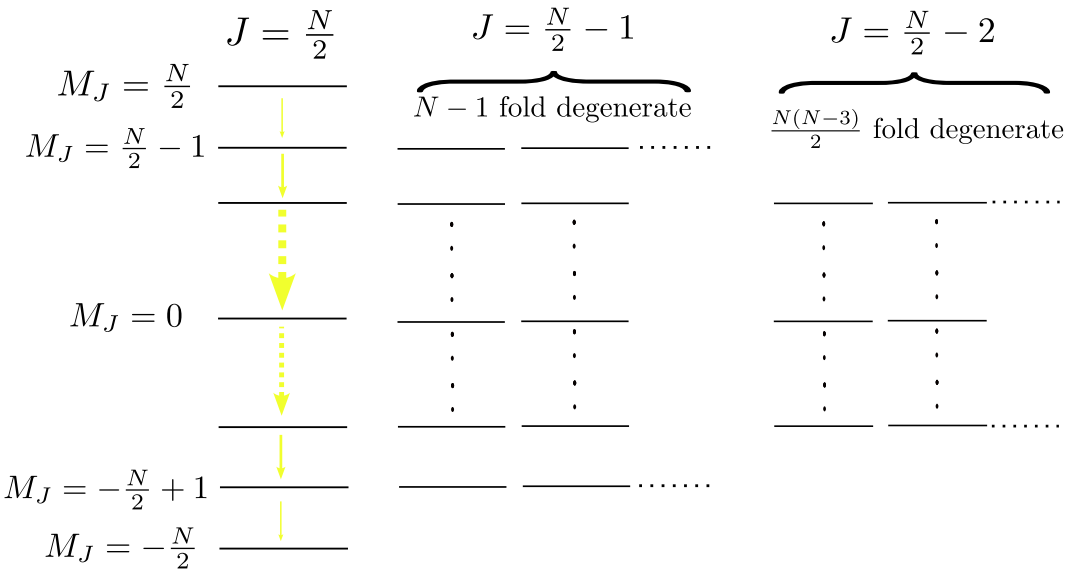

FIGURE 1.2: Energy diagram of collective Dicke states for N atoms, where the subradiant manifolds ($J \neq N/2$) are present next to the superradiant Dicke ladder ($J = N/2$) illustrated in Figure 1.1. The thickness of the arrows in the latter shows the change of the spontaneous radiation probabilities as the collective system decays. The Figure is adapted from [35].

Before proceeding in the discussion, it is essential to highlight here that the permutationally symmetric states included in the ladder of Figure 1.1 are only the ones involved in the superradiant emission. However, those are not the only states of the collective system. For each M_J there is a number of states for all possible J values within $|M_J| \leq J \leq \frac{N}{2}$, that are degenerate in energy[6]. This leads to multiple ladders of states, extended next to the superradiant one [35], as illustrated in Figure 1.2, that are anti-symmetric and therefore not invariant to atom exchange, as the superradiant states. These states are not coupled to the environment or to the external drive, making them challenging to populate and unable to decay. They exist only for ensembles with an even number of emitters and exhibit as well high correlations. Though, in contrast to the superradiant case, the emitters radiate

[6]The total angular momentum in principle takes all the values $J = 0, 1, ...N/2$. We started the discussion with the $J = N/2$ to focus on the ladder giving the superradiance.

in pairs out-of-phase with each other, resulting into very low (or zero in the ideal case) radiation rates. Hence, these states are rightfully named *subradiant*. In order to access such long-lived states, there should be a symmetry breaking of the ensemble, which could for example be made possible by increasing its size. Another approach to populating subradiant states, is to make use of pulses with duration longer than $N\Gamma$. This has been shown to increase the likelihood of populating subradiant states rather than the superradiant [78], a mechanism that could be attributed to the quantum Zeno effect [79].

1.2.2 Two-atom collective emission

Superradiance can be observed even in the smallest system that could show any collective behavior. That is the one with only two atoms (N = 2) sitting much closer than λ_0. In this case, it is simple to include in the energy diagram all the stationary states of the collective system, since $0 \leq J \leq 1 \Rightarrow J = 0, 1$. The resulting $|J, M_J\rangle$ states then are: $|0,0\rangle$, $|1,1\rangle$, $|1,0\rangle$ and $|1,-1\rangle$. For $|1,1\rangle$ and $|1,-1\rangle$, both atoms are in the excited or the ground state, respectively. We further on adopt the notation $|1,1\rangle \rightarrow |ee\rangle$ and $|0,0\rangle \rightarrow |gg\rangle$ for clarity. For the states $|0,0\rangle$ and $|1,0\rangle$ one emitter is in the excited while the other in the ground state. Specifically, the two are defined as the symmetric $|1,0\rangle \rightarrow |+\rangle = \frac{1}{\sqrt{2}}(|eg\rangle + |ge\rangle)$ state, alike the symmetric triplet state in the spin-$1/2$ systems, and the anti-symmetric $|0,0\rangle \rightarrow |-\rangle = \frac{1}{\sqrt{2}}(|eg\rangle - |ge\rangle)$ state, known as singlet. They are degenerate in energy and compose the single-excitation subspace. The energy diagram describing the two-emitter system is shown in Figure 1.3. In comparison to the N-atom case, we can already correspond the three-level ladder of J_+ to the superradiant decay path, and J_- to the subradiant one.

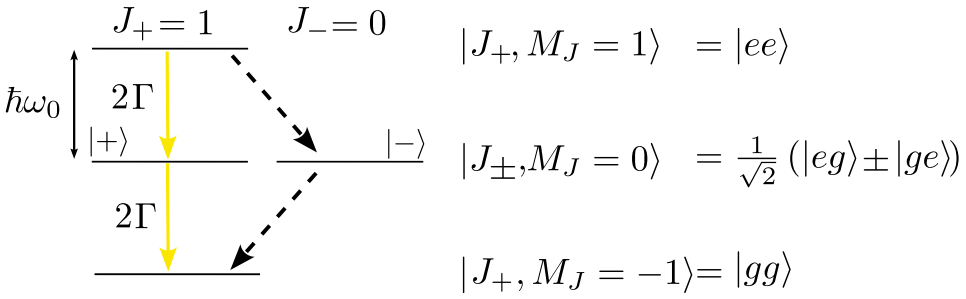

FIGURE 1.3: Energy diagram of the collective states for a two-atom system. The two intermediate states $|+\rangle$ and $|-\rangle$ are degenerate in energy and correspond to in- or out-of-phase emission from the two emitters. That, would lead to super- or sub-radiant emission from the two-atom system, respectively. In the superradiant case (yellow arrows), the decay rate will be twice the one of the single emitter, Γ. The cascade down through the subradiant state, $|-\rangle$ (dashed arrows), is prohibited as it is decoupled to the environment.

Similar to the qualitative derivation for the N-atom system, we focus on

the $J_+ = 1$ ladder. Looking into the photon emission rate W_2, we aim to show that the two indistinguishable emitters exhibit superradiance. Starting in the doubly excited state $|ee\rangle$ at $t = 0$, the initial population probabilities for the three $J_+ = 1$ states are $P_{|ee\rangle}(0) = 1$, $P_{|+\rangle}(0) = P_{|gg\rangle}(0) = 0$. At a later time t, the system starts to decay. The states that contribute to the emission are $|ee\rangle$ and $|+\rangle$ with a rate calculated by (1.6) to be 2Γ, while $|gg\rangle$ does not emit. The photon emission rate of the two-emitter system is then given by,

$$W_2(t) = 2\Gamma \left(P_{|ee\rangle}(t) + P_{|+\rangle}(t) \right). \tag{1.7}$$

The average number of excited atoms can also be written in terms of the probabilities as,

$$\left\langle \sum_{m=1,2} \hat{\sigma}_m^+ \hat{\sigma}_m^- \right\rangle = 2P_{|ee\rangle}(t) + P_{|+\rangle}(t). \tag{1.8}$$

Using then the intuitive argument, that the decrease in the number of the excited atoms should be equal to the photon emission rate at any time, we write,

$$-\frac{d\left\langle \sum_{m=1,2} \hat{\sigma}_m^+ \hat{\sigma}_m^- \right\rangle}{dt} = W_2(t). \tag{1.9}$$

which by (1.7) and (1.8) turns into,

$$2\frac{dP_{|ee\rangle}(t)}{dt} + \frac{dP_{|+\rangle}(t)}{dt} = -2\Gamma \left(P_{|ee\rangle}(t) + P_{|+\rangle}(t) \right). \tag{1.10}$$

To solve (1.10) and find the time dependent probabilities, we start with the doubly excited state $|ee\rangle$. While in this state, the two emitters are not correlated to each other. The first photon can therefore be emitted by either of the two with a rate Γ, as the emitters act independently. The total probability for this state to decay is then 2Γ. Hence,

$$\frac{dP_{|ee\rangle}(t)}{dt} = -2\Gamma P_{|ee\rangle}(t). \tag{1.11}$$

Plugging (1.11) in (1.10),

$$\begin{aligned} P_{|+\rangle}(t) &= 2\Gamma\, t\, e^{-2\Gamma t} \\ P_{|ee\rangle}(t) &= e^{-2\Gamma t}, \end{aligned} \tag{1.12}$$

and from the total probability conservation: $P_{|ee\rangle}(t) + P_{|+\rangle}(t) + P_{|gg\rangle}(t) = 1$ we find

$$P_{|gg\rangle}(t) = 1 - (1 + 2\Gamma t)\, e^{-2\Gamma t}. \tag{1.13}$$

The photon emission rate of the collective system is then derived as,

$$W_2(t) = 2\Gamma\,(1 + 2\Gamma t)\,e^{-2\Gamma t}. \tag{1.14}$$

To emphasize the effect of the collective behavior, we compare (1.14) to the photon rate resulting from the independent emission of two simultaneously excited atoms, $W_{2\,ind}(t) = 2\Gamma e^{-\Gamma t}$. To visualize the difference, the two cases for independent (Figure 1.4(a)) and coupled (Figure 1.4(b)) emitters are plotted together in Figure 1.4(c). Starting from the doubly excited state $|ee\rangle$, both rates begin from the same value at $t = 0$, since the two emitters are not yet correlated. At short times after the decay, the photon rate of the collective system, W_2, exceeds that of the independent emitters, $W_{2\,ind}$, exhibiting non-exponential behavior, characteristic of the superradiant emission from the decay of $|ee\rangle$. At longer times W_2 becomes smaller than $W_{2\,ind}$, due to energy conservation. This small overshooting of W_2 at short times is the manifestation of superradiance, that results in the decay being twice as fast when the emitters are correlated.

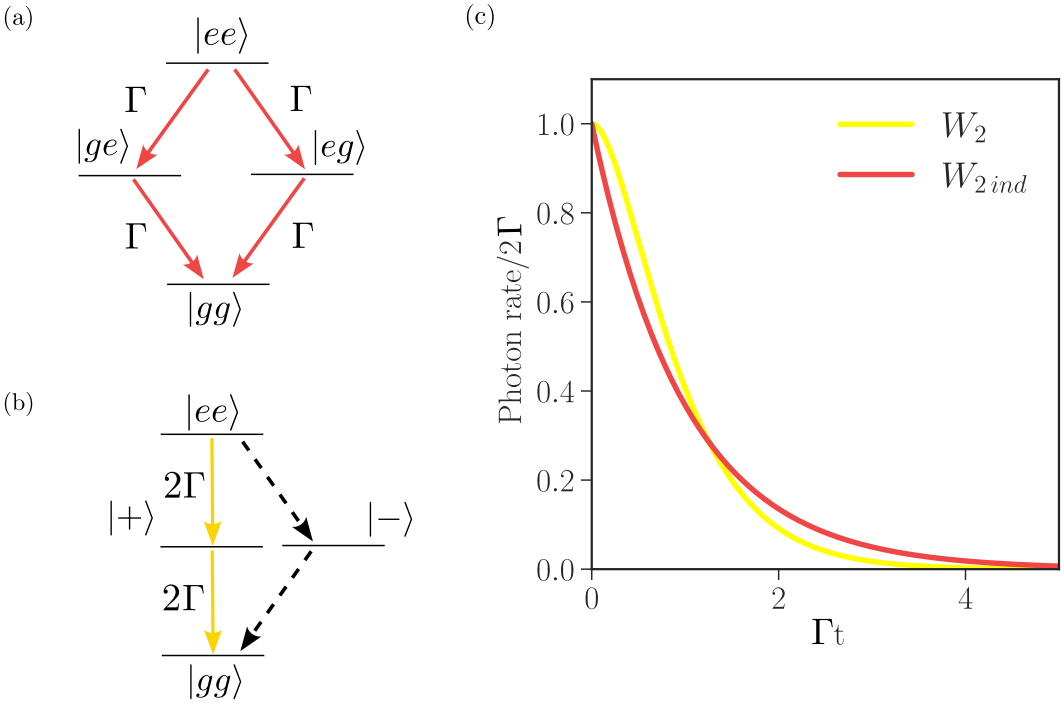

FIGURE 1.4: Energy diagrams of two (a) distinguishable and (b) superradiant emitters. (c) Photon decay rates from a two-atom system, when the emitters decay collectively (yellow), and independent from each other (red). Here an initially prepared doubly excited state, $|ee\rangle$, is assumed. Figure is adapted by [55].

In the three-level ladder the two decays appear to have identical rates of 2Γ. It is important to highlight here that each one is attributed to a different reason. From the doubly excited $|ee\rangle$ to the symmetric superradiant state, $|+\rangle$, the decay has twice the rate of the single emitter, because at that point the two uncorrelated atoms decay independently, each with a rate Γ. Schematically this can be explained using Figure 1.4(a) which indicates that

the 2Γ decay rate results due to the presence of two decay channels from $|ee\rangle$, the $|eg\rangle$ and $|ge\rangle$, with rates Γ each. This is consistent too with the photon rate deducted by (1.6) for $J = M_J = 1$. The actual superradiant effect manifests at the second decay from $|+\rangle$ to the collective ground state, $|gg\rangle$. There, the two emitters have interacted via the first emitted photon, which generated correlations between them. That induces the enhanced dipole, which decays with twice the rate of the single emitter, through the single available decay channel. This enhanced decay rate is a clear indication of cooperation of both atoms in the emission process, and reveals coupling between the two.

What is even more fundamental to highlight here is that this modification of the decay rate is present even if there is only a single excitation in the system. This is when the so-called single-photon superradiance takes place. Characteristically, Dicke uses the example of two neutrons, at distance closer than the radiation wavelength λ_0, where only one of them is in the excited state [35]. In this scenario, the initial state of the system is $|eg\rangle$. Written in terms of the super- and subradiant states $|eg\rangle = \frac{1}{\sqrt{2}}(|+\rangle + |-\rangle)$, the system would have a probability of one-half to emit a photon. If the neutrons were in the subradiant (singlet) state, then no photon would be emitted, as the singlet state is not coupled to $|gg\rangle$. Instead, if the neutrons were in the superradiant (triplet) state, the emission of a photon would occur with certainty and a rate twice that of the single emitter. We then see that the correlations between the emitters are generated simply by the fact that they sit within the same electromagnetic field, where, in the illuminating words of R. H. Dicke, simply "the presence of the unexcited neutron in this case doubles the radiation rate".

Closing this section, one could be equally confused and fascinated by the fact that superradiance in this single-excitation subspace is still a result of constructive interference, and what interferes here is "the emission from one **or** the other emitter".

1.3 Dissipative and dispersive coupling regimes

Up to now we discussed about the collective emission from an ensemble of atoms and derived the modification of the decay rate for two in free space. Before delving into the investigation of the system used in the experiments of this thesis —a pair of quantum emitters coupled through a shared waveguide mode— we first need to introduce the coupling regimes that define the type of interaction between the emitters. Namely, the *dissipative* and *dispersive* coupling regimes.

To provide some intuition on that, we begin with the description of the light-matter interaction. The Hamiltonian that describes a system of N two-level identical emitters coupled to an electromagnetic field is given by,

$$H_{tot} = H_D + H_F + H_I, \tag{1.15}$$

where H_D is the Hamiltonian describing the N dipoles,

$$H_D = \sum_m \hbar\omega_0 \, \hat{\sigma}_{ee}^m \,, \tag{1.16}$$

with $\hat{\sigma}_{ee} = |e\rangle \langle e|$ and $\hbar\omega_0$ the energy difference between $|g\rangle$ and $|e\rangle$ for each one of the identical emitters. The H_F is the Hamiltonian of the electromagnetic field in the notation of the bosonic creation and annihilation operators, $\hat{\alpha}_k^\dagger$, $\hat{\alpha}_k$, respectively

$$H_F = \int \hbar\omega_k \hat{\alpha}_k^\dagger \hat{\alpha}_k \, dk, \tag{1.17}$$

where k is the wavenumber and $\hbar\omega_k$ the energy of the photon for each mode. Lastly, the Hamiltonian describing the interaction of the light with the electric dipoles reads,

$$H_I = -\sum_m \left[\hat{\mathbf{E}}^+(\mathbf{r}_m) + \hat{\mathbf{E}}^-(\mathbf{r}_m) \right] \hat{\mathbf{p}}_m, \tag{1.18}$$

with $\hat{\mathbf{p}}_m$ the dipole moment operator of the m^{th} emitter. For the expression of the electromagnetic field $\hat{\mathbf{E}}^+(\mathbf{r}_m)$ we resort to the quantization technique based on the classical electromagnetic Green's function, $\mathbf{G}(\mathbf{r}, \mathbf{r}_n, \omega)$, [50, 80, 81] to avoid the heavy derivation using creation and annihilation operators [57].

We consider a system of N polarizable dipoles $\mathbf{p}_n$ at positions $\mathbf{r}_n$, and a known input driving field $\mathbf{E}_p(\mathbf{r}, \omega)$. The dipoles are excited by the field and re-scatter light in the ensemble themselves. The total field at a position $\mathbf{r}$ is then described by $\mathbf{E}(\mathbf{r}, \omega) = \mathbf{E}_p(\mathbf{r}, \omega) + \mu_0\omega^2 \sum_{n=1}^N \mathbf{G}(\mathbf{r}, \mathbf{r}_n, \omega) \cdot \mathbf{p}_n(\omega)$, where μ_0 is the vacuum permeability. Here, $\mathbf{G}(\mathbf{r}, \mathbf{r}_n, \omega)$ is the total Green's function, describing the electromagnetic field that a dipole in position $\mathbf{r}$ experiences, due to another dipole n oscillating in $\mathbf{r}_n$.

Direct correspondence to the quantum counterpart applies by replacing the field and the dipole moment with their operators. Assuming narrow bandwidth emission around the resonance frequency ω_0 of the dipoles, we can approximate $\mathbf{G}(\mathbf{r}, \mathbf{r}_n, \omega) \rightarrow \mathbf{G}(\mathbf{r}, \mathbf{r}_n, \omega_0)$. The generalized input-output equation for the total field then reads [34],

$$\hat{\mathbf{E}}^+(\mathbf{r}) = \hat{\mathbf{E}}_p^+(\mathbf{r}) + \mu_0\omega_0^2 \sum_{n=1}^N \mathbf{G}(\mathbf{r}, \mathbf{r}_n, \omega_0) \cdot \mathbf{d} \, \hat{\sigma}_n^- , \tag{1.19}$$

where $\mathbf{d} = \langle g | \hat{\mathbf{p}}_n | e \rangle$ the dipole matrix element of the transition of the dipole moment operator $\hat{\mathbf{p}}_n = \mathbf{d}^* \hat{\sigma}_n^+ + \mathbf{d}\hat{\sigma}_n^-$ for the n^{th} emitter. Therefore, $\hat{\mathbf{E}}^+(\mathbf{r}_m)$ in (1.18) is the total guided-mode field and is given by the sum of the driving electromagnetic field and the field re-scattered by all other dipoles at the position $\mathbf{r}_m$ of the m^{th} dipole.

The Hamiltonian in (1.15) contains all the details of the system. For our purpose we can simplify to an equation that governs the dynamics. To do so, we make use of the master equation to describe the evolution of this

system, in the Born-Markov approximation. For this approximation to hold we make the assumption that the decays in the ensemble are much slower than any time-scale of the environment. In other words, we assume that the environment is broad in frequency, such that it can be considered flat over the resonance frequency ω_0 of the dipole, hence $\omega \to \omega_0$[7]. In this approximation, the photonic degrees of freedom can be traced out and we arrive to an effective dipole-dipole Hamiltonian. The evolution of the system can then be derived by $\dot{\rho} = -\frac{i}{\hbar}[H, \rho] + \mathcal{L}[\rho]$, where ρ is the density matrix of the dipole. Within the rotating wave approximation and in the rotating frame of the guided-mode driving field frequency ω_p, the Hamiltonian and the Lindbladian considered are [81],

$$\begin{aligned} H =& -\hbar\Delta \sum_{m=1}^{N} \hat{\sigma}_{ee}^{m} - \hbar \sum_{m,n=1}^{N} J_{mn} \hat{\sigma}_{m}^{+} \hat{\sigma}_{n}^{-} \\ & - \sum_{m=1}^{N} \left[\mathbf{d} \cdot \hat{\mathbf{E}}_{p}^{-}(\mathbf{r}_m) \hat{\sigma}_{m}^{-} + \mathbf{d}^{*} \cdot \hat{\mathbf{E}}_{p}^{+}(\mathbf{r}_m) \hat{\sigma}_{m}^{+} \right], \\ \mathcal{L}[\rho] =& \sum_{m,n=1}^{N} \frac{\Gamma_{mn}}{2} \left(2\hat{\sigma}_{m}^{-} \rho \hat{\sigma}_{n}^{+} - \hat{\sigma}_{m}^{+} \hat{\sigma}_{n}^{-} \rho - \rho \hat{\sigma}_{m}^{+} \hat{\sigma}_{n}^{-} \right), \end{aligned} \tag{1.20}$$

with $\Delta = \omega_p - \omega_0$ the detuning between the guided-mode driving field and any of the identical emitters.

In this expression, the evolution is divided between the coherent part of the dynamics, contained in H, and the dissipative part described by the Lindbladian, $\mathcal{L}[\rho_A]$. In (1.20) the total Green's function $\mathbf{G}(\mathbf{r}_m, \mathbf{r}_n, \omega_0)$, is separated in its real and imaginary part as,

$$\begin{aligned} J_{mn} &= \frac{\mu_0 \omega_0^2}{\hbar} \mathbf{d}^{*} \cdot \mathrm{Re}\{\mathbf{G}(\mathbf{r}_m, \mathbf{r}_n, \omega_0)\} \cdot \mathbf{d}, \\ \Gamma_{mn} &= \frac{2\mu_0 \omega_0^2}{\hbar} \mathbf{d}^{*} \cdot \mathrm{Im}\{\mathbf{G}(\mathbf{r}_m, \mathbf{r}_n, \omega_0)\} \cdot \mathbf{d}. \end{aligned} \tag{1.21}$$

The two parameters J_{mn} and Γ_{mn} are referred to as the *coupling rates* of the interacting system and will be used to identify the nature of the coupling. Specifically, Γ_{mn} is called the *dissipative coupling rate* and contains the self Γ_{mm} and mutual Γ_{mn} decays between the dipoles. When it reaches its maximum value for a specific system, the coupling between the emitters is considered to be of dissipative character (J_{mn} = 0). For such a coupling, a photon from the decay of an emitter is absorbed and re-emitted by an adjacent one. The symmetric (superradiant) and anti-symmetric (subradiant) states are in this case degenerate in energy, and maximally modified in the decay rates as $\Gamma_{+} = N\Gamma$ and $\Gamma_{-} = 0$, with respect to the single emitter, Γ. Hence, super- and subradiant emission manifest in the dissipative coupling

[7] Equivalent to neglecting the frequency dependence in the Greens function above.

regime. The energy diagram for this limit is illustrated in Figure 1.5(a) for the simplest collective system of two emitters.

J_{mn}, is called the *dispersive coupling rate* and is related to the dipole-dipole coupling, containing $1/r_{mn}^3$ terms, as well as the long-range, waveguide-mediated interaction. For a maximum J_{mn}, the emitters exhibit a flip-flop interaction via the exchange of virtual photons, that exert an electromagnetic force on them. As a result, the symmetric and anti-symmetric levels shift apart in energy by a maximum of $2J_{mn}$ (Figure 1.5(b)), while both states decay with the single emitter rate, Γ. This term is associated with the dispersive coupling regime ($\Gamma_{mn} = 0$), often described as the collective Lamb-shift[8] [82].

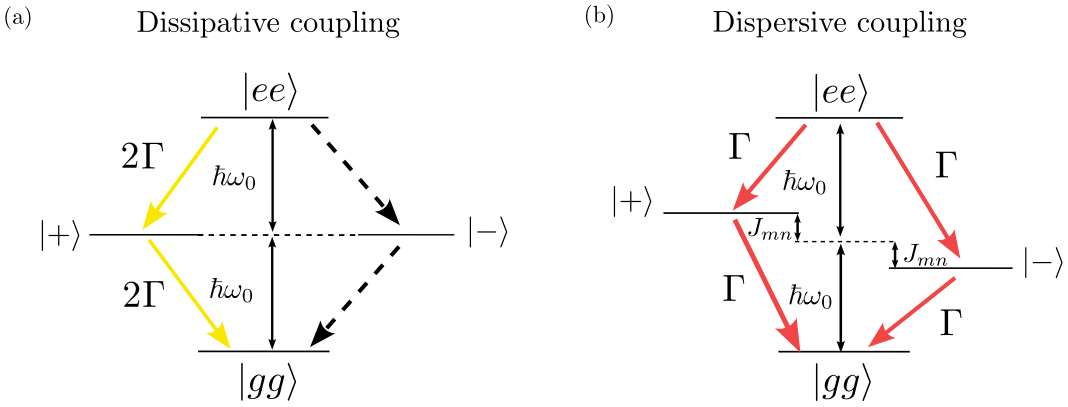

FIGURE 1.5: Illustration of the energy diagrams for the two coupling regimes. The system considered is of two emitters for simplicity. (a) Dissipative coupling, where the symmetric, $|+\rangle$ and anti-symmetric $|-\rangle$ states are degenerate in energy, but maximally modified in the decay rate, and (b) Dispersive coupling, where the $|+\rangle$ and $|-\rangle$ are maximally shifted apart in energy.

From (1.21) it becomes clear that the dipole-dipole interaction depends on the inter-emitter separation $r_{mn} = r_m - r_n$, included in the Green's function. The exact calculation of $\mathbf{G}\left(\mathbf{r}_m, \mathbf{r}_n, \omega_0\right)$ is challenging and often derived numerically, given the geometry of the dielectric media [48]. However an effective model can be constructed with basic assumptions for certain structures, that allow to estimate the Green's function for a region of interest analytically. In the next Section, we specifically address our structure of interest —the photonic crystal waveguide (PCW)— where the approximate Green's function reveals that the type of coupling in such nanostructures is in fact determined by the inter-emitter separation, r_{mn}. Thus, for this system, one could engineer purely dissipative or dispersive interactions by carefully tuning the distance between the emitters [34, 48, 65].

Having described the two coupling regimes, we note as a final remark here that the claims in Section 1.2.2 are accurate only when considering an ideal system, where permutation-symmetry is preserved, and for specific

[8]Here we note that the individual Lamb-shifts, owed to undesired guided or non-guided modes that would shift the dipole resonance frequency, are neglected since they can be directly included in ω_0.

inter-emitter separations, leading to dissipative coupling. In a real sample, the simple Dicke model breaks down when the Green's function is not permutationally symmetric. For example, in the case where the interactions between adjacent emitters are of different character, the symmetric states are not eigenstates of the system. Also, in the non-ideal sample, as brought up in the introduction, the doubly excited state may have a probability of decaying through the subradiant state (black dashed arrows in Figure 1.4(b)) with a certain rate ($\Gamma_- \neq 0$). Additionally, the degeneracy between $|+\rangle$ and $|-\rangle$ might be lifted due to imprecise positioning of the emitters, resulting in an intermediate type of coupling that combines dissipative and dispersive effects.

1.4 Collective dynamics of two emitters in a waveguide

Until now the collective effects of super- and subradiance have been described qualitatively for a system of closely positioned, interacting atoms in free space. From here on, we consider the system of two two-level emitters inside a waveguide, as shown in Figure 1.6. This environment will now mediate the interaction via photon absorption and re-emission by the emitters, theoretically extending it to an infinite range[9]. Such a photonic nanostructure, specifically a PCW, was employed for the work of this thesis. In this section, we introduce the theory that was developed to model our system (Supplementary Material of [56]), directing the discussion to the one-dimensional (1D) light-matter interaction of waveguide quantum electrodynamics (QED). The derivation of the expressions that follow are rigorously discussed in [34, 57, 65, 74].

In a PCW the emitters couple predominately to a single guided mode of the waveguide. It is therefore convenient to separate the Green's function in the 1D guided mode of the waveguide and the remaining non-guided ones as $\mathbf{G}\left(\mathbf{r}_m, \mathbf{r}_n, \omega_0\right) = \mathbf{G}_{wg}\left(\mathbf{r}_m, \mathbf{r}_n, \omega_0\right) + \mathbf{G}'\left(\mathbf{r}_m, \mathbf{r}_n, \omega_0\right)$. For the waveguide, the Green's tensor of the guided mode reads [47],

$$\begin{aligned}\mathbf{G}_{wg}\left(\mathbf{r}_m, \mathbf{r}_n, \omega_0\right) = & \, i\frac{\alpha\omega_0}{2u_g}\Theta(x_m - x_n)\mathbf{b}_k(\mathbf{r}_m)\mathbf{b}_k^*(\mathbf{r}_n)e^{ik(x_m - x_n)} \\ & + i\frac{\alpha\omega_0}{2u_g}\Theta(x_n - x_m)\mathbf{b}_k^*(\mathbf{r}_m)\mathbf{b}_k(\mathbf{r}_n)e^{-ik(x_m - x_n)}\,,\end{aligned} \tag{1.22}$$

where α is the lattice constant of the PCW, $u_g = \partial\omega/\partial k$ is the group velocity for the light propagating inside the waveguide, $\mathbf{b}_k(\mathbf{r}_m)$ is a 1D periodic function along the axis of the waveguide, Θ is the Heaviside function which determines the left (L) and right (R) propagating modes, k is the Bloch wavenumber and $x_{mn} = x_m - x_n$ the spacing between the m and n dipoles along the waveguide. The coupling rates J_{mn} and Γ_{mn} can be then rewritten

[9] Limited by losses and decoherences from imperfections of the structure and the environment.

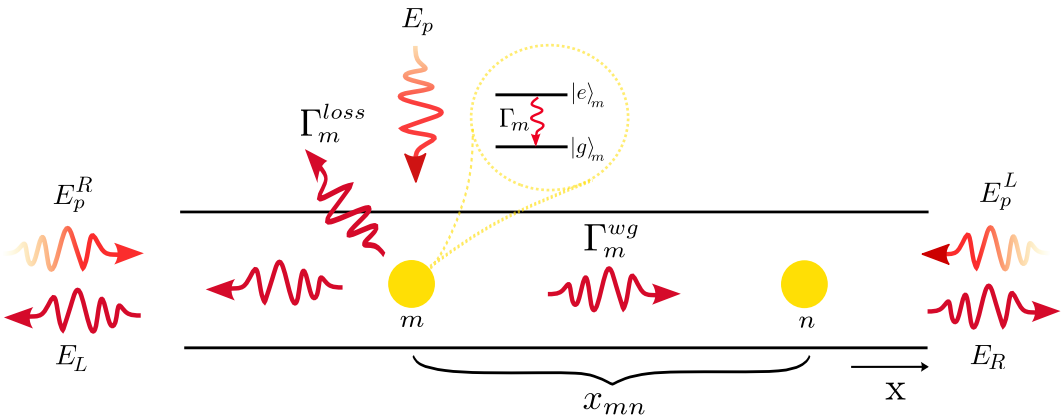

FIGURE 1.6: Two quantum emitters m and n, driven inside a waveguide, with spacial separation of x_{mn}. Each emitter is a two-level system with a ground $|g\rangle_m$ and an excited $|e\rangle_m$ state. The emitters can be driven through the waveguide, from the right E_p^R or left E_p^L, as well as from the top, E_p, depending on the experimental purpose. After excitation, the emitter m decays with a rate Γ_m. In non-directional structures, the emitter will decay with equal probability towards either of the two directions inside the waveguide, with a rate of Γ_m^{wg}, giving the output field E_R or E_L. In addition, part of the emission can leak out of the waveguide, with rate Γ_m^{loss}.

as $\Gamma_{mn} = \Gamma_{mn}^{wg} + \Gamma'\delta_{mn}$ and $J_{mn} = J_{mn}^{wg} + J'\delta_{mn}$, where δ_{mn} is the Kronecker delta [81].

To describe the evolution of the system, we make use of the Lindbald master equation described in (1.20). With the revised Green's function, the master equation is separated between the dynamics in the 1D transmission line of the waveguide and the non-guided part. Specifically, the latter will be included as a Liouvillian $\mathcal{L}_{loss}[\rho]$, describing the emission to modes other than the waveguide. In addition, to account for dephasing from the environment $\mathcal{L}_{dph}[\rho]$ is introduced. The complete master equation then reads (for $\hbar = 1$) [59, 65],

$$\dot{\rho} = -i[H', \rho] + \sum_{m,n} \frac{\Gamma_{mn}^{wg}}{2} \left(2\hat{\sigma}_m^- \rho \hat{\sigma}_n^+ - \{\hat{\sigma}_m^+ \hat{\sigma}_n^-, \rho\}\right) + \mathcal{L}_{loss}[\rho] + \mathcal{L}_{dph}[\rho]\,, \quad (1.23)$$

where now the Hamiltonian of (1.20) can be rewritten as,

$$H' = -\sum_m \frac{\Delta_m}{2}\hat{\sigma}_m^z - \sum_{m,n} J_{mn}^{wg} \hat{\sigma}_m^+ \hat{\sigma}_n^- + \frac{\Omega_m}{2}\left(e^{i\theta_m}\hat{\sigma}_m^+ + e^{-i\theta_m}\hat{\sigma}_m^-\right). \quad (1.24)$$

Here, we use $\Delta_m = \omega_p - \omega_m$ to account for differences between the emitters' resonance frequency. Compared to (1.20), the interaction of the dipoles with the input driving field is replaced by $\frac{\Omega_m}{2}\left(e^{i\theta_m}\hat{\sigma}_m^+ + e^{-i\theta_m}\hat{\sigma}_m^-\right)$, where $\Omega_m = \left|\mathbf{d}_m^* \cdot \mathbf{E}_p^R(\mathbf{r}_m)\right|/\hbar$ and θ_m the *driving phase*. The driving phase of an emitter will be more often mentioned in reference to a second one, as the relative

phase between them $\theta = \theta_m - \theta_n$ will be the useful parameter. The two Liouvilians included are described by,

$$\begin{aligned}\mathcal{L}_{loss}[\rho] &= \sum_m \Gamma_m^{loss} \hat{\sigma}_m^- \rho \hat{\sigma}_m^+ \\ \mathcal{L}_{dph}[\rho] &= \frac{\Gamma_{dph}}{2} \sum_m [\hat{\sigma}_m^z \rho \hat{\sigma}_m^z - \rho]\,,\end{aligned} \tag{1.25}$$

where Γ_m^{loss} is the decay rate of the m^{th} emitter in the non-guided modes, and Γ_{dph} is the dephasing rate, which is here assumed to be the same for all emitters for simplicity. Finally, the coupling rates are defined by (1.21) with the Green's function of the waveguide (1.22) as,

$$\Gamma_{mn}^{wg} = \frac{4\pi g_{k,m} g_{k,n}}{u_g} \mathrm{Re}\{e^{i\phi_{mn}}\} \quad \text{and} \quad J_{mn}^{wg} = \frac{2\pi g_{k,m} g_{k,n}}{u_g} \mathrm{Im}\{e^{i\phi_{mn}}\}. \tag{1.26}$$

Here, $\phi_{mn} = k|x_{mn}|$ is the *coupling phase*, which accumulates as the field propagates between the interacting emitters, depending on their spatial separation, $|x_{mn}|$. $g_{k,m} = -\mathbf{E}_k(\mathbf{r}_m)\cdot\mathbf{d}_m$, is the local coupling rate of the m^{th} dipole to the waveguide mode k, where $\mathbf{E}_k(\mathbf{r}_m) = \sqrt{\frac{\hbar\omega_k}{2\epsilon_0}}\mathbf{u}_k(\mathbf{r}_m)$ is the field amplitude with ω_k the frequency of the optical mode, ϵ_0 the vacuum permittivity and $\mathbf{u}_k(\mathbf{r}_m) = \sqrt{\frac{a}{L}}\mathbf{b}(\mathbf{r}_m)e^{ikx_m}$ the Bloch modes, constituting the periodic basis functions for a single band of the PCW, where L is the length of the waveguide[10] [47].

Using the relation $\Gamma_m\beta_m = 4\pi g_{k,m}^2/u_g$, the coupling rates can be written in a more intuitive form,

$$\Gamma_{mn}^{wg} = \sqrt{\beta_m\beta_n\Gamma_m\Gamma_n}\cos\phi_{mn} \quad \text{and} \quad J_{mn}^{wg} = \frac{1}{2}\sqrt{\beta_m\beta_n\Gamma_m\Gamma_n}\sin\phi_{mn} \tag{1.27}$$

where $\Gamma_m = \Gamma_m^{wg} + \Gamma_m^{loss}$, is the sum of all decays from a single emitter[11], inside the mode of the waveguide and out of it, while $\beta_m = \Gamma_m^{wg}/\Gamma_m$ is the coupling factor of an emitter m to the waveguide mode.

As mentioned in Section 1.3, from (1.27) it becomes clear that the coupling phase ϕ_{mn}; i.e., the inter-emitter spacing $|x_{mn}|$, is the parameter that determines the nature of the coupling in the system. Specifically, one can deduce from the relations above that for $\phi_{mn} = (N + 1/2)\,\pi$, where N an integer[12], the emitters exhibit dispersive coupling ($\Gamma_{mn}^{wg} = 0$) and unchanged decay rates compared to those of the uncoupled emitters. For $\phi_{mn} = N\pi$ the dissipative coupling ($J_{mn}^{wg} = 0$) leads to super- and subradiant states

[10] Since the waveguide obeys time-reversal symmetry, $\mathbf{E}_k = \mathbf{E}_{-k}^*$ holds, meaning that the periodic function is also real in backward direction ($\mathbf{u}_{-k} = \mathbf{u}_k$).

[11] There is also part of the decay that might happen through non-radiative processes, which are not included here.

[12] Not to be confused with the number of emitters.

with maximally modified decay rates. More intuitively, ϕ_{mn} is the parameter that defines the interference of the radiation field emitted into the PCW and scattered from each of the emitters, as they switch excitations back and forth. Hence, for $\phi_{mn} = N\pi$ the field emitted by the coupled system interferes either constructively or destructively, yielding super- or subradiant emission, respectively.

Finally, to provide a more direct understanding of the physics behind the coupling, a simplified analytical approach is employed. For that, the dephasing will be neglected and only the dynamics in the single-excitation subspace will be considered. This treatment is valid when driving only one of the emitters, with a pulse much shorter than their individual lifetimes. In this case, (1.23) can be written as

$$\dot{\rho} = -i\left[H_{\text{eff}}\rho - \rho H_{\text{eff}}^{\dagger}\right], \tag{1.28}$$

where the effective Hamiltonian H_{eff} is given by[13],

$$H_{\text{eff}} = \sum_{m,n=1}^{2}\left(J_{mn} - i\frac{\Gamma_{mn}}{2}\right)\hat{\sigma}_m^{+}\hat{\sigma}_n^{-} + \sum_{m=1}^{2}\left(\Delta_m - i\frac{\Gamma_m^{loss}}{2}\right)\hat{\sigma}_m^{+}\hat{\sigma}_m^{-}. \tag{1.29}$$

The first term accounts for the interaction of the two dipoles via photon emission and re-absorption in the waveguide, and the second contains the dipole Hamiltonian and the non-guided terms of the dynamics.

In the evolution described by (1.28), the jump terms, representing the state of the system after the decay, essentially preparing it in the collective ground state $|gg\rangle$, have been omitted. As this state does not emit light, the full dynamics of the system can be understood within the so-called no-jump formalism used here[14]. However, if the emitters undergo dephasing, are re-excited, or simultaneously driven populating $|ee\rangle$, the system exits the single-excitation subspace and the jump evolution becomes important. In these cases the full master equation (1.23) should be employed for a complete description of the dynamics in the system.

While H_{eff} provides valuable insights into the system's dynamics, numerical integration of the complete master equation (1.23) was used to simulate the experimental results of Chapter 4. As it will be demonstrated (in Figures 4.5 and 4.7), the present model succeeds in describing with very good precision the experimental data for both the single-emitter excitation scheme and the simultaneous driving of both emitters from the top of the waveguide.

[13] Here we drop the wg superscript at the coupling rates to ease the notation.

[14] Corresponds to the so-called no-jump evolution of the quantum Monte-Carlo wavefunction approach [83].

1.5 Summary and Connection

In the present Chapter we aimed to build the theoretical background required to motivate our experimental methodology and interpret the results. We started by introducing the collective phenomena of super- and subradiance, as the results of constructive and destructive interference, respectively, of the coherent emission from an ensemble of interacting emitters. In an ideal system, superradiance occurs when the individual fields lock in-phase, giving rise to a short pulse of high intensity, whereas for subradiance an even number of emitters should emit out-of-phase, canceling each other out. We then qualitatively discussed the superradiant Dicke ladder for an ensemble of closely spaced atoms and delved deeper into the smallest system, composed of two, under ideal conditions. The complete energy diagram of two coupled emitters provides an intuitive understanding of the modification of the decay rates, leading to super- and subradiance. It also highlights the fundamental aspect of the interaction, that in the single-excitation subspace of two coupled emitters, the presence of the non-driven one will double the rate of the coherent radiation ($\Gamma_+ = 2\Gamma$) or eliminate it ($\Gamma_- = 0$). Further we distinguished between the dispersive ($\Gamma_{mn} = 0$) and dissipative ($J_{mn} = 0$) coupling regime. We introduced their characteristic effects on the coupled system, emphasizing that the maximal modification of decay rates, resulting in super- and subradiance, occurs at the dissipative limit. Finally, considering photon-mediated coupling of two emitters through a shared waveguide mode, we showed that the inter-emitter separation $|x_{mn}|$, directly related to the coupling phase ϕ_{mn}, is the parameter that determines the nature of the coupling. This is easier seen in the expressions of the coupling rates Γ_{mn} and J_{mn}, from where it becomes evident that super- and subradiance reach their peak for a coupling phase of an integer number of π, $\phi_{mn} = N\pi$. The discussion concludes with the effective Hamiltonian that describes our experimental system of two coupled emitters embedded in a PCW, in the single-excitation subspace.

Having introduced the fundamental theoretical tools required for the present thesis, we proceed to describe the experimental in the following Chapter.

2 Experimental setup and equipment

This chapter includes a description of the platform, the optical components and the equipment used to conduct the experiments of this thesis. We begin by introducing briefly our quantum emitter and its tailored nanophotonic environment. Next, the structure of the sample is presented. We further describe the cryostat and the main optical setup employed to drive the emitters and collect the radiation, along with the two excitation techniques used throughout this work. Finally, the lasers, spectral filtering setups and detectors are outlined.

2.1 Quantum dots in a photonic crystal waveguide

For many fundamental experiments in quantum optics and applications in quantum technology, the initial requirement is to control a single quantum emitter by exciting it and coupling its emission to a single optical mode. Various quantum emitters have been explored for this purpose, with solid-state emitters having the advantage of enabling direct integration into photonic nanostructures. This allows to tailor the light-matter interaction, couple the emitter to a single optical mode and route single photons for further experiments. Our platform adopts a self-assembled InAs quantum dot (QD) as the quantum emitter, coupled to a photonic nanostructure [47]. In this section, we make a concise presentation of the self-assembled QD and its optical properties, introduce the relevant nanophotonic structure and describe the composition of the sample used for this thesis, layer-by-layer.

2.1.1 The self-assembled quantum dot

The QDs used in this work are grown with the Stranski-Krastanov method, relying on the self-assembly of InAs QDs inside a GaAs membrane. In this approach, the QDs are formed due to the intrinsic strain induced by the 7% lattice mismatch between the two semiconductor materials. Specifically, the QDs are grown on top of 1.5 monolayers of InAs, called the *wetting layer*, deposited on a GaAs (Figure 2.1(a)). After the wetting layer, the strain leads to the formation of randomly positioned clusters. These clusters are composed of approximately $10^4 - 10^5$ atoms each, forming small dome-like islands with varying diameters of $15 - 20$ nm and heights of $5 - 10$ nm. It is these islands that constitute the QDs.

InAs and GaAs are both semiconductor materials. Their continuum of electronic states are divided between two bands, the valence (VB) and the

conduction band (CB), separated in energy by a band-gap. In Figure 2.1(b) the band diagram of the InAs QD and the surrounding GaAs is illustrated. The two materials exhibit different band-gaps. As the InAs in enclosed within a material of larger bandbap, a three-dimensional (3D) quantum well is created. Due to this quantum confinement of electrons to nanometric dimensions, the continuum of electronic states of InAs become quantized. As a result, even though a QD consists of hundreds of thousands of atoms, it exhibits the optical properties of a single one, rightfully called an "artificial atom".

For a neutral QD ($|0\rangle$), the states of the valence band are fully occupied while the conduction band is empty. Under optical excitation of the QD with a laser beam, an electron moves to the conduction band, leaving behind a hole in the valence band. The electron-hole pair forms a bound state, referred as the *exciton*. After a certain time, corresponding to the lifetime of the excited state, typically of ~ 1 ns, the pair recombines, emitting a single photon. The frequency of the emitted photon depends both on the band-gap of the InAs material and the size of the QD, which determines the confinement potential. Variation of the QDs' dimensions due to the random growth process results in an *inhomogeneous broadening* among the emitters within the same sample, where the emitted photons range between $915 - 945$ nm in wavelength. This broadening poses a challenge for achieving interaction between different QDs, as they would need to be individually tuned to resonance.

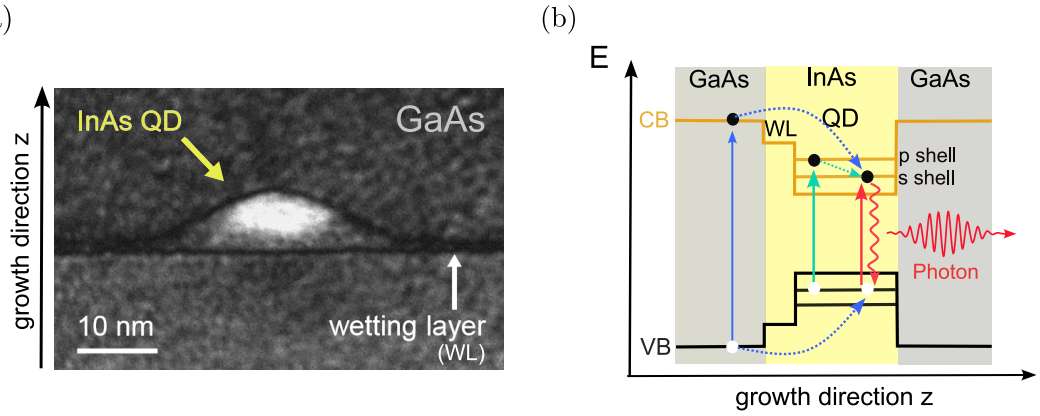

FIGURE 2.1: (a) Transmission electron microscope image of a self-assembled InAs QD embedded in GaAs. Adapted by [84] and [85]. Courtesy of Jean-Michel Chauveau and Arne Ludwig (b) Electronic potential of an InAs QD in GaAs. Smaller band-gap between the valence (VB) and the conduction band (CB) of the InAs, leads to a 3D quantum confinement. In turn, this creates the quantized energy levels of the QD. Three methods of optical excitation are illustrated; above band (ABB, blue), through the p shell (green) and resonant excitation (red). After excitation a pair of an electron (black disk) and a hole (white disk) is created, i.e., an exciton. Upon recombination of the electron-hole pair, a photon is emitted.

2.1.1.1 Optical excitation schemes

In order to create an exciton in the QD, different optical excitation schemes can be used. The three types exploited throughout this thesis are summarized in Figure 2.1(b). In the above band (ABB) driving (blue arrows), the excitation laser has much larger energy than the GaAs band-gap and the exciton is created in the bulk material of GaAs. From there the excited electron decays non-radiatively down to the lowest energy state of the conduction band in the QD (s shell), while the corresponding hole arrives at the higher energy state of the valence band. The electron-hole pair will then recombine at the ground state, and emit a single photon with the resonant frequency of the QD transition. This excitation scheme was used for the initial spectroscopy of the QDs, as it does not require any pre-characterization of the sample. Another way to create an exciton is to adjust the frequency of the laser beam to drive the electron to the second energy level of the conduction band, the p shell (green arrows). After few ps the electron relaxes through phonon processes to the s shell, from where it will decay radiatively and the electron-hole pair diffuses. This method of excitation is incoherent, due to the relaxation process it undergoes before the radiative decay, but can be particularly advantageous as it allows to filter out the excitation laser light from the photons emitted by the QD. Finally, the exciton can be created under resonant excitation, where the frequency of the laser exactly matches the QD transition (red arrows). This scheme conserves the coherence in the emission and different techniques are used to mitigate the laser background in the signal, as it now overlaps spectrally with the QD emission[1].

2.1.1.2 The neutral exciton

The electron-hole excitons discussed above are known as neutral excitons, X^0, as there is no additional, unpaired electron or hole to impose a charge on the QD. In the neutral exciton the electron e, has a spin of $S_e = 1/2, S_{e,z} = \pm 1/2$, that is indicate with $|\uparrow\rangle$ and $|\downarrow\rangle$ for the up and down spin orientations, and a heavy hole h, with angular momentum $J_h = 3/2, J_{h,z} = \pm 3/2$, denoted by $|\Uparrow\rangle$ and $|\Downarrow\rangle$ for up and down hole spin, respectively. From combinations of these, four bound states are formed, characterized by the projection of their total angular momentum $J_{ex,z} = S_{e,z} + J_{h,z} = -2, -1, 1, 2$, where ex stands for exciton. Of these four $J_{ex,z} = -2, +2$ are dark states, as only transitions with $\Delta J_{ex} = \pm 1$ are allowed by selection rules. The bright states of $J_{ex,z} = -1, +1$ corresponding to $|\downarrow\Uparrow\rangle$ and $|\uparrow\Downarrow\rangle$, can be excited with circularly polarized light, σ_+ and σ_- respectively, due to angular momentum conservation. These two states are degenerate in energy for a symmetric QD. However, a weakly broken QD symmetry[2], leads to an exchange interaction between the electron and the hole spins [86], which lifts this degeneracy of the exciton states by the fine-structure splitting (FSS). Consequently, the angular momentum J_{ex} is no longer a good quantum number,

[1] e.g. when exciting the QD from the top, walking the beam in its vicinity has shown to improve the signal-to-noise ratio (SNR). Here, noise translates to the laser background.

[2] as it can occur due to strain during the growth of the self-assembled QDs

and the energy eigenstates are symmetric and anti-symmetric linear combinations of the bright exciton states, $(|\downarrow\Uparrow\rangle - |\uparrow\Downarrow\rangle)/\sqrt{2}$ and $(|\downarrow\Uparrow\rangle + |\uparrow\Downarrow\rangle)/\sqrt{2}$, referred as the *x*- and *y-dipole*, respectively (Figure 2.2).

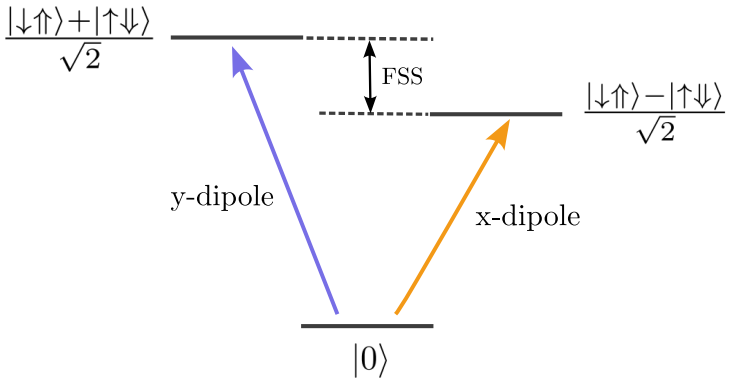

FIGURE 2.2: Energy level diagram of a neutral exciton. The two exciton states are shifted apart in energy by the fine-structure splitting (FSS) due to asymmetries in the geometry of the QD, and exhibit orthogonal linear dipoles, x and y. The neutral QD, $|0\rangle$, can then be excited to each of the two with a properly linear polarized excitation beam. Adapted by [87].

2.1.2 Light-matter interaction in a photonic crystal waveguide

Embedding a QD in a nanophotonic waveguide gives the ability to enhance its interaction with light and couples it to a single guided mode. Here, we focus on the nanostructure used for this thesis —a photonic crystal waveguide— and give a short description of its properties and effects on the QD emission.

2.1.2.1 Spontaneous emission of a two-level system

The fundamental phenomena where an excited two-level system eventually decays to its ground state emitting a photon, is known as *spontaneous emission* and is attributed to fluctuations of the vacuum. Considering the two-level system coupled to a continuum reservoir of optical modes with wavevectors k, its spontaneous emission can be described by the Wigner-Weisskopf theory[3] which predicts an exponential decay of the excited state of the emitter with a rate of,

$$\Gamma = \frac{\pi\omega}{\hbar\epsilon_0}|\mathbf{d}|^2\rho(\mathbf{r}_0,\omega,\hat{\mathbf{e}}_d), \tag{2.1}$$

and a Lorentzian emission spectrum of width Γ. Here, ω is the optical frequency of the dipole, ϵ_0 the vacuum permitivity, $|\mathbf{d}|$ the magnitude of the optical dipole, $\mathbf{r}_0$ the position of the emitter, $\hat{\mathbf{e}}_d$ the unit vector specifying

[3]Holds for the case where the local density of optical states is insignificant over a frequency interval comparable to the emitter linewidth.

the orientation of the transition dipole moment and ρ is the **local density of states** (LDOS). The LDOS defines the number of optical states at frequency ω per frequency bandwidth and volume at the position of the emitter, and relates to the local light-matter interaction strength.

From (2.1) it becomes clear that the spontaneous emission of an emitter can be controlled by modifying the LDOS in its environment. The enhancement of the decay rate can be quantified by the Purcell factor F_P, describing the decay rate inside the waveguide, $\Gamma(\mathbf{r}_0, \omega, \hat{\mathbf{e}}_d)$, relative to the decay rate of the same emitter in a homogeneous medium, $\Gamma^{hom}(\omega)$,

$$F_P(\mathbf{r}_0, \omega, \hat{\mathbf{e}}_d) = \frac{\Gamma(\mathbf{r}_0, \omega, \hat{\mathbf{e}}_d)}{\Gamma^{hom}(\omega)} \propto \rho(\mathbf{r}_0, \omega, \hat{\mathbf{e}}_d). \tag{2.2}$$

2.1.2.2 Photonic crystal waveguide

The LDOS can be efficiently modified by placing the emitter inside a nanostructure, like a cavity or a waveguide. Specifically, a photonic crystal waveguide (PCW) has been measured experimentally to increase the decay rate by $F_P = 9$ [88]. Figure 2.3(a), shows a scanning electron micrograph (SEM) of a PCW, similar to the one used for this thesis, engraved on top of a GaAs suspended membrane. The modification of the LDOS with this nanostructure is owed to the periodic modulation of the refractive index, determined by the characteristics of the photonic crystal, the lattice constant, α, and hole radius, r (inset of Figure 2.3(a)). This periodicity modifies the distribution of the electric field on the membrane and consequently the supported modes.

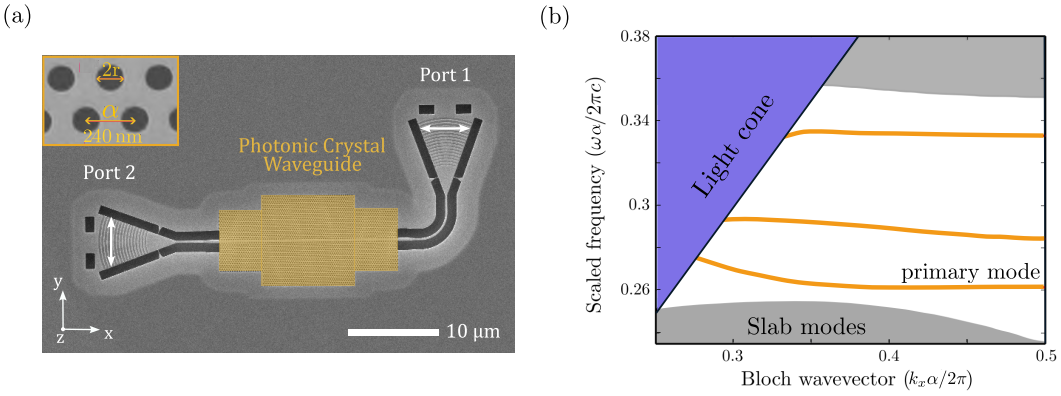

FIGURE 2.3: (a) Scanning electron micrograph (SEM) of a photonic crystal waveguide. The lattice constant (holes separation) α and hole radius r are 240 nm and 65 nm, respectively. (b) Band diagram of a GaAs PCW. Three TE-like waveguide modes (orange lines) appear in the band gap (white region between the two gray shaded areas). Lowest in energy is the primary mode, that is usually the one of interest, exhibiting a slow group velocity near the band edge (at $k_x\alpha/2\pi = 0.5$). Gray regions correspond to slab modes which are not confined in the waveguide, while the light cone contains the continuum of modes leaking outside the waveguide. Adapted from [47].

To elaborate, a photonic crystal is fabricated by etching holes, of radius r and periodicity α, into the membrane, with α comparable to the optical wavelength inside the material. This induces a periodic alternation of the refractive index between GaAs and air, leading to optical Bragg scattering of the light, with the propagating optical modes being Bloch modes. When the difference between the two refractive indices is large, Bragg scattering can suppress the propagation of optical modes for a range of frequencies in the membrane, giving rise to a *band-gap*. The band-gap frequencies are determined by the radius of the holes, their separation, the lattice structure, the thickness of the membrane, as well as the material of it. It can be therefore tailored to the frequency range of QDs. By removing a single row of holes from the photonic crystal, creating a defect to the periodicity, a number of guided modes are allowed to propagate through, and this row is now forms the *photonic crystal waveguide*, PCW. Figure 2.3(b) shows the resulting band diagram with the dispersion relation of the guided modes $\omega = \omega(k)$. The three modes appearing inside the band-gap of the membrane are confined in-plane (xy-plane) with the structure by total internal reflection in z and propagate along the x direction due to Bragg scattering in y. Therefore, the TE-like (transverse electric) modes propagating the waveguide will interact with the dipoles of the QDs within it. Of the three, the relevant mode with respect to the resonance frequencies of the QDs is the lowest in frequency, primary mode. This essentially establishes the PCW as a 1D single-mode optical system.

Near the low frequencies of the primary mode, at the edge of the Brillouin zone ($k_x\alpha/2\pi \rightarrow 0.5$), the dispersion relation in the photonic crystal flattens-out, leading to a low group velocity, $u_g = \partial\omega/\partial k$. This means that light at these frequencies slows down significantly in the membrane and therefore interacts with the corresponding QDs for longer. This occurs for frequencies near the so-called *band-edge* of the photonic crystal, where light below the band-edge frequency is prevented from transmitting the waveguide. Low group velocity means that the group index $n_g = c/u_g$ increases drastically close to the band-edge. Hence, as the maximum of the Purcell factor is $F_P^{max}(\omega) \propto n_g(\omega)$ [47], the LDOS increases proportionally to the group index, $n_g(\omega)$. Therefore the decay rate of a QD with a transition frequency close to the band-edge will be strongly enhanced[4]. Theoretically, the n_g diverges at the band-edge, but fabrication imperfection are preventing from such an observation [89]. In fact simulated values of the group index at the band-edge have shown $n_g = 58$ [90].

As a final remark, we note here that Purcell enhancement can become quite complex, as besides the spectral position of the QD with respect to the band-edge of the photonic crystal, it also depends on the emitter's spatial position, $\mathbf{r}_0$, within the waveguide, as well as its dipole orientation, $\hat{\mathbf{e}}_d$ [90].

Enhancement of the QD decay rate implies reduced interaction time with the noisy solid-state environment. This is harnessed as a remedy to mitigate

[4] Again as mentioned for the band-gap, the frequency of the band-edge can be tailored to approach the resonance frequencies of the QDs, as it depends on the lattice constant α and the holes radius r of the photonic crystal.

the effect of the fast noise, occurring on a timescale of $\sim$ 100 ps, from the elastic phonon scattering, known as *pure dephasing*. This phenomena serves as yet another source of decoherence, broadening the Lorentzian lineshape of the zero-phonon-line of the emission. Purcell-enhanced QDs, as those spectrally close to the band-edge of the photonic crystal, exhibit low pure dephasing leading to near-lifetime-limited coherence [91].

As the PCW essentially suppresses the emission of photons to modes other than the guided one, the QD couples efficiently to the single, well-defined mode of the waveguide. The parameter used to quantify the coupling of the emitter to the waveguide mode is the β-factor, given by

$$\beta = \frac{\Gamma_{wg}}{\Gamma_{wg} + \Gamma_{ng} + \Gamma_{nrad}}, \tag{2.3}$$

where Γ_{wg} is the decay rate in the waveguide mode, Γ_{ng} is the decay outside of the waveguide, hence in non-guided modes, and Γ_{nrad} is the decay rate through non-radiative processes[5]. β-factor is then essentially the probability of the emitted photon to be channeled through the desired waveguide mode. A coupling efficiency of $\beta > 98\%$ over a large bandwidth has been demonstrated experimentally with the current nanostructures, owed to the Purcell enhanced Γ_{wg} and to the reduced Γ_{ng} by the photonic crystal band-gap [88]. This results into efficient photon countrates by the deterministic emission from the QDs into the guided mode [18].

2.1.3 Sample

2.1.3.1 Sample growth

The wafer material used in this study is synthesized through molecular beam epitaxy[6]. Specifically, the self-assembled InAs QDs are formed in the center of a 180 nm-thin GaAs membrane (Figure 2.4(a)), atop a $\sim$1μm-thick sacrificial layer based on GaAs substrate [18]. The QDs are embedded in the center of this very thin membrane in order to maximize the probability of coupling to a single, TE-mode propagating the sample. During the growth of the membrane, the GaAs is doped such that a p-i-n diode with a Fermi level, E_F, fixed to the n-contact is structured. The doped regions generate a constant intrinsic voltage, V_{intr}, across the membrane, bending the conduction and valence band of the heterostructure, as illustrated in Figure 2.4(b). The wetting layer below the QDs brings a continuum of energy levels close to the emitters. To eliminate any coupling to this continuum of states, the QDs are capped with a higher band-gap material of AlAs [92]. On top of the emitters, a thick layer of AlGaAs is employed prior to the doped GaAs region. This serves as a tunnel barrier, since it assists further the controlled tuning of the emitters by restricting the flow of electrons through the QDs

[5] $\Gamma_{ng} + \Gamma_{nrad}$ is what we refer to as Γ_{loss} in Chapter 1.

[6] A piece from the "magical" B15027 wafer! All our wafers come from the team of Dr. Arne Ludwig in the University of Bochum.

to forward bias [19], and decreases the non-radiative exciton recombination, that could occur through tunneling. The sample is finally capped with a GaAs layer.

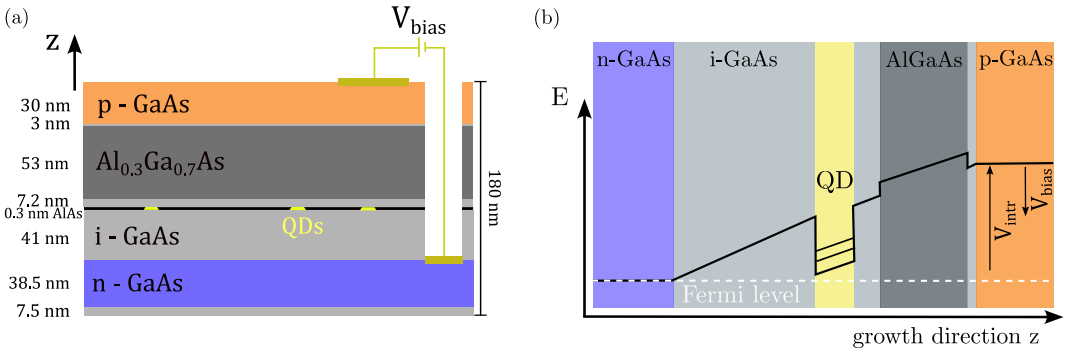

FIGURE 2.4: (a) Composition of the p-i-n heterostructure of the sample. Electrical contacts between the p- and n-doped layers are illustrated with the dark yellow wire. z is the direction of the QDs growth. Adapted from [18]. (b) Conduction band of one QD embedded in a p-i-n diode. The doped layers introduce an intrinsic constant electric field V_{intr}, which bends the conduction band. By applying an external bias, V_{bias}, the slope can be modified. Tuning the conduction band of the QD lower than the Fermi level, can lead to a negatively charged QD.

2.1.3.2 Photonic chip fabrication

From this wafer material, a 3 x 4 mm sample is cleaved to prepare the photonic chip we used. At first, electrical contacts to the diode are fabricated. For that, the sample is etched in certain regions down to the n-doped layer, followed by metal deposition to both p- and n- layers separately, for the formation of electrodes. Through those a bias voltage, V_{bias}, can be applied across the QDs. This feature gives accessibility to the properties of the emitters, as it allows for tuning of their emission frequencies via the DC-Stark effect (Figure 2.4(b)). Applying a positive bias will lower the intrinsic field of the diode. Reducing it further, so that a single conduction band reaches below E_F, can result in a charged QD through the tunneling of an electron from the n-doped layer. In addition, the p-i-n diode can be used to quench the charge noise of the solid-state environment, reducing significantly the *spectral diffusion*. Spectral diffusion is a consequence of the shift of the QD resonance due to the Stark effect caused by the charges surrounding the QDs. Over longer times ($\sim$ ms) these shifts of the resonance frequency effectively broaden the linewidth, $\gamma = \Gamma/2\pi$, defined by the radiative lifetime of the transition[7]. The implementation of the p-i-n diode mitigates this effect, enabling near-lifetime emission linewidths.

Next, the nanostructures, specifically designed for the project, are patterned with electron beam lithography. The PCW is connected to two shallow etched grating out-couplers (Port 1 and Port 2) through short

[7]Defined as: decay rate Γ, linewidth γ and lifetime of the transition $1/\Gamma$.

nanobeams (Figure 2.3(a)). To engrave the nanostructure on the sample, the holes of the photonic crystal and the nanobeams are etched through the membrane. Finally, the sacrificial layer below the membrane is chemically removed, leaving the structures suspended in air[8].

The PCW used in this thesis have a lattice constant of $\alpha = 240$ nm and hole radius r = 65 nm. The photonic crystal is composed of two regions, the so-called *slow* (broader) and *fast* (narrower) *light region*, exhibiting different u_g of the propagating light, with the latter serving as a mode adapter between the slow light PCW and the nanobeams. The grating out-couplers in both ends allow for coupling the light to and out of the photonic chip. By diffracting the emission in the waveguide out-of-plane with high efficiency and collecting the photons through the objective, the current devices have demonstrated > 60% chip-to-fiber coupling efficiency [94]. Their broad bandwidth of above 50 nm, allows for excitation and collection of almost the full spectral range of the InAs QDs in the waveguide. Moreover, they facilitate the suppression of the laser background in the signal by spatial and polarization selectivity. In particular, the input-output gratings are separated in space, and have orthogonal orientations, coupling to linearly polarized near-Gaussian modes in x and y for Port 1 and Port 2, respectively. In this way, the scattered input light at Port 1, going through the objective, can be rejected from the signal collected from Port 2. The nanostructures are commonly fabricated along the crystallographic axis of the wafer ([110] or [1$\bar{1}$0] [95]), such that either the x- or y-dipole of the QD has high probability of coupling well to the mode of the waveguide.

2.2 Optical setup

Exciting the QDs on demand and detecting their single photon emission, requires to ensure that thermal energy is below the confinement potential, eliminating the probability of thermal population of the QDs. Hence, the sample needs to be placed at the center of a cryogenic system.

To do so, the sample is glued[9] and wire-bonded on a PCB for electrical accessibility to the QDs. It is then fixed atop a stage of a three-axis stack of linear, piezo-driven nanopositioners, that is placed at the bottom of a dipstick. The sample is oriented with its z axis (Figure 2.4(a)) along the dipstick and electrical feedthroughs[10] from BNC connectors at the top of the dipstick, reach the PCB. Right above the sample there is a low-temperature compatible, apochromatic microscope objective, of numerical aperture NA = 0.81 and focal length f = 2.93 mm, suitable for near-infrared wavelength range (LT-APO/NIR/0.81). Through that objective, the laser light reaches the sample highly focused, gets efficiently collected, and the sample is imaged under white light. Moving upwards on the dipstick, a 4f lens system

[8] More details about the fabrication procedure can be found in [18] and [93].

[9] with silver paste for thermal contact.

[10] connecting to ultra-low noise voltage source (lower than 1 μV_{RMS} output voltage noise), from Basel Precision Instruments.

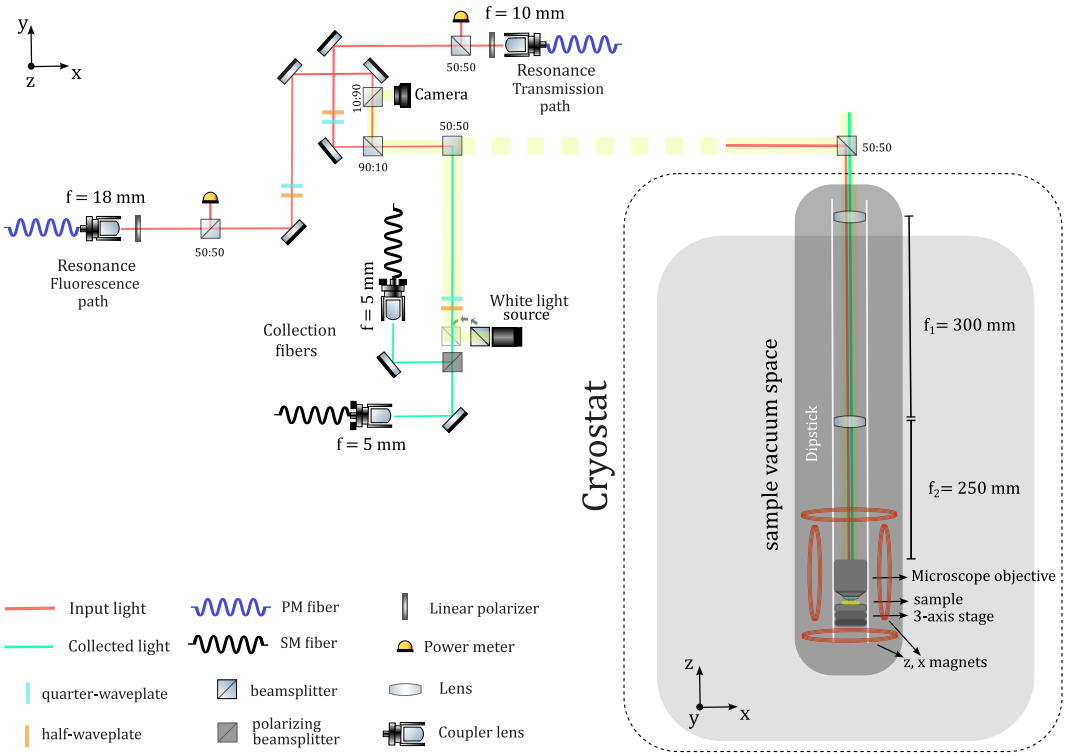

FIGURE 2.5: Illustration of the cryostat with the sample (contained in the dashed loop) and the primary optical setup of the breadboard on top of it. The excitation light going to the cryostat from the Resonance Transmission (RT) and Resonance Fluorescence (RF) paths is indicated with a red line. The laser reaches the sample by reflecting downwards on the 50:50 beamsplitter on top of the dipstick, and going through the microscope objective. The signal from the chip, indicated with blue line, is now transmitted through the same 50:50 beamsplitter, and collected by the single-mode fibers.

fixed in the optical path follows the objective. This is used as an optical relay for the alignment of the laser on the sample, while it also limits the losses from diffraction. The dipstick is top-loaded in the center of a closed-cycle cryostat[11] that operates at 4K, with ∼50 mbar of helium gas inside the sample space, to ensure thermal contact for efficient heat dissipation from the cold finger.

To send light to the sample, a breadboard with fibers and optical components fixed on top of the cryostat, guides the light to the center of the dipstick. The laser light arrives to the breadboard through polarization maintaining optical fibers. The beam is collimated at their output with a coupler lens of different f, determined by the excitation technique they would serve. Two optical paths for excitation are prepared on the breadboard. One is dedicated for driving the emitters from the top of the waveguide, and the

[11] AttoDRY1000 with 5/3T magnet from Attocube (aka: HyQ cryo)

other to couple the light through it, using the grating couplers. For the excitation from the top, also referred to as *Resonant Fluorescence* (RF), f = 18 mm is used resulting to a diffraction-limited beam spot (of $\sim$ 1 μm diameter) on top of the waveguide. For the excitation through the waveguide, also known as *Resonant Transmission* (RT), a lens of f = 10 mm is used to create a larger spot on the sample, allowing for efficient coupling to the grating ports. Subsequently, in both RF and RT paths the light goes through a linear polarizer, to ensure a well defined starting polarization of the beam. Part of the light is sent to a power meter fixed on the reflecting side of a beam splitter (BS) in the optical paths. The optical power measured is then stabilized with a feedback loop from the power meter, through a PID controller and an Acousto-Optic Modulator (AOM) setup. The excitation beam in both paths is further passed through a pair of half ($\lambda/2$) and quarter ($\lambda/4$) waveplates on motorized mounts, for polarization control. Finally, the two paths are combined on a BS and are both reflected downwards to the center of the cryostat, by a 50:50 BS[12] at the top of the dipstick. The collimated beam then continues through the 4f system and the objective to reach the photonic chip.

The light diffracted from the grating coupler used as the collection port of the nanostructure, follows the same path upwards. It instead now transmits through the same 50:50 BS at the top of the dipstick and is sent to the collection path of the breadboard. After another pair of $\lambda/4$ and $\lambda/2$ waveplates, a polarizing beam splitter (PBS) separates the collection in polarization to two single-mode fibers, with fiber-couplers[13] of f= 5 mm. One will collect the x- (horizontal) and the other the y- (vertical) polarization, depending on the port of the PCW we choose to collect from.

With a flippable 50:50 BS in the optical path of the collection, we can send diffused white light, back to the dipstick and illuminate the sample. The light reflected from the sample is imaged by a CMOS camera[14], that is placed at the reflection side of a 10:90 BS, added in the RF path.

The current cryostat, contains superconducting magnets in x and z orientation, that can reach up to 3 T and 5 T, respectively. This allows us to apply an external magnetic field over the sample, which, as we will see, will play an instrumental role in the QD coupling experiment.

2.3 Excitation techniques

Throughout the thesis, two excitation methods will be used: the Resonance Transmission (RT) and Resonance Fluorescence (RF). In RT (Figure 2.6(a)), the beam spot of the laser is usually aligned on top of the coupling grating Port 2, with a small angle. The light couples into the waveguide (optimally at about 8.4°) and while propagating through, it interacts with a QD that is coupled to the same mode. In the case where the light is resonant

[12] A 10:90 BS could be consider for more efficient collection. A 50:50 was used in this case, as high power in excitation was a requirement for a potential future experiment.

[13] Fiber-coupler 60FC-SFF-4M5-10 from Schäfter & Kirchhoff.

[14] DCC1645C USB 2.0 from Thorlabs

with the QD transition, and the QD is not saturated by the driving, the photon will be absorbed and re-emitted in the direction opposite to the laser light propagation. It will be essentially reflected by the QD, towards Port 2[15]. Higher-photon components of the laser will be transmitted to Port 1, along with photons that are off-resonant to the QD transition. Hence, under RT excitation with a coherent light source, the spectra of a QD will reveal an *RT dip* at the resonance frequency, due to the reflection of the single-photon component. Importantly, the shape of this dip is directly related to the decay rate, Γ, of the QD transition. The photons that reach Port 1 scatter off the chip with the same optimal angle. Through the objective, the light is directed to the collection fiber in the transmission of the PBS (Figure 2.5), aligned with the x-polarization of Port 1 (Section 2.1).

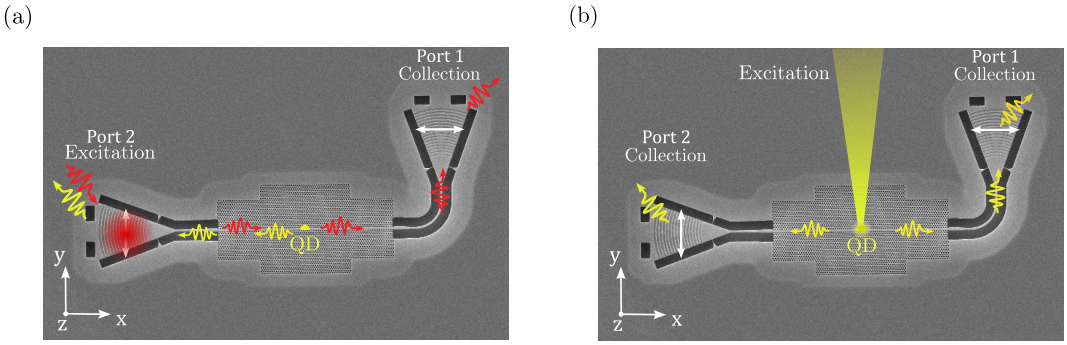

FIGURE 2.6: Illustration of the excitation techniques of a QD, by (a) Resonant Transmission (RT) and (b) Resonant Fluorescence (RF). (a) In RT the laser is aligned to one of the grating couplers (Port 2). When the light is resonant with the transition of the emitter, the QD will absorb and re-emit the light in reflection (yellow photons), allowing only off-resonant photons to transmit (red photons) in weak excitation. (b) In RF the QD is excited from the top of the waveguide and has equal probability of emitting photons in either of the two directions. Figure adapted by [87].

In RF excitation (Figure 2.6(b)), the diffraction limited beam spot is aligned well focused on top of the waveguide, at the known position of the QD. Part of the light will couple to the waveguide and excite the emitter. The polarization of the beam can be adjusted by the quarter- and half-waveplates on the RF excitation path (Figure 2.5), according to the orientation of the QD dipole that we want to drive. The photons emitted by the QD will propagate towards either of the ports with equal probability in the (non-chiral) PCW.

2.4 Excitation lasers

Two lasers were employed for the entirety of this thesis. A continuous-wave (CW), tunable laser[16] with wavelength range 910-980 nm and typical

[15] In other words, the emitted photon interferes destructively with the laser light in transmission after the QD.

[16] CTL950 from Toptica

linewidth < 10 kHz, was used for spectroscopy in Chapter 3 and photon-coincidence measurements in Chapter 5. To stabilize the driving frequency to a precise value, part of the beam is directed to a wavemeter[17] which, through a feedback loop, enables to lock the frequency of the laser to the desired value, with 60 MHz absolute accuracy.

For the time-resolved dynamics measurements presented in Chapter 4, we used a mode-locked Ti:Sapphire laser[18] with about 10 ps pulse duration[19], as given by the autocorrelator signal, and 80 MHz repetition rate. Such a pulse corresponds to about 32 GHz transform-limited bandwidth, considering a sech^2 temporal pulse shape. To address the much narrower QD transitions more efficiently, the beam goes through a 4f stretcher setup, similar to the one described in [96]. In short, the beam is initially expanded by a pair of lenses, obtaining a diameter of 25 mm on a diffraction grating. The reflecting diffraction grating[20] of 1200 grooves/mrad, disperses the light as 0.74 nm/mrad to its spectral components. A big lens of $f = 750$ mm focal length in the optical path, focuses the beam onto a mirror placed in the Fourier-plane of an effective 4f system. Mounted on the mirror is an adjustable slit with micrometer precision and the mirror is fixed on a linearly movable stage. By choosing the angle of the grating and the position of the mirror-slit component perpendicular to the beam, we can select the desired central frequency. The opening of the slit will define the FWHM bandwidth of the stretched beam. The selected frequency is reflected following the same path backwards. In order to separate the input beam from the output, a PBS and a quarter-waveplate are placed[21] before the expansion lenses. The input beam will be transmitted through the PBS and get a circular polarization after the quarter-waveplate. Upon reflection on the Fourier-plane mirror, the beam acquires a pi-phase shift that will reverse the handedness of the circular polarization. This leads to a vertical polarization after the quarter-waveplate, and thus to reflection by the PBS, separating from the input light. After the stretcher the pulse on the spectrometer has a bandwidth of ~ 91 pm. Correcting for the instrument response of the spectrometer, that is 24 pm [87], and considering a Gaussian pulse shape after the stretcher, the resulting pulse is 29.3 GHz FWHM with a duration of 15 ps.

2.5 Filter boards

The collected light from the sample undergoes frequency filtering to separate the emitters signal from the noise, before directed to the detectors. For the measurements done by off-resonant excitation (ABB, through the p shell or a higher-energy level, Section 2.1.1.1), the laser frequencies were most

[17] WS-7 from HighFiness.

[18] Tsunami from Spectra Physics.

[19] 10 ps FWHM from autocorrelator should come from a 6.6 ps pulse duration for a $sech^2$ pulse.

[20] Near-IR ruled reflective diffraction grating, at 750 nm blazed wavelength from Thorlabs.

[21] This is not optimal for the grating that is polarization-sensitive to our wavelengths.

commonly about 6 THz higher than the resonance of the emitters. To filter out the laser, a reflecting diffraction grating[22] of 22.1 GHz FWHM bandwidth and 65 % efficiency was used [96].

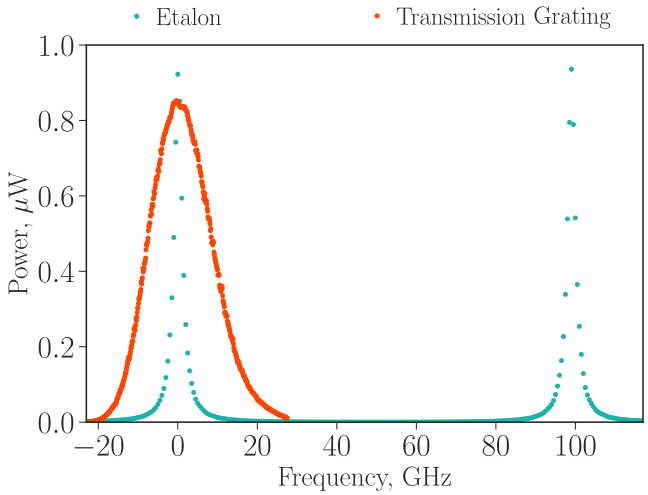

FIGURE 2.7: Individual transmissions through the transmission grating (red) and the etalon filter (light blue). The free spectral range, FSR, of the etalon, FWHM and relative efficiencies of both are identified.

In the case of resonant excitation, the broadband, compared to the QD transition, pulsed laser, was filtered by the combination of a transmission grating[23] and a solid silica etalon filter. The transmission grating has a bandwidth of 18 GHz FWHM, and $> 80 - 90\%$ diffraction efficiency at 930 nm, depending on the polarization of the light (Figure 2.7 red). The etalon has a 100 GHz free spectral range (FSR), 3 GHz FWHM bandwidth and exhibits a measured efficiency of about 95% (Figure 2.7 light blue). Placing the etalon at a small angle with respect to the optical path, allows to separate the reflected undesired frequencies of the light from the signal. The central transmitted frequency can be selected with high precision and stability, by adjusting the thickness of the etalon. This can be controlled by regulating the etalon's temperature using a Peltier element, placed below its mount, and a PI-controller. The two filters are calibrated such that they are centered around the frequency of the QD transition.

2.6 Detectors

The detection systems used throughout the thesis were a spectrometer and three types of single photon detectors. The spectrometer was employed to identify the promising QDs, as well as for their initial spectroscopic investigation. The single photon detectors that were used for the rest of the experiments were avalanche photo-diodes (APDs), fast APDs and superconducting nanowire single photon detectors (SNSPDs). Depending on the needs of each experiment, the suitable detector was chosen with respect to

[22] Same type as the one described for the stretcher setup.
[23] GP3515N VPH Transmission Grating at 930 nm by Thorlabs

their efficiency and time jitter. Both the APDs and SNSPDs are fiber coupled detectors, with the latter being extensively used, due their high quantum efficiency (70% at 940 nm), and very low dark count rate (< 5 Hz). However, their temporal jitter, of 200 ps FWHM, would limit the resolution of dynamics happening at shorter timescales. The fast APDs were employed for most of the decay dynamics measurements, included in Chapter 4, due to their comparably low time jitter of 40 ps FWHM. This property is advantageous for the decay measurements of the coupled emitters, as it allows to resolve the fast (superradiant) emission. On the downside, as these detectors are free space systems, they have very low quantum efficiency (1%), which makes the measurements remarkably longer in duration. A table with the parameters of all three detectors can be found in [96].

The time taggers used depending on their availability were a PicoHarp300, with time precision < 12 ps RMS, or a Time Tagger Ulta[24] with time jitter 20 ps FWHM. The time jitter for both devices is low enough, that does not limit the timing resolution of the measurements themselves. For the time resolved measurements with pulsed excitation, an electrical signal was sent from a fast photodiode in the path of the laser, to one of the channels of the time tagger counter. This 'clock' signal was used as reference to tag the detected photons in time. For the coincidence measurements described in Chapter 5, electrical signals from two single photon detectors are connected to two channels of the time tagger, where one is selected as the reference to tag in time the photons arriving in the other.

2.7 Summary and Connection

This Chapter introduces the solid-state emitter embedded in the photonic nanostructure, that enables modification of its spontaneous emission. We further compiled a concise description of the platform, as well as technical information on the optical setup and equipment used to excite, manipulate and detect the emission from the QDs.

In the Chapter that follows we employ all components to investigate the sample with spectroscopy. We will look into identifying the suitable QDs for the observation of the collective phenomena, along with the parameter that will be used to tune the emitters into resonance with control.

[24] By PicoQuant and Swabian respectively.

3 Optical Spectroscopy

"So, where are the dots?" - Theory Prof. Anders Søndberg Sørensen in the lab

On the way to explore the coupling between multiple emitters with our platform, two requirements emerged from the beginning: (1) We needed to find at least two QDs well coupled to the shared waveguide mode, and (2) spectrally close to each other, such that they could be brought to resonance with an external tuning knob.

In this Chapter we identify the promising QDs for the experiments that follow. We perform basic spectroscopy, probe their tunability and estimate their spatial separations. At first, the emitters are selected spectrally through resonant transmission of the PCW and located spatially inside the waveguide via photo-luminescence. Next, an out-of-plane magnetic field is introduced as the tuning knob to bring the emitters into resonance with control. Closing, we image the QD candidates inside the PCW, to approximate the inter-emitter separations.

3.1 Identifying the emitters in resonant transmission

Starting with a new sample, to identify the promising QD candidates, we begin by performing RT measurements for different nanostructures. For this study the nanostructures of interest are PCWs, identical to the device shown in Figure 2.3(a). As described in Section 2.3 for an RT measurement, the CTL laser is shined with low power[1], well below the saturation of QDs, upon Port 2. Following, its frequency is scanned, initially for a broad range, with a step of 300 MHz. The light transmitted through the waveguide is collected from Port 1. For each frequency the counts are recorded for two bias voltages V_{bias}; at 0 V, to measure the laser background, and at 1.24 V, the voltage at which neutral excitons can be excited. With this method, for a PCW with lattice constant $\alpha = 240$ nm and hole radius r = 65 nm, we obtain the transmission spectrum shown in Figure 3.1(a).

We observe the band-edge of the waveguide[2] at about 318.4 THz and three transmission dips (RT dips Section 2.3) exhibiting good extinction, spectrally close to each other and the band-edge. These RT dips correspond to the frequencies for which the laser is on resonance with three different QDs inside the PCW (highlighted in yellow, orange and red). As mentioned

[1] 1 μW and filtered with OD 5.0 filter.
[2] Found at the $1/e$ of the maximal transmission.

in Section 2.3, under this excitation scheme, each QD would reflect back the resonant light instead, resulting in the observed dips in transmission.

The specific structure is selected among others, because of the large depth of the RT dips, which consists a criteria of both good coupling between the waveguide and the QDs (high β-factor), and low spectral diffusion and pure dephasing[3]. Operating with QDs that are well coupled to the waveguide mode and less susceptible to noises, naturally increases the chances for an efficient photon-mediated dipole-dipole interaction and improved coupling.

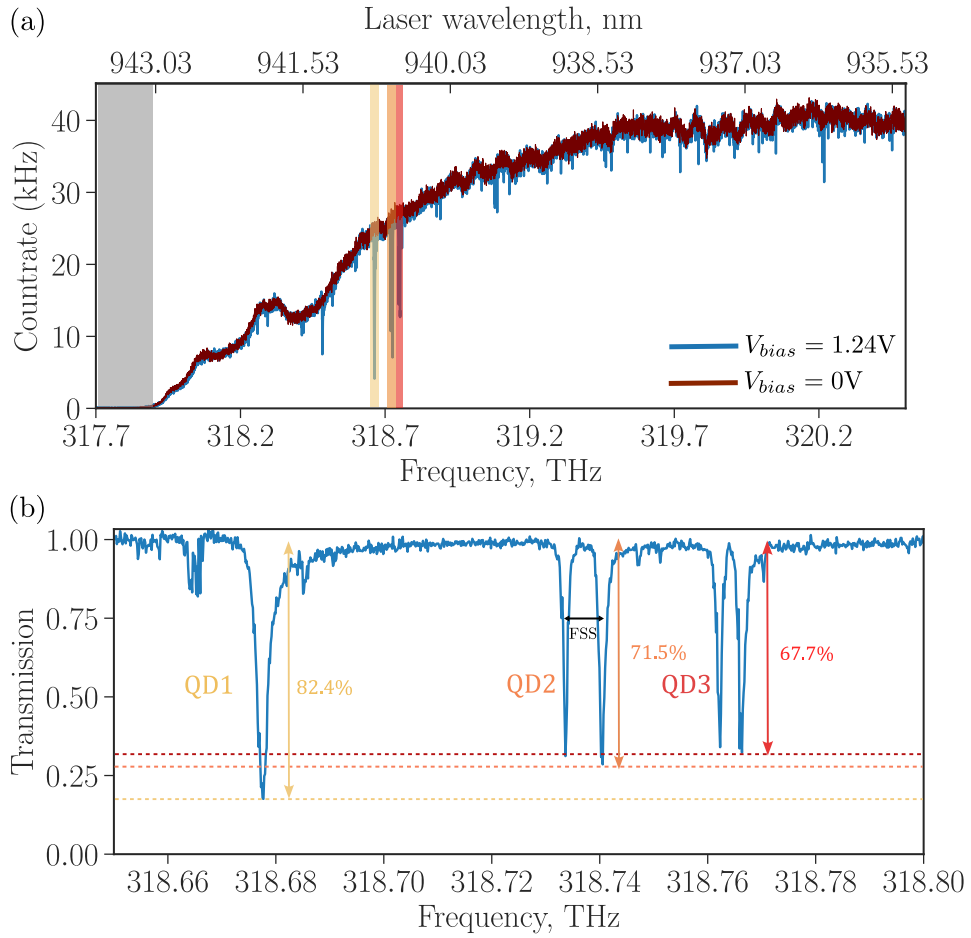

FIGURE 3.1: RT spectrum of the PCW containing the three well-coupled emitters at $B = 0$ T. (a) Off-resonance (brown) and on-resonance (blue) countrates were recorded, using $V_{bias} = 0$V and 1.24V, respectively. The colored lines: QD1 yellow, QD2 orange and QD3 red, are highlighting the spectral positions of the QDs with respect to the band-edge (band-gap: the gray shaded area). (b) Zoom-in RT at the region of the three emitters. Both x- and y-dipoles of QD2 and QD3 are coupled to the waveguide, while only one dipole of QD1 appears predominantly at $B = 0$ T. The FSS between the two dipoles is indicated for QD2.

[3]Due to the spectral position of the emitters with respect to the band-edge of the PCW, see Section 2.1.2.2.

From the tested nanostructures, on this sample we find that one out of three PCWs contained at least two QDs well coupled to the waveguide and spectrally close to each other. Given that the self-assembled QDs grow randomly in position and size, and the engraving of nanostructures on the sample is done with knowledge limited to the orientation of the crystallographic axis, this relatively high probability is attributed to the density of QDs, measured to be 10 μm^{-2} [85, 97]. However, scaling up to more emitters, would require deterministic positioning of the nanostructures on pre-localized QDs [98] or deterministic QD growth [99–101]. With the former demanding in its implementation and the latter in preliminary stage of fabrication, we for now rely on the high density of the QD wafer material.

Figure 3.1(b) shows a finer resolution scan around the frequencies of QD1, QD2 and QD3 at low power[4]. The scan reveals two dips at B = 0 T for each one of the three emitters. Those correspond to the linear x- and y-dipoles of the QDs, intrinsic result of the asymmetric QDs shape, due to the strain they experience during growth [47] (see Section 2.1.1). Their resonance frequencies for $V_{bias} = 1.26$ V and FSS (indicated in Figure 3.1(b) for QD2) evaluated from this measurement, are included in Table 3.1. The adjacent dipoles show a spectral separation of about 49 GHz and 21 GHz, between QD1-QD2 and QD2-QD3, respectively. From the spectra it becomes apparent that the low frequency (LF) dipole of QD1 is much better coupled to the waveguide mode ($\sim$ 82% maximum of transmission dip) than the higher (HF) one, while both dipoles of QD2 and QD3 show similar coupling ($\sim$ 71% and $\sim$ 67% respectively). These variations to the coupling of the different dipoles are related to the position of the emitters inside the PCW. Specifically, they are attributed to the varying local polarization of the PCW mode, leading to different projections of the QD dipole moments [90].

The transmission dips is fitted individually with the model described in [102]

$$T = \frac{[(\Gamma + 2\Gamma_{dph})((\beta-1)^2\Gamma + 2\Gamma_{dph}) + 4\Delta^2](1+\xi^2)}{(\Gamma + 2\Gamma_{dph})^2 + 4\Delta^2 + 4\beta\Gamma\Delta\xi + [((\beta-1)\Gamma - 2\Gamma_{dph})^2 + 4\Delta^2]\xi^2}, \quad (3.1)$$

where Γ is the decay rate of each dipole, Γ_{dph} the pure dephasing rate, β the β-factor, Δ the detuning between the laser frequency and the transition of the QD dipole, and ξ is the Fano-parameter. The latter originates from weak cavity resonances caused by reflections between the interfaces of the waveguide, inducing the observed asymmetry to an otherwise Lorentzian dip. To take the effect of spectral diffusion, σ_{sd}, into account, the above expression is convolved with a Gaussian distribution of detunings Δ centered around zero, and a standard deviation that corresponds to the spectral diffusion from the local environment.

To extract the decay rates, the spectral diffusion and β-factors of all dipoles, a power-dependent RT measurement at $B = 0$ T is recorded and fitted with the convolved function for each of the three emitters. Figure

[4]This scan was done for $V_{bias} = 1.26$ V, with 1μW power and an optical filter of OD 5.0, to ensure that the QDs will not be saturated.

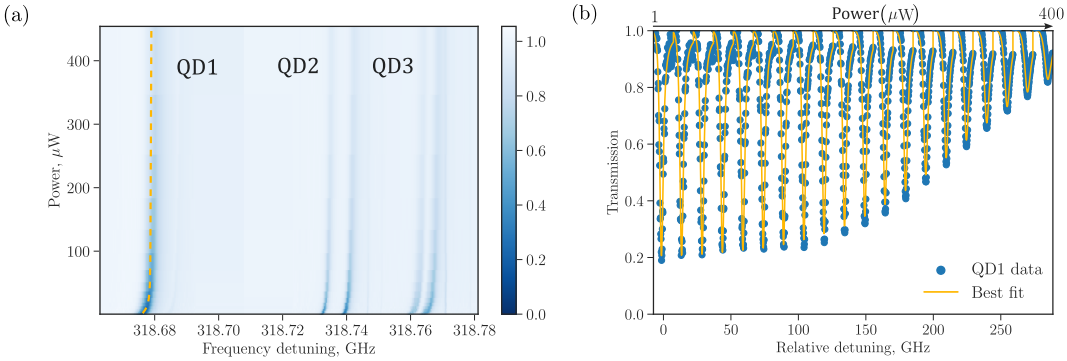

FIGURE 3.2: (a) Power dependent RT measurement for the three QDs. (b) RT dips of the LF QD1 dipole, at all powers, tracing the dash line in (a). The solid line is the result of modeling the experimental data, with the sum of multiple transmission dips given by (3.1), convolved with the Gaussian spectral diffusion.

3.2(a) shows the power-dependent RT for the three QDs. The single transmission dip of the QD1 LF dipole is fitted for all powers at once, with a sum of the above mentioned convolved functions. The resulting fit is shown in Figure 3.2(b)[5]. Respectively, for QD2 and QD3 the same procedure is followed, where now a product of two transmission dips of (3.1) is convolved with the Gaussian, to account for both x- and y-dipole of each QD. A sum of these is used to fit the two dips of QD2 and QD3 at all powers. For the entirety of the modeling, the pure dephasing is fixed at $\gamma_{dph} = 0.05$ GHz, where $\gamma_{dph} = \Gamma_{dph}/2\pi$ and the spectral diffusion is considered the same for both dipoles of each QD. Individual fits to the transmission dips at $B = 0$ T and $P = 1\,\mu$W are shown in Figure 3.3. The modeled parameters are summarized in Table 3.1.

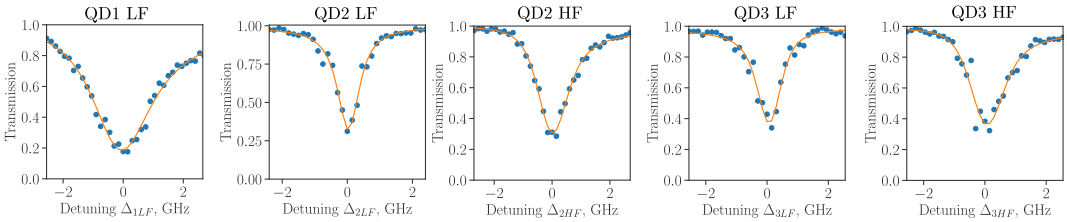

FIGURE 3.3: RT spectra of all five dipoles at B = 0 T. From left to right: low frequency (LF) dipole of QD1, LF of QD2, high frequency (HF) dipole of QD2, LF of QD3 and HF of QD3. The solid lines are fits to the transmission dips by (3.1) convolved with a Gaussian spectral diffusion.

Extracting precise values of these parameters solely through RT data is not straight forward. That is because the β-factor, pure dephasing and spectral diffusion, all contribute to the decrease of the RT dip [102]. A more thorough investigation of RT dip analysis is described in [103]. In our case, an optimal approach would have been to measure the decay rate of each dipole individually at $B = 0$ T, by performing lifetime measurements. This

[5]The transmission dips are shifted by a constant detuning for clarity of the plot.

way, one out of four free parameters would have been fixed and estimated independently.

3.2 Charge plateaus

To investigate the tuning range (voltage span) of our neutral excitons, we trace in RT the frequency-voltage plateau of each QD. For that we use once more the CW laser coupled to the waveguide from Port 2. The optical power is set to $1\,\mu$W and a filter in the excitation path with optical density of 5.0, ensures driving well below saturation. Assuming from Figure 3.1(b), that the resonant frequencies at $V_{bias} = 1.26$ V are approximately at the center of the plateaus, we scan the frequency of the laser for about 70 GHz (100 GHz) around the resonant frequency of QD1 (QD2), with a step of 50 MHz. For each frequency the laser is locked and the bias voltage is scanned with a step of 2 mV. The transmitted light is collected from Port 1 and measured with an APD. The results are depicted in Figure 3.4, where the transmission is normalized to the counts collected with non-resonant bias voltage (1 V), to correct for the laser background.

Each frequency-voltage plateau shows a stable QD emission tuning with the bias voltage applied. The three QDs show a Stark tuning of 0.62 GHz/mV for QD1, 0.69 GHz/mV for QD2 and 0.63 GHz/mV for QD3. From the current measurement, it is also confirmed that the pairs of dips seen in Figure 3.1(b) are two dipoles of the same QD, as they tune with the same slope (Figure 3.4(b)). The plateau abruptly disappears after 1.3 V, as for larger V_{bias} the QD gets charged with an electron that tunnels through the barrier of the intrinsic region of GaAs and jumps to a different energy, outside the measured spectrum.

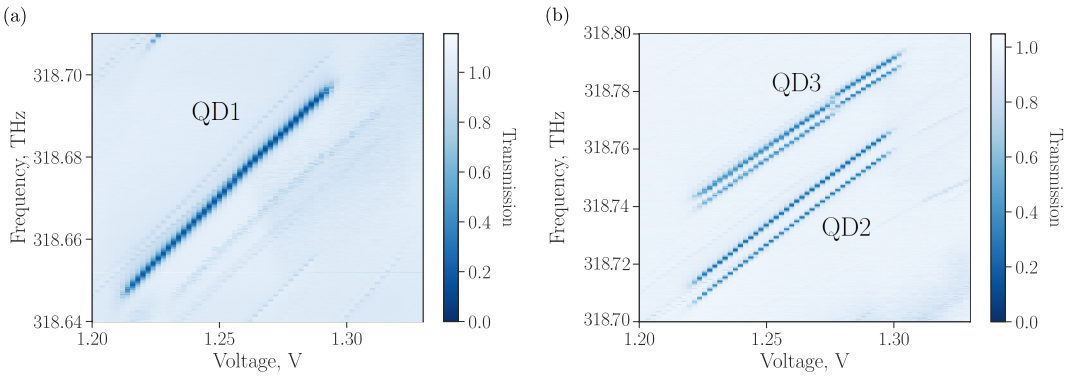

FIGURE 3.4: Frequency-voltage plateaus of the neutral excitons (X^0) of (a) QD1, (b) QD2 and QD3. At $B = 0$ T, only the LF dipole of QD1 couples to the waveguide mode, whereas both LF and HF dipoles of QD2 and QD3 appear in the RT spectra.

3.3 Magnetic field as the tuning knob

As mentioned in the introduction of this Chapter, to satisfy the last requirement for the coupling experiment, the emitters should be brought to resonance. From the charge plateaus it becomes clear that, with the current device, the electric field can not be used as the knob that would tune the frequencies of the QDs to resonance. This could have been made possible in a more dedicated design[6], that would allow for independent control over the electric field on each emitter locally [85, 104]. We then turn to make use of the magnets of the cryostat (Figure 2.5), which in x and z can produce an in-plane (Voigt configuration), or out-of-plane (Faraday configuration) magnetic field with respect to the sample, respectively.

3.3.1 Out-of-plane magnetic field on a neutral exciton

To elaborate on the effect that an external magnetic field has on a neutral exciton, we recall from Section 2.1.1.2 that in the absence of it ($B = 0$ T) the QD has two linear dipoles, $|x\rangle = (|{\downarrow}{\Uparrow}\rangle - |{\uparrow}{\Downarrow}\rangle)/\sqrt{2}$ and $|y\rangle = (|{\downarrow}{\Uparrow}\rangle + |{\uparrow}{\Downarrow}\rangle)/\sqrt{2}$, shifted in energy by FSS. Applying now an external magnetic field $\vec{B} = (B_x, B_y, B_z)$ of arbitrary strength and orientation on the neutral exciton, the FSS is extended by the Zeeman interaction of the electron and the hole spins with B, given by the Hamiltonian [86],

$$H_{Zeeman}(B) = -\mu_B \sum_{i=x,y,z} (g_{e,i} S_{e,i} - 2\kappa_i J_{h,i} - 2q_i J^3_{h,i})\, B_i, \tag{3.2}$$

where μ_B is the Bohr magneton, g_e is the electron g-factor, S_e the electron spin and J_h the hole spin, while κ and q are the valence-band parameters in the Luttinger-Kohn Hamiltonian, related to the material[7].

Using the magnet along the x axis to apply an in-plane B field (Voigt configuration), the two bright states at $B = 0$ T would both shift to higher energies with increasing B_x. It would therefore be unlikely to bring two QDs to resonance under this tuning field.

For an out-of-plane magnetic field (Faraday configuration) where B is oriented along the heterostructure growth direction z, (3.2) can be simplified to [86],

$$H^F_{Zeeman}(B) = -\mu_B (g_{e,z} S_{e,z} - \frac{g_{h,z}}{3} J_{h,z})\, B_z, \tag{3.3}$$

with $g_{h,z}$ being the effective hole g-factor[8]. Within this field the two bright dipoles of each QD shift apart with an increasing B_z field, due to their different symmetries. To elaborate, the linearly polarized x- and y-dipoles at $B = 0$ T transition to circularly polarized in the presence of a B_z field. Plugging in (3.3) the electron and hole spins for each exciton $\sigma_\pm$: $J_{ex,z} = \pm 1 \rightarrow S_{e,z} = \mp 1/2$, $J_{h,z} = \pm 3/2$ (see Section 2.1.1.2), we deduct the exciton energies

[6] An example of such a device is shown in Figure 6.1

[7] For InAs κ = 7.68 and q = 0.04 [105].

[8] Given by $g_{h,z} = 6\kappa_z + 13.5 q_z$ [86].

$E_{\pm,Zeeman} = \mp\frac{\mu_B}{2}(g_{e,z} + g_{h,z})\, B_z$. The two dipoles then exhibit an even and linear energy shift in opposite directions with increasing B_z due to Zeeman effect, with σ_+ shifting downwards and σ_- upwards in energy.

In addition, at large magnetic fields, the contribution of the exciton diamagnetic shift given by $\Delta E_{dia} = \sigma B_z^2$ becomes significant, causing a deviation from the purely linear behavior in the energy shift.

The bright exciton eigenstates for a neutral QD with reduced symmetry under a B_z field are then described by,

$$E_\pm = E_0 + \frac{1}{2}FSS \pm \frac{1}{2}\sqrt{FSS^2 + (\mu_B g_{ex,z} B_z)^2} + \sigma B_z^2, \tag{3.4}$$

where E_0 is the energy of the low frequency dipole of each QD at B_z = 0 T, FSS is the fine-structure splitting between the initially linear dipoles and $g_{ex,z}$= $g_{e,z}$ + $g_{h,z}$ is the exciton g-factor. From (3.4) we see that for each QD at B = 0 T we begin with a degenerate energy for both dipoles of E_0. Considering a QD with reduced symmetry, the degeneracy is lifted and the two bright dipoles split in energy by FSS. At low magnetic field the energy splitting varies quadratically with B_z. As B_z increases to values much larger than the exchange energy, the shift exhibits linear behavior, with the Zeeman effect dominating. For large values of B_z, the diamagnetic effect shifts equally both dipoles up in energy quadratically, independent of their polarization.

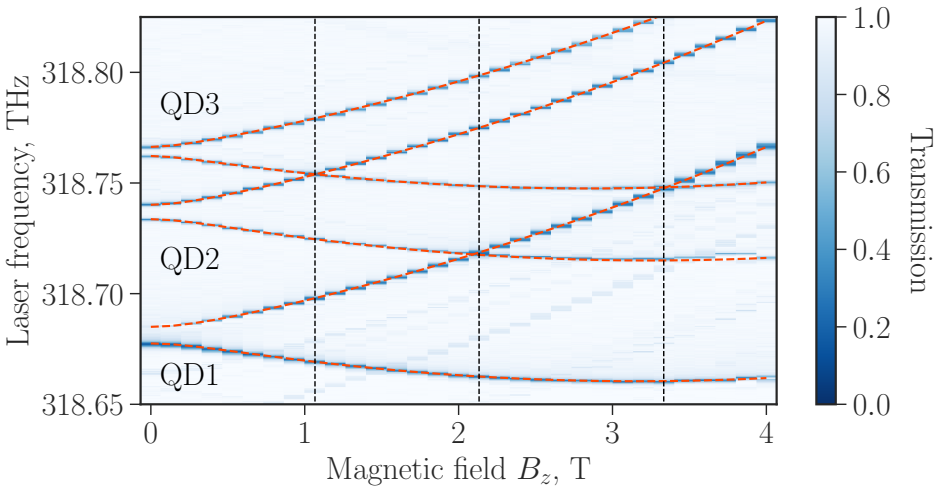

FIGURE 3.5: RT spectra of all three QDs at V = 1.24 V, as a function of the out-of-plane magnetic field, B_z. The red dashed lines follow the theoretical prediction for the Zeeman effect with a diamagnetic shift, while the black dashed lines are highlighting the B_z values where the dipoles of the different QDs come to resonance pairwise.

3.3.2 Tuning pairs of quantum dots to resonance

With the expected effects in mind, we exploit the magnet of the cryostat in z direction to impose an external magnetic field in Faraday configuration on our three QDs. To test the tunability, we repeat the RT measurement,

while sweeping B_z up to 4 T. Figure 3.5 shows the effect of the increasing B_z over the spectra of the three emitters. The red dashed lines are fits to the RT dips with (3.4).

We note that the RT dips of both dipoles for each QD exhibit approximately equal strength for the neutral exciton. This happens because the circularly polarized dipoles are projected onto the local linear polarization of the PCW, allowing them to couple equally well to the waveguide mode. As it will be mentioned later, it is for the same reason that the two opposite in polarization dipoles can couple when tuned to resonance—because they interact through the mode of the waveguide they couple in.

From Figure 3.5 it becomes clear that B_z is a suitable tuning knob for the relative detunings of the three QDs. We observe opposite dipoles of the three QDs coming to resonance pairwise, for three different values of B_z (black dashed lines). Specifically, the first crossing at $B_z = 1.07$ T is between QD2 and QD3, the second at $B_z = 2.13$ T between QD1 and QD2, and the third at $B_z = 3.33$ T between QD1 and QD3.

As the three QDs couple efficiently to the waveguide mode, exhibit low noise, owed to their spectral proximity to the band-edge of the photonic crystal, and can be tuned to resonance with control by an applied magnetic field, we focus the experiments for the entirety of the thesis on these three emitters.

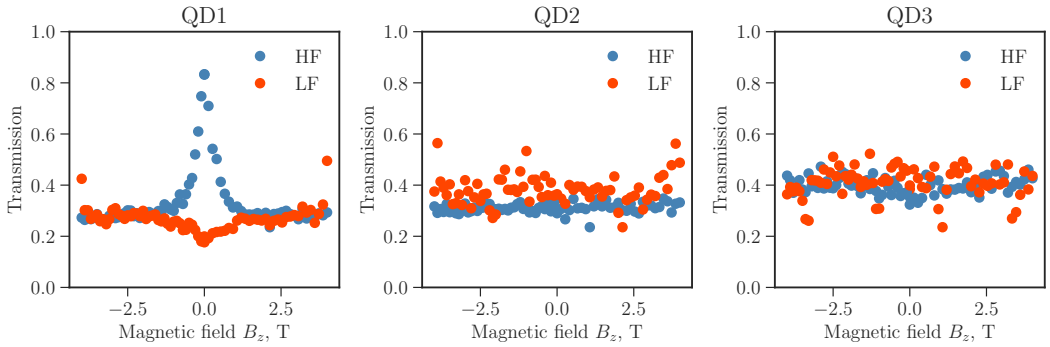

FIGURE 3.6: Amplitude of transmission dips as a function of the magnetic field B_z, for the high frequency (HF) and low frequency (LF) dipoles of the three emitters. The symmetry around B_z = 0 T confirms the absence of chirality in the device.

Before moving on, the chirality of the structure was tested, by comparing the RT dips of Figure 3.5, to counts from an identical RT measurement at negative B_z values. The resulting spectra are a mirror image of Figure 3.5. Figure 3.6 summarizes the amplitudes of the transmissions of each dipole (HF and LF) for the three emitters, for $B_z = [-4, 4]$ T. All six dips exhibit symmetry around $B_z = 0$ T, verifying the absence of chirality in the coupling of the QDs to the waveguide mode.

3.4 Resonant fluorescence

The QDs are also probed in RF. For that, we need first to find the position of the emitters inside the waveguide. To do so, we initially use a CW laser to mark the resonant frequencies of the QDs on a spectrometer and then perform excitation through a higher-energy state, while scanning the position of the laser on top of the waveguide. Obtaining counts on the spectrometer at the marked frequencies indicates that we have successfully located the QDs of interest. In the paragraphs that follow we describe this procedure in more detail.

We begin with the CW laser aligned through the RF path (Figure 2.5), focused on top of the waveguide. Locking the laser to the central frequency of the charge plateau for each QD (corresponding to $V_{bias} = 1.26$ V in Figure 3.4) we collect the light coupled to the waveguide from Port 1 and direct it to a spectrometer. The three central frequencies of the QDs are then marked for reference.

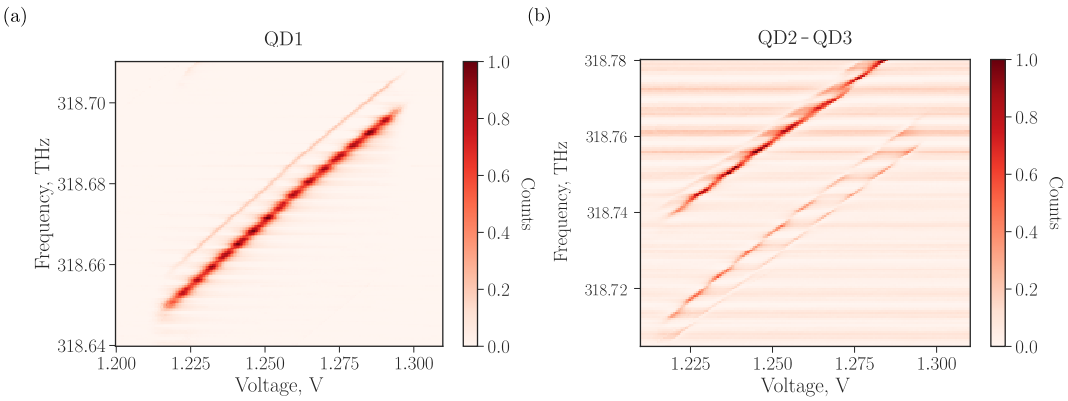

FIGURE 3.7: Resonance fluorescence spectra of (a) QD1, (b) QD2 and QD3 at B_z = 0 T as a function of frequency and bias voltage. As we excite from free space on top of the PCW, (b) implies that QD2 and QD3 are positioned close to each other, within the diameter of the beam spot.

We then perform ABB[9] excitation (Section 2.1.1.1) for each emitter, from free space. As this driving scheme creates the excitation in the bulk material (GaAs), our sample of high density and inhomogeneous broaden ensemble of QDs, can lead to a large number of overlapping spectral lines from the emitters at the vicinity of the beam spot. However, it is chosen as it does not require pre-characterization of the emitters, it can efficiently generate charge carries and the frequency of the laser is far-detuned from the emission of the QDs.

For the ABB drive, the frequency of the laser is locked at ~ 800 nm and the beam spot is translated continuously along the waveguide. When the beam approaches one of the three QDs, the emitter will be excited, and its emission will exhibit a peak on the spectrometer in one of the three marked

[9]We here use the pulsed Tsunami, as it has a larger spectral range

frequencies. With this process, we identified two spots on the waveguide as the locations of the three emitters[10].

With the locations of the QDs now known, we can perform the RF measurements. For that, the CW laser is sent again through the RF path on top of the each of the two identified locations, to excite now the emitters resonantly, with a power of $5\,\mu$W. Similar to the RT charge plateaus above, at each location, the frequency of the laser is scanned with a step of 25 MHz, around the central value for each QD, and for each frequency, the voltage is scanned with a step of 5 mV around the central $V_{bias} = 1.26$ V of the charge plateau. The light emitted is collected from Port 1 and detected by an APD. Figure 3.7 shows the result of the two RF measurements[11].

From these we notice that the RF plateaus show similar characteristics to the RT equivalent. However, Figure 3.7(b) provides a new information. While here only QD2 is intentionally driven for this RF measurement, both QD2 and QD3 plateaus are recorded from the same location. This measurement therefore reveals that the two emitters are not only close spectrally, but also spatially, within the diameter of the diffraction-limited beam spot, $\sim 1\mu$m[12].

3.5 Imaging the quantum dots

A last step in characterizing the emitters, is to estimate their spatial separations. For that, we employ the camera of the setup to image the three QDs inside the PCW. As it will be discussed later, this result could prove useful in confirming the character of the coupling between the crossing QD pairs.

The QDs are imaged from the top of the PCW, by the CMOS camera (DCC CMOS camera, 1280 x 1024 resolution) on the breadboard. To do so, we perform three RT measurements with acquisition time of 30 s. For each of them, the laser is locked on resonance with the imaged QD, at 318.678 THz (QD1), 318.741 THz (QD2) and 318.766 THz (QD3), with $V_{bias} = 1.26$ V, and following with $V_{bias} \approx 1$ V, to subtract the respective backgrounds. The out-of-plane fluorescence of each QD is then recorded on the camera. This imaging method, is essentially exploiting the imperfection of the system, as the photons arriving to the camera are the ones emitted outside of the waveguide, through the leaky mode. The images taken with this procedure are shown in the three bottom plots of Figure 3.8. Finally, to locate the emitters with respect to the waveguide, an image of the PCW with the white-light switched on is acquired and the four images are superimposed (Figure 3.8 top).

The center of each emitter is deducted by fitting the individual images with a Gaussian. For each image, the counts along (x-axis) and vertical (y-axis) to the waveguide are summed up and fitted individually, to obtain the

[10] The same translation of the beam spot for p-shell excitation (laser at ~ 920 nm), giving more clear spectral lines was done to verify the positions.

[11] The 'wavy' features in the background can be owed to different reasons, e.g. poor alignment or laser locking, interferences in the optical setup ect.

[12] From then on, QD2-QD3 were named "Twins", while QD1"Big Sister".

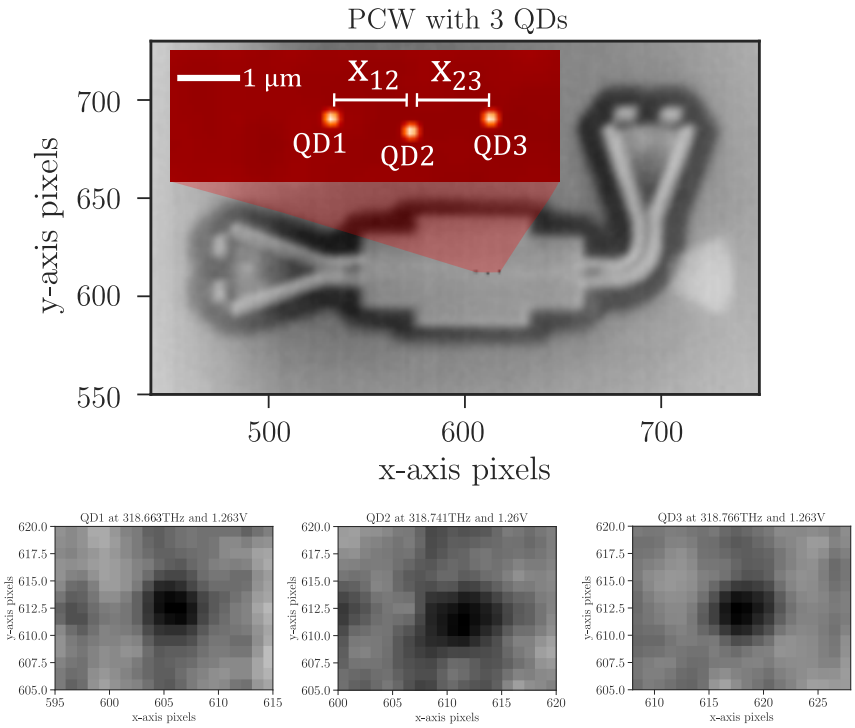

FIGURE 3.8: Fluorescence image of the three emitters inside the PCW. Top: Imaging of the QDs superimposed to a white-light image. Bottom: Individual images of the three emitters.

[x,y] position in pixels for each emitter.

To calculate the separations between each QD pair, the pixels are converted to μm. For that, the dimensions of different features of the nanostructure from the white-light image, are compared to the corresponding features on the mask used to fabricate the chip. The conversion parameter is then found to be $\sim 182 \pm 5$ nm/pixels, resulting into spatial separations of $x_{12} = 970$ nm, $x_{23} = 1252$ nm and $x_{13} = 2222$ nm, along the waveguide. The uncertainty for each x_{mn} is $\sim \pm 184$ nm, including the resolution and the uncertainties of the fits. We therefore note that the precise identification of the spatial separations between the QD pairs is limited by our imaging system, given that the QD size is an order of magnitude smaller than the imaging resolution.

3.6 Parameter summary

Parameters	QD1	QD2	QD3
Central frequency, THz	318.678	318.734	318.762
FSS , GHz	7.05	6.75	4.05
β	0.94	0.83(LF), 0.88(HF)	0.83(LF),0.84(HF)
$\Gamma_m/2\pi$, GHz	2.3	0.69(LF), 0.87(HF)	0.72(LF),0.92(HF)
$\sigma_{sd}/2\pi$, GHz	0.59	0.22	0.6

TABLE 3.1: Summary of the parameters from the characterization of the three emitters in B = 0 T, at $V = 1.26$ V and $P = 1\,\mu$W. The central frequencies shown are of the LF dipole of each emitter.

3.7 Summary and Connection

In the present Chapter we identified and characterized the QDs that will be used throughout the experiments of this thesis. We found three QDs, spectrally close to each other and the band-edge, and well coupled to the mode of their waveguide. Those were the first indications of promising candidates for the investigation of photon-mediated coupled emitters. Frequency-voltage scans showed stable charge plateaus and similar electrical tuning for all three QDs. To bring the detuned emitters to resonance, an out-of-plane magnetic field was identified as the suitable tuning knob. Specifically, by increasing the applied external B_z field, we observed opposite circularly polarized dipoles of the different QDs coming to resonance, pairwise. Finally, from RF measurements we found the physical positions of the emitters inside the waveguide.

In the next Chapter we explore the collective dynamics between the three QD pairs, to observe direct signatures of photon-mediated coupling through the shared waveguide mode, in the modification of their lifetimes.

4 Collective dynamics of two coupled quantum dots

This Chapter is based on the following article

Collective super- and subradiant dynamics between distant optical quantum emitters, A. Tiranov, V. Angelopoulou, C. J. van Diepen, B. Schrinski, O. A. Dall'Alba Sandberg, Y. Wang, L. Midolo, S. Scholz, A. D. Wieck, A. Ludwig, A. Søndberg Sørensen & P. Lodahl, https://www.science.org/doi/10.1126/science.ade9324

In this Chapter we demonstrate experimentally the realization of photon-mediated coupling between different pairs of QD dipoles, embedded, multiple wavelengths apart, in a PCW. We probe the time-resolved dynamics of each pair, for off- and on-resonance conditions between them, and show clear evidence of collective behavior through the super- and subradiant components of the emission. This modification of the decay dynamics is, to the best of our knowledge, the first direct experimental proof of coupling between two QDs. The coherent evolution of the coupling is then investigated through the dynamics obtained by gradual spectral tuning of the crossing dipoles. Finally, we perform a proof-of-principle measurement, to directly drive to a collective state of the coupled system with control, by means of collective excitation.

4.1 Photon-mediated coupling between two optical emitters

In Chapter 3 we characterized three QDs embedded in the same PCW. This system was claimed as promising for probing collective dynamics, as the emitters were found to be: (1) well coupled to the waveguide mode, by the high extinction in the transmission counts, (2) close to the band-edge, which would reduce their radiative lifetime, leaving them less susceptible to noises from the environment, and (3) spectrally close enough to each other to be pairwise tuned to resonance, by a controllable out-of-plane magnetic field, B_z. Benefiting still from the coherent light-matter interface provided by the nanophotonic environment, extending the interaction to multiple optical wavelengths, we use these candidates to observe super- and subradiance from their collective emission.

We begin by recalling the effective Hamiltonian (1.29) describing the dynamics that occur in a dipole-dipole interaction through a waveguide mode,

$$H_{\text{eff}} = \sum_{m,n=1}^{2} \left(J_{mn} - i\frac{\Gamma_{mn}}{2} \right) \sigma_m^+ \sigma_n^- + \sum_{m=1}^{2} \left(\Delta_m - i\frac{\Gamma_m^{loss}}{2} \right) \sigma_m^+ \sigma_m^-,$$

which constitutes the simplified expression of the full master equation (1.23), in the frame rotating with the driving frequency and in the single-excitation subspace. Summarizing briefly the parameters from Section 1.4, Δ_m, is the detuning of QD$_m$ with the driving frequency, such that $\Delta_{mn} = \Delta_m - \Delta_n$ is the relative detuning between QD$_m$ and QD$_n$, Γ_m^{loss} is the rate of photons emitted outside of the waveguide, $\sigma^{\pm}$ are the raising and lowering atomic operators, $J_{mn} = \frac{1}{2}\sqrt{\beta_m \beta_n \Gamma_m \Gamma_n} \sin \phi_{mn}$ is the dispersive coupling rate and $\Gamma_{mn} = \sqrt{\beta_m \beta_n \Gamma_m \Gamma_n} \cos \phi_{mn}$ the dissipative coupling rate. The parameters in the coupling rate expressions are $\Gamma_m = \Gamma_m^{wg} + \Gamma_m^{loss}$ the sum of all decays, in and out of the waveguide, β_m the coupling factor to the waveguide mode for QD$_m$, given by $\beta_m = \Gamma_m^{wg}/\Gamma_m$, and ϕ_{mn} the coupling phase. As introduced before, this is the phase that the electric field accumulates when traveling the distance between the interacting QDs. It relates to their spatial separation x_{mn} by $\phi_{mn} = k|x_{mn}|$, where k is the effective wavenumber of the PCW, and constitutes the defining parameter for the type of the coupling between the emitters.

To experimentally investigate the coupling dynamics of this system, we start with the excitation scheme of driving selectively one emitter from the top of the PCW, as illustrated in Figure 4.1(a). To describe qualitatively the emergence of the depicted dynamics, we make use of the energy diagrams in Figure 4.1(b). Under the single-emitter excitation scheme, when the two QDs are off-resonance with each other, $\Delta_{mn} \neq 0$, (left energy diagram), the photons emitted with a decay rate Γ_m by the driven QD$_m$ are transmitted through the waveguide, either towards Port 1 or Port 2, unaffected by the presence of the second emitter. When the two are brought to resonance, $\Delta_{mn} = 0$, the second emitter will scatter the photons of the first. This photon-mediated interaction, leads to coherent optical dipole coupling between the emitters, and the system is then naturally described by the collective eigenstates (right energy diagram) $|+\rangle = (|e_m g_n\rangle + |g_m e_n\rangle)/\sqrt{2}$ and $|-\rangle = (|e_m g_n\rangle - |g_m e_n\rangle)/\sqrt{2}$, with their decay rates determined by ϕ_{mn}. Specifically, as discussed in Section 1.3, ϕ_{mn} defines the coupling parameters J_{mn} and Γ_{mn} and therefore the type of coupling, ranging between the dispersive, for $\phi_{mn} = (N + 1/2)\pi$, and the dissipative, for $\phi_{mn} = N\pi$, coupling regime.

In the dissipative coupling regime, the two emitters will absorb and re-emit photons in- or out-of-phase with each other, leading to constructive and destructive interference between their fields, respectively. For ideal interference, the constructive case will result into a field with twice the intensity and the decay rate, $\Gamma_+ = 2\Gamma_m$ (assuming $\Gamma_m = \Gamma_n$) of the individual emitter (yellow emission in Figure 4.1). This enhanced emission represents the described phenomenon of superradiance and emerges from the decay of the bright state, $|+\rangle$. If the two fields interfere destructively, there should

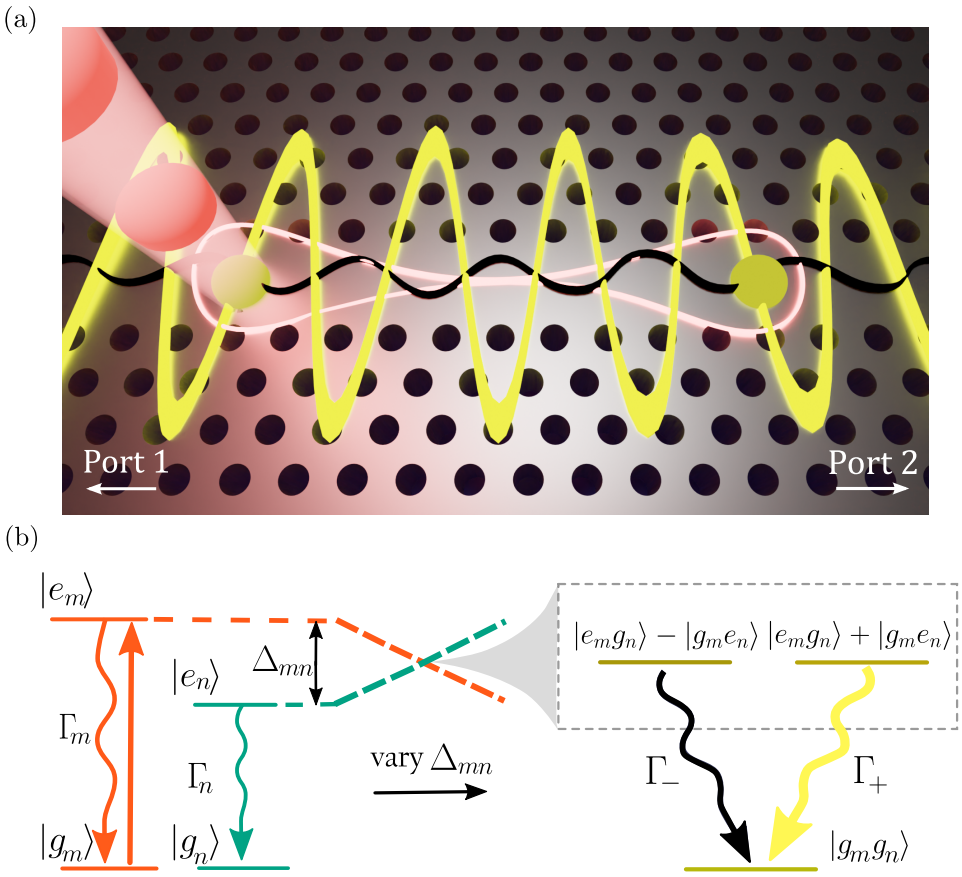

FIGURE 4.1: (a) Illustration showing the modified emission by two coupled (white ∞ line) QDs (yellow hemispheres), embedded in a PCW, when only one emitter is optically driven. The emission dynamics then exhibits super- and subradiace, due to constructive (yellow) and destructive (black) interference of the emitted field scattered by the two QDs. The two arrows at the bottom indicate the direction of the two collection ports. (b) Energy diagrams depicting the transition between the two basis used to describe the two-emitter system. Here, the illustrated dynamics correspond to the case of dissipative coupling between the emitters. For off-resonant QDs (left), detuned by Δ_{mn}, the two decay independently with Γ_m and Γ_n, while when tuned to resonance (right) super- and subradiant dynamics occur with decay rates Γ_+ and Γ_-, respectively.

be no light seen at the collection ports of the waveguide. In other words, the coupled system is a dark state, $|-\rangle$, associated with subradiance, which ideally never decays, $\Gamma_- = 0$ (black emission in Figure 4.1).

There are two pictures to understand subradiance in our system; either one where the photons emitted by the QDs will forever scatter back and forth between them and never exit the system, with the QDs acting as perfect mirrors, or another where the emission happens outside of the waveguide, as the subradiant state is uncoupled from its nanophotonic environment. The latter implies that the ideal subradiant state should be neither excited through the waveguide, nor decaying in it [42]. However, by driving the emitters in RF, from the top of the waveguide, we can populate $|-\rangle$

even deterministically, while imperfections of the system enable the measurement of its emission through the waveguide. Such imperfections could be a residual detuning Δ_{mn}, the presence of pure dephasing γ_{dph}, any small deviation of ϕ_{mn} from the $N\pi$ of the pure dissipative coupling, or uneven decay rates of the individual emitters, that would prevent from the ideal in- and out-of-phase emission [65]. These imperfections facilitate the measurement of the emission from the subradiant state through the waveguide by disrupting the perfect destructive interference. As a result, the long-lived subradiant features diminish quickly, as they are sensitive to decoherences and imperfections [48]. With our system, we exploit the nanophotonic environment and the spectral position of the QDs with respect to its band-edge, to mitigate the effects of γ_{dph}, and employ the magnetic field B_z to finely control Δ_{mn}.

From the above discussion on the effects of the dissipative coupling regime it becomes clear that, with single-emitter excitation, a direct experimental proof of dissipative coupling between two emitters, is to observe a modification in the decay dynamics when the two are tuned off- and on-resonance with each other. Hence, our first objective is to detect this signature in the lifetime measurements of the coupled system.

4.2 Observation of super- and subradiant emission

We begin with calibrating the optical setup for the lifetime measurements, ensuring driving of a single emitter and identifying the suitable excitation scheme. To drive only one emitter of an adjacent pair of QDs[1], we exploit the orthogonal[2] polarization of the crossing dipoles. By driving in RF on top of the QD pair of interest and adjusting the excitation waveplates (Figure 2.5), we can suppress the excitation of the undesired emitter while efficiently driving the other. For the driving, initially, we decided to perform excitation through a higher-energy state (often referred to as p-shell, d-shell.. excitation, see Section 2.1.1.1), to facilitate the filtering of the laser leakage in the waveguide. For that, an initial characterization is required, where the excitation spectra of each QD with a CW laser are recorded on the spectrometer. As an example, the excitation spectra of QD2 is showed in Figure 4.2(a). The spectra show a single photoluminescence line at a fixed wavelength of 940.09 nm (dashed line). The absence of other spectral lines over a large range of the QD emission wavelengths, verifies that only QD2 is excited efficiently under these waveplate conditions. The excitation frequency is then chosen far from resonance to be properly filtered out of the collection, but also close enough such that the relaxation to the s-shell of the conduction band would not affect the lifetime measurement itself. The

[1] that sit $\sim 1\mu$m apart (see Section 3.5), with a diffraction-limited beam spot, arriving on the chip with a diameter of the same order

[2] and circularly polarized orientations, when the magnetic field in Faraday configuration, B_z, is applied

frequency selected for the lifetime measurements of QD2 is around 325.72 THz (laser locked at 920.40 nm).

The investigation of the coupled system with lifetime measurements begins by optically driving, with pulsed excitation, a single QD of a pair in RF. We then record the collective emission dynamics for a continuous range of detunings Δ_{mn} between the emitters around their resonance point, from both ports of the waveguide. This set of measurements are repeated for each of the three QD pairs crossing in Figure 3.5. The pulsed laser employed is a Tsunami laser of 5 ps pulse duration and 80 MHz repetition rate. The laser frequency is fixed to the selected value from the excitation spectra of each QD, depending on the crossing we study, and the power is locked close to the saturation of the driven emitter, as calibrated by power dependence measurements, similar to the one shown in Figure 4.2(b). The emitted intensity in either of the ports is then sent through an optical reflection grating filtering setup (25 GHz bandwidth) and the filtered output is detected either by an SNSPD or a fast APD. We note here that the relative detunings, Δ_{mn} that we scan through, are converted from the values of the magnetic field, B_z, that is the experimentally accessible tuning parameter. The conversion factor is estimated from the fits in Figure 3.5 to be 24.6 GHz/T and the relative $\Delta_{mn}/2\pi = 0$ is defined at the crossing point of the fitted traces for each QD pair.

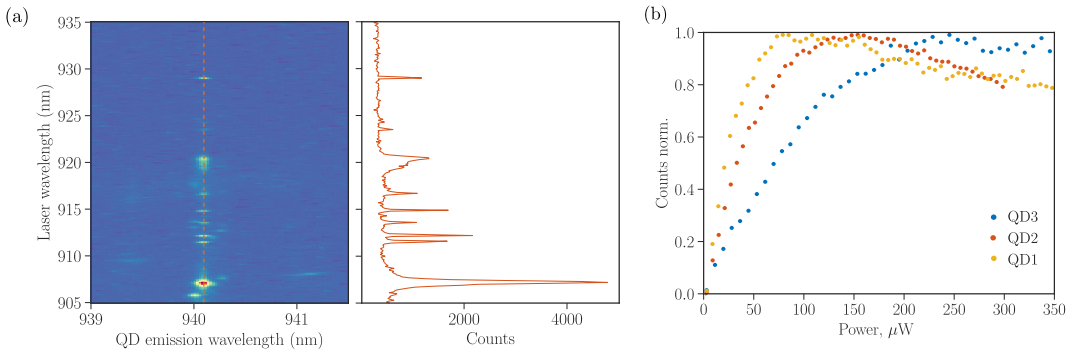

FIGURE 4.2: (a) Excitation spectra of QD2 at 940.09 nm , as a function of excitation wavelength, at zero magnetic field. Higher-energy states appear with increasing laser wavelength. The photoluminescence excitation spectra recorded at the emission wavelength (dashed line) is shown on the left side. (b) Power saturation measurement for the three QDs, with pulsed excitation through higher-energy state.

The lifetime measurements recorded for the crossing of QD1-QD2 while driving QD2, and QD2-QD3 while driving QD3 are shown in Figure 4.3(a) and (b), respectively, in logarithmic scale. Here, two time traces of the complete scan of Δ_{mn}, included in Appendix B, collected from Port 1 are plotted for the two pairs. The traces shown are for the emitters off-[3] and on-resonance with each other. In each time trace the counts are normalized to the maximum at zero-time delay, corresponding to the time of excitation of the coupled system.

[3] At $\Delta_{12}/2\pi$ = 6 GHz and $\Delta_{23}/2\pi$ = 5 GHz.

From the plots we observe that, in the case where the two emitters are off-resonant (red), the expected monotonic exponential decay from the single-emitter driving[4] is recorded. Interestingly, when the emitters are brought to resonance (yellow-black), the decay behavior shows evident modification. Instead, the emission follows a bi-exponential decay, with a fast component (yellow) at short times and a slow component (black) persisting after the single emitter has fully decayed to its ground state. The fast decay with rate Γ_+, is attributed to the emission from the superradiant state, $|+\rangle$, while the slow decay, Γ_-, results from the depopulation of the subradiant state, $|-\rangle$. We here emphasize that it is exactly these modifications of the decay dynamics from the resonant emitters that we were after. This observation constitutes a direct signature of coherent coupling between the QD pairs.

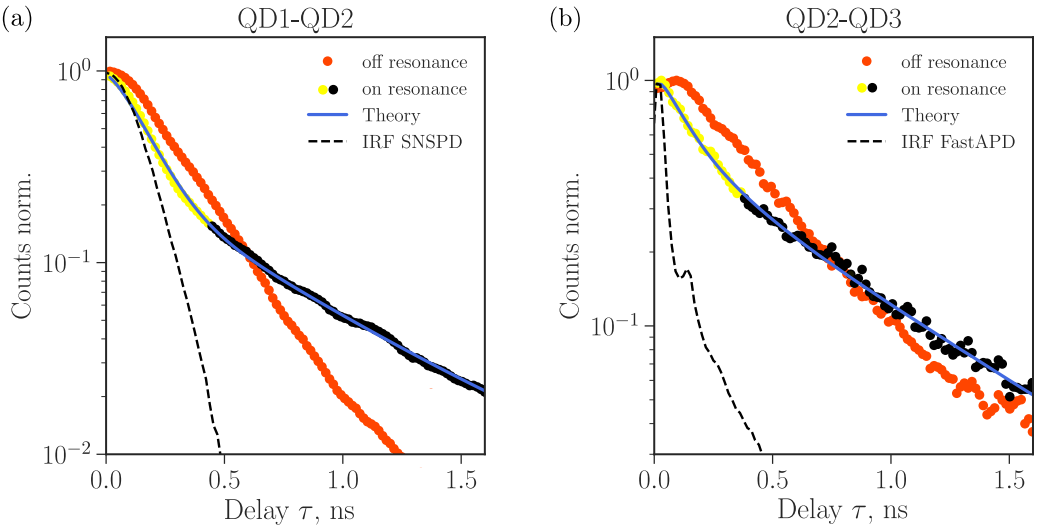

FIGURE 4.3: Time-resolved decay dynamics in logarithmic scale, as recorded in the experiment for the pairs (a) QD1-QD2 and (b) QD2-QD3, for off- and on-resonance conditions. For the on-resonance trace, two colors are used to highlight the bi-exponential trend, where the fast Γ_+ (yellow) and slow Γ_- (black) components of the decay, correspond to super- and subradiant dynamics. The counts are normalized to the maximum at $\tau = 0$. The blue solid line is a fit to the experimental data, by a bi-exponential convolved with the instrument response function (IRF) of the corresponding detector.

The decay rates of the two collective states are deducted by fitting (blue line) the on-resonance experimental data with a bi-exponential function. This is convolved with the instrument response function (IRF, black dashed lines) of the single-photon detectors, which limits the modeling at short times. For the QD1-QD2 pair, an SNSPD with 200 ps FWHM temporal jitter is used, whereas for QD2-QD3 the detection is done by a fast APD with 40 ps FWHM temporal jitter. By fitting the intensities of QD1-QD2, the modified radiative linewidths from the coupling are found to be $\Gamma_+/2\pi = 1.36 \pm 0.08$

[4]Either QD2 or QD3 in (a) and (b), respectively.

GHz and $\Gamma_-/2\pi = 0.28 \pm 0.02$ GHz[5]. Those should be considered in comparison to the linewidths of the individual emitters, obtained at off-resonance conditions for this pair, $\Gamma_1/2\pi = 0.85 \pm 0.01$ GHz and $\Gamma_2/2\pi = 0.79 \pm 0.02$ GHz, which are approximately in between the two modified values.

Deriving the ratio of the super- over the subradiant decay rate for QD1-QD2 we find Γ_+/Γ_- = 4.8. This enhancement factor constitutes a direct figure of merit of the coupling strength between the two emitters. Increasing the ratio further would demand careful considerations over the system and the excitation scheme, as the coupling strength is sensitive to the experimental decoherences and imperfections listed in Section 4.1, as well as to the duration of the excitation pulse, which needs to be calibrated for the examined QD pair. Potential optimization steps to increase the coupling strength are discussed in more detail in the Outlook.

Another parameter that would limit the dipole-dipole coupling strength and the scaling up of the inter-emitter separation, x_{mn}, are the losses of photons that mediate the interaction [106]. In free space, x_{mn} needs to be smaller than the optical wavelength, such that the coupling strength would be larger than the coherence decay rate. In our system, we observe that the nanophotonic structure, as a coherent light-matter interface, extends this dipole-dipole coupling to multiple wavelengths. To demonstrate this we imaged the QDs inside the PCW, to estimate the spatial separations between the crossing pairs (see Section 3.5). By comparison to the optical wavelength inside GaAs, $\lambda = 270$ nm[6], we confirm the above claim as $x_{12} \approx 3.6\lambda$ and $x_{23} \approx 4.6\lambda$. An upper bound to the x_{mn}, is imposed by the photon losses inherent to the nanostructure[7], which restrict the spatial separation of the coupled emitters to $\sim 20\,\mu$m ($\sim 70\lambda$) in the slow light region of the PCW, where the QDs are well-coupled to the waveguide mode [47].

Finally, to extract a consistent set of the coupling parameters, we use the complete experimental dataset recorded for all three QD pairs in both collection ports (in Appendix B). For each pair and port, five time-traces of different detunings $\Delta_{mn}/2\pi$ around $\Delta_{mn}/2\pi = 0$ are fitted with the theoretical model described in Section 1.4. Specifically, the analytical expressions for the output fields are used to calculate the intensity at the two ports as $I_{R,L} = |E_{R,L}|^2$, with R and L standing for right (Port 2) and left (Port 1) side of the waveguide. For a simplified form of the output fields, an instantaneous π-pulse excitation, compared to the emitters' lifetimes $1/\Gamma_m$, $1/\Gamma_n$, and zero dephasing are assumed. The expressions for the fields arriving at the left and the right detector then read (from Supplemental Material of [56]),

$$E^{R,L} = E_+^{R,L} + E_-^{R,L}, \tag{4.1}$$

[5]The complete set of radiative decays found from the fits are included in Table 4.1 together with all modeled experimental parameters.

[6]To be transparent, from a different approach, since the QDs are close to the band-edge, the relation $k\alpha/2\pi = 0.5$ holds, where k is the wavevector and α the lattice constant of the PCW. This results in a $\lambda = 2\alpha = 480$ nm. To find an accurate relation between x_{mn} and λ, one would need to solve the Greens function in the PCW.

[7]7 dB/mm, attributed to scattering losses due to the sidewall roughness [85]

where $+$ and $-$ correspond to super- $|+\rangle$ and subradiant $|-\rangle$ emission with,

$$E_{+}^{R} = \frac{-i\sqrt{\Gamma_m\beta_m}(\Gamma_n\beta_n - i\Delta_{mn} + (S+\Gamma_m-\Gamma_n)/2)}{\sqrt{2}S}\exp\left[-(\Gamma_m+\Gamma_n+S)\frac{t}{4})\right]$$
$$E_{-}^{R} = \frac{i\sqrt{\Gamma_m\beta_m}(\Gamma_n\beta_n - i\Delta_{mn} + (-S+\Gamma_m-\Gamma_n)/2)}{\sqrt{2}S}\exp\left[-(\Gamma_m+\Gamma_n-S)\frac{t}{4})\right], \tag{4.2}$$

and

$$E_{+}^{L} = \frac{-i\sqrt{\Gamma_m\beta_m}(e^{2i\phi_{mn}}\Gamma_n\beta_n - i\Delta_{mn} + (S+\Gamma_m-\Gamma_n)/2)}{\sqrt{2}S}\exp\left[-(\Gamma_m+\Gamma_n+S)\frac{t}{4})\right]$$
$$E_{-}^{L} = \frac{i\sqrt{\Gamma_m\beta_m}(e^{2i\phi_{mn}}\Gamma_n\beta_n - i\Delta_{mn} + (-S+\Gamma_m-\Gamma_n)/2)}{\sqrt{2}S}\exp\left[-(\Gamma_m+\Gamma_n-S)\frac{t}{4})\right], \tag{4.3}$$

where $S = \sqrt{4e^{2i\phi_{mn}}\Gamma_m\Gamma_n\beta_m\beta_n + (2i\Delta_{mn}-\Gamma_m+\Gamma_n)^2}$. For the fitting, a conservative value of $\sqrt{\beta_m\beta_n} = 0.8$ is used to extract a lower bound to the coupling parameters of the QD pairs. The total intensity $I_{R,L}$ found, is then integrated over the spectral linewidth for detunings Δ_{mn} between each pair of QDs, to account for spectral diffusion. The result is finally convolved with the IRF of the detectors. In particular, of the SNSPD for the QD1-QD2 pair and the fast APD IRF for QD2-QD3 and QD1-QD3, with their respective temporal jitters (see Section 2.6). The extracted coupling parameters, $\phi_{mn}, \Gamma_{mn}/2\pi$ and $J_{mn}/2\pi$ for all three pairs, are summarized in Table 4.1. These parameters are then used to model the experimental data through numerical integration of (1.23). The result is averaged over a normal distribution of detunings Δ_m around the resonant transition of the driven QD$_m$, with standard deviation σ_{sd}, to include the effects of spectral diffusion. The theoretical modeling for all pairs and both ports are presented in the theory figures of Appendix B and exhibit good agreement with the experimental data.

4.3 Coherent evolution of the coupled system

To explore further the dynamics of the system, we repeat the previous set of measurements driving now the emitters resonantly, and investigate the coherent evolution of the collective states.

Continuing with the single-emitter excitation in RF, we proceed to drive the QD3 dipole of QD2-QD3 and record the time-evolution of the collective dynamics, as a function of $\Delta_{23}/2\pi$. Here, the pulsed laser is tuned in resonance with the transition of QD3 at about 318.76 THz, and is power-stabilized with an AOM. The power used is calibrated by performing Rabi oscillation measurements prior to each lifetime measurement, to apply the optical power corresponding to a π-pulse for the driven QD. An indicative Rabi measurement for QD2-QD3 pair is shown in Figure 4.4, where in (a)

only QD3 is excited, by alignment and polarization selectivity, while the anticipated emission from QD2 at around 1.275 V, as seen in (b), is not present. The power selected for QD3 from (a) is about 4 μW. The emission is collected again from both ports of the waveguide, and prior to detection, is subjected to filtering, by a transmission grating and a temperature-controlled etalon filter, with narrow linewidth of 3 GHz, to suppress the laser background. The detector used here is an SNSPD.

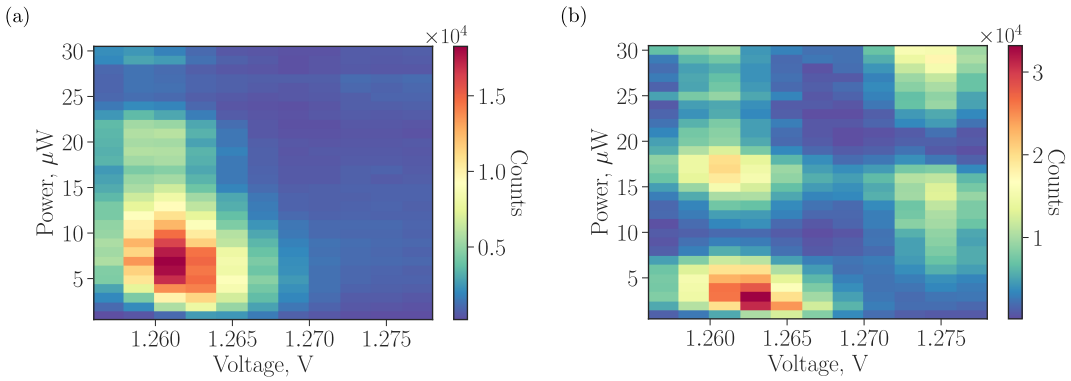

FIGURE 4.4: Rabi oscillations from (a) QD3 and (b) both QD3 and QD2 after rotating the polarization of the excitation laser. (b) QD2 dipole is resonant with the filtering etalon for a voltage of about 1.275 V. Two maxima appear implying that both dipoles are excited for different excitation powers. The calibration is done at a magnetic field where the two dipoles are far from resonance, at 0.8 T, and the pulsed laser is locked at around 940.5 nm.

The results of these measurements are shown in Figure 4.5(a) and (b) for Ports 1 and 2, respectively, where the counts in each time-trace have been normalized to the sum of the counts for that $\Delta_{23}/2\pi$. These 2D maps are essentially a collection of single time-traces, similar to the ones shown in Figure 4.3(b), for a range of $\Delta_{23}/2\pi$ around the crossing point of the QD2-QD3 dipoles. We visualize this correspondence by indicating the two time-traces of Figure 4.3(b) with dashed color-coded lines on Figure 4.5(a).

With the excitation of QD3, the system is prepared in an equal superposition of the two collective states, $|g_2e_3\rangle = (|+\rangle + |-\rangle)/\sqrt{2}$. To explain the emerging features in Figure 4.5(a) and (b), as the system evolves with time from the initial state $|g_2e_3\rangle$, we refer back to the effective Hamiltonian, H_{eff}, in (1.29). Assuming that the two emitters have the same decay rates $\Gamma_2 = \Gamma_3 = \Gamma$ and coupling efficiencies $\beta_2 = \beta_3 = \beta$, we deduct a simplified form of the two eigenvalues of the coupled system, $E_\pm = \frac{1}{2}\left(-i\Gamma + \Delta_2 + \Delta_3 \pm \sqrt{\Delta_{23}^2 + (2J_{23} - i\Gamma_{23})^2}\right)$ [107] and claim that the correlated dynamics would then evolve according to the difference between them,

$$f_{osc} = \sqrt{\Delta_{23}^2 + (2J_{23} - i\Gamma_{23})^2}. \tag{4.4}$$

Considering pure dissipative coupling ($J_{23} = 0$), from the above relation two co-existing effects that dictate the dynamics are identified:

- The coherent evolution due to Δ_{23}, which, in a simplified picture, can be translated to an acquired phase in time between the excitation of the two emitters, $|e_2 g_3\rangle + e^{i\Delta_{23}t}|g_2 e_3\rangle$. This would induce interchange of population between $|+\rangle$ and $|-\rangle$, as illustrated in Figure 4.6(a) with red arrows.

- The dissipation itself Γ_{23}, that defines the decay rates of the collective states, $\Gamma_{\pm} = \Gamma \pm \Gamma_{23}$ (for $\Delta_{23} = 0$) [57], bringing the population to the collective ground state, $|g_2 g_3\rangle$.

More specifically, for a short pulse duration and a repetition rate larger than the longer decay time of the coupled system ($1/\Gamma_{-}$), such that we ensure that we are in the single-excitation subspace, the equation (4.4) indicates three regimes:

> $|\Delta_{23}| > \Gamma_{23}$, the under-damped regime, where the coherent evolution dominates the dissipation. There, as soon as the state evolves out of the perfect superpositon, $|g_2 e_3\rangle$, (since the population in $|+\rangle$ starts to decay fast after excitation) Δ_{23} will induce exchange of population between $|+\rangle$ and $|-\rangle$ states, leading to coherent oscillations of the intensity. The dashed white lines in Figure 4.5, trace the intensity maxima for the different Δ_{23}, corresponding to the maximal population of $|+\rangle$. This occurs at times $t = \pi/f_{osc}$ for each Δ_{23}. The intensity oscillations are gradually damped in time, as the system simultaneously decays to $|g_2 g_3\rangle$.
>
> $|\Delta_{23}| = \Gamma_{23}$, the critical damping regime, where the dissipation and the coherent oscillations impact the evolution equally. This results into the long "fins" appearing symmetrically around $\Delta_{23}/2\pi = 0$.
>
> $|\Delta_{23}| < \Gamma_{23}$, the over-damped regime, where the dissipative coupling damps the excitation fast to $|g_2 g_3\rangle$, before any coherent oscillation occurs, giving rise to the gap of $2\Gamma_{23}$ between the white dashed lines. In the resonant case specifically, $\Delta_{23}/2\pi = 0$, the coherent evolution exhibits no oscillations. The population in $|+\rangle$ will decay fast after excitation, and the remaining population in $|-\rangle$ will decay at longer times, directly to $|g_2 g_3\rangle$.

To visualize the dynamics that occur in the coupled system through time, we simulate the evolution of the quantum state for a large detuning between the emitters, $\Delta_{23} = -5.5\Gamma$ on the Bloch sphere, in Figure 4.6(b). This Bloch sphere represents the single-excitation subspace of the coupled system. In sequential colors, the length of the Bloch vector indicates the population of the collective state at each time; from the moment of excitation, to the complete decay down to the collective ground state $|g_2 g_3\rangle$, at the origin of the sphere. Following the colormap of time, the population starts from $|g_2 g_3\rangle$. When QD3 is excited with a π-pulse, the population is transferred to $|g_2 e_3\rangle$ at the equator. For the case of large Δ_{23} between the emitters as depicted

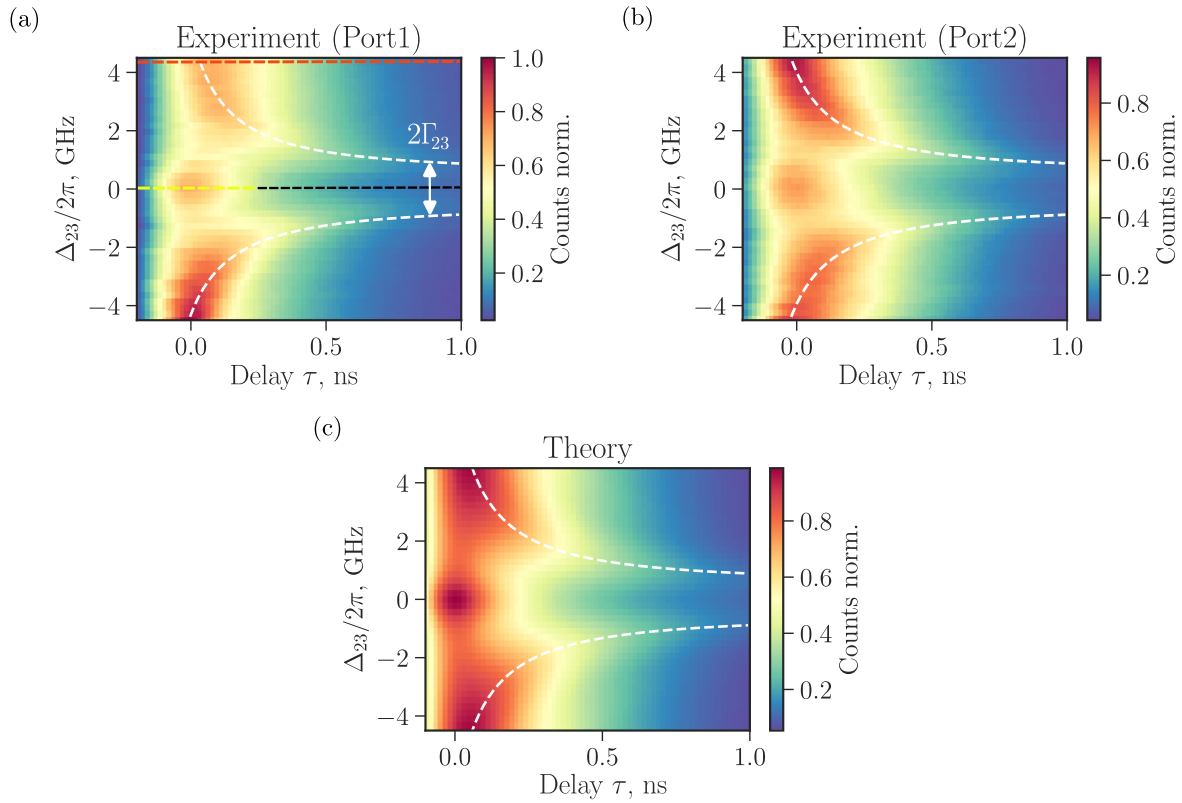

FIGURE 4.5: (a) and (b) Complete set of experimental data of the time-resolved intensity of the collective emission from QD2-QD3, as a function of $\Delta_{23}/2\pi$ when driving QD3. The collection is recorded from Port 1 and 2, respectively. The data of each trace are normalized to the sum of the counts in each $\Delta_{23}/2\pi$. The horizontal dashed lines in (a) are color-coded to correspond to the traces shown in Figure 4.3(b), while the white dashed lines trace the maximum of the intensity for all $\Delta_{23}/2\pi$. (c) Modeling the experimental data with the theory, using the experimental parameters of QD2-QD3 pair (Table 4.1).

here, as soon as the system begins to decay, it will no longer be in an eigenstate of the coupled system. Δ_{23} then induces coherent oscillations between the super- (north pole) and the subradiant (south pole) states, at a frequency defined by the Δ_{23}[8]. Since the coupled system dissipates at the same time, these coherent oscillations appear as a spiral with decreasing amplitude, while the system decays to $|g_2 g_3\rangle$, back to the center of the Bloch sphere. The handedness of the state's evolution is determined by the orientation of the quantization axis. That is the resultant of Δ_{mn} (gray solid arrow) and J_{mn} (gray dashed arrow), represented as vectors on the Bloch sphere. As we are restricting ourselves to the dissipative limit, where $J_{mn} = 0$, the state then revolves around the axis defined by Δ_{mn}, as shown in Figure 4.6(b). Specifically, for $\Delta_{23} < 0$, where $\Delta_{23} = \Delta_2 - \Delta_3$, the state evolves anti-clockwise, whereas for $\Delta_{23} > 0$ clockwise.

By comparing the intensities from the two collection ports in Figure

[8]since Γ_{23} is fixed for a specific pair, as it is defined by the $|x_{23}|$.

4.5(a) and (b), we see similar behavior, implying a predominately dissipative character for the coupling of the emitters. To elaborate, the intensities from the two sides of the waveguide can be expressed by,

$$I_L = \sum_{m,n=2}^{3} E_m^* E_n e^{-i\phi_{mn}}$$
$$I_R = \sum_{m,n=2}^{3} E_m^* E_n e^{i\phi_{mn}}, \tag{4.5}$$

where $E_m = -i\frac{\sqrt{\beta_m \Gamma_m}\sigma_m^-}{\sqrt{2}}$, is the amplitude of the field in the waveguide. The two almost identical results in Figure 4.5(a) and (b), reveal that $I_L \approx I_R \Rightarrow \phi_{23} \approx N\pi$, since only then $e^{-i\phi_{23}} = e^{i\phi_{23}} = (-1)^N$, resulting in an equal signal at both detectors. As explained in Section 1.3, $\phi_{23} = N\pi$ would maximize the dissipative coupling rate Γ_{mn}, leading to maximally modified decay rates of the coupled system, $\Gamma_\pm$. This determines the nature of the coupling as predominantly dissipative[9].

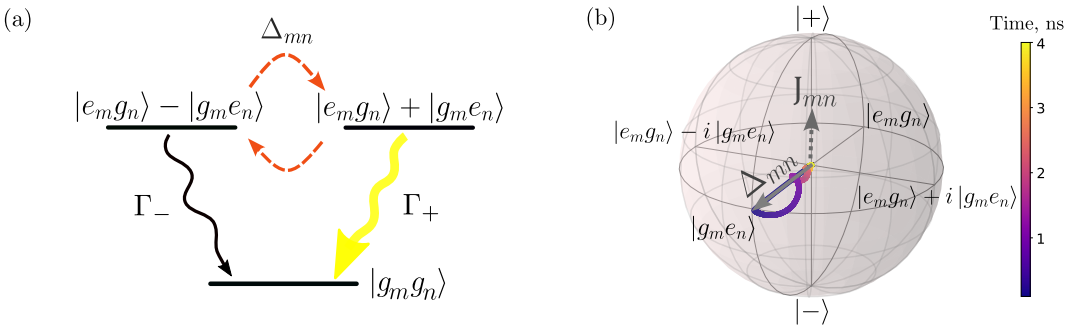

FIGURE 4.6: (a) Energy diagram of the collective states relevant for the single-emitter excitation scheme. Detuning Δ_{mn} between the emitters allows for coherent exchange of population, between the super- and the sub-radiant states. (b) Bloch sphere of the single-excitation subspace of the coupled system with the state evolution trajectory for $\Delta_{23} = -5.5\Gamma$.

Comparing Figure 4.5(a) and (b) with the corresponding complete scans done through higher-order QD shell excitation, "off-resonantly", for QD2-QD3 (Figure B1), we observe an equivalent behavior in the results. The only discrepancy appears at short times after the excitation, where the resonant driving exhibits higher-resolution to the dynamics features. That can be explained by the nature of the decay process for the "off-resonant" driving, that takes short, but finite, time for the electron to relax to the s shell of the conduction band before the decay (see Section 2.1.1.1). This relaxation process has not a well-defined time-duration, resulting in washing-out the effects of the dynamics for short times after excitation.

We note that by comparing the experimental results acquired by excitation through a higher-energy state (Appendix B) we find similar signal

[9]Further discussion is provided in the Supplementary Material of [56]

recorded in both ports, for all three QD pairs, suggesting predominately dissipative coupling between all studied QDs. Indeed, the experimentally extracted coupling rates Γ_{mn} and J_{mn} in Table 4.1 are very similar for all three QD pairs and result to a coupling phase $\phi_{mn} = 0.05 - 0.08\pi$, approximating at the limit of pure dissipative coupling ($\phi_{mn} = N\pi$). The explanation behind this phenomenologically suspicious coincidence, lies in the selection method of the QD candidates. As discussed in Section 3.1, the three QDs, investigated in this Chapter, were pre-selected for their high extinction in the RT measurement, implying good coupling to the PCW mode, i.e., high β-factors. This condition, leads to the selection of QDs that are at well-defined positions in a unit cell of the PCW, as the β-factor has strong spatial dependence [90]. Therefore, the spatial separation x_{mn} of adjacent pairs is determined by the periodicity of the photonic crystal lattice, as $x_{mn} \approx N\alpha$, where α the lattice constant and N an integer number. Since the QDs are also spectrally close to the band-edge of the PCW, the wavevector is given by $k_x\alpha/2\pi \approx 0.5 \Rightarrow k_x\alpha \approx \pi$ [47]. Consequently, for QD pairs with high β-factors and spectrally close to the band-edge of the PCW, their spatial separation leads to an accumulated phase of $\phi_{mn} = k_x|x_{mn}| \approx N\pi$. As a result, the coupling is predominantly of dissipative character for all three QD pairs, due to their selection requirements.

The experimental results in Figure 4.5(a) and (b) are further simulated with the theoretical model developed for the coupled QDs in the waveguide. Specifically, we follow the procedure described for the theory figures in Appendix B and use the experimentally extracted parameters of QD2-QD3 in Table 4.1. The resulting theoretical calculation is depicted in Figure 4.5(c) and shows good agreement with the experimental data. The theory figures of both ports are included in Appendix C.

The dissipative and dispersive coupling rates included in Table 4.1 from the analysis of the data discussed in Section 4.2, are calculated by their definitions, $\Gamma_{23} = \sqrt{\beta_2\beta_3\Gamma_2\Gamma_3}\cos\phi_{23}$ and $J_{23} = \frac{1}{2}\sqrt{\beta_2\beta_3\Gamma_2\Gamma_3}\sin\phi_{23}$ using the fitted $\{\Gamma_2, \Gamma_3\}/2\pi$ and ϕ_{23}. They are found to be $\Gamma_{23}/2\pi = 0.61$ GHz and $J_{23}/2\pi = 0.03$ GHz, respectively. The negligible dispersive component of the coupling, allows to approximate the relations of the super- and subradiant decay rates. Given by $\Gamma_\pm = -2\,\mathrm{Im}\,(E_\pm)$, where $E_\pm$ the simplified eigenvalues of the H_{eff} introduced earlier, the result to the lowest order, where the decay rates scale quadratically, reads

$$\begin{aligned} \Gamma_+ &\approx \Gamma + \Gamma_{23} - \frac{\sigma_{sd}^2}{2\beta\Gamma} \\ \Gamma_- &\approx \Gamma - \Gamma_{23} + \frac{\sigma_{sd}^2}{2\beta\Gamma}, \end{aligned} \tag{4.6}$$

assuming once more $\Gamma_2 = \Gamma_3 = \Gamma$, while σ_{sd} substituted the detuning Δ_{23} in the eigenvalues $E_\pm$, considering the two QDs in resonance with each other, $\Delta_{23} = 0$. The modified linewidths due to the coupling are then calculated

to be $\Gamma_+/2\pi$ = 1.25 GHz and $\Gamma_-/2\pi$ = 0.27 GHz, using the QD2-QD3 parameters from Table 4.1[10]. The modeled values seem to approximate well enough the experimentally estimated $\Gamma_+/2\pi$ = 1.33 GHz and $\Gamma_-/2\pi$ = 0.22 GHz, extracted by fitting the resonance data curve in Figure 4.3(b) with the empirical convolved function. The same analysis is applied to the other two crossings of QD1-QD2 and QD1-QD3 dipoles, completing Table 4.1.

4.4 Proof-of-principle controlled preparation of the collective state

Having pinned down the coupling, we aim now to find an excitation scheme that would give control over the preparation of the initial collective state. Dominating the deterministic population of the super- or the sub-radiant state, would pave the way for their use in quantum-information processing [26, 34, 39, 108].

In order to initialize the system to a desired collective state, both QDs of the crossing pair have to be coherently excited, with driving fields Ω_m and $\Omega_n e^{i\theta}$, where Ω_m and Ω_n are the driving field areas and θ the relative driving phase. These three are the parameters that would determine the initial state of the coupled system. For equal driving pulse areas, $\Omega_m = \Omega_n$, corresponding to a $\pi/2$ Rabi flip on each QD dipole, the prepared state is given by $(|g_m\rangle + |e_m\rangle) \otimes (|g_n\rangle + e^{i\theta}|e_n\rangle)$. This implies a population of 50% in the single-excitation subspace $|e_m g_n\rangle + e^{i\theta}|g_m e_n\rangle$, and 25% for each of the $|g_m g_n\rangle$ and $|e_m e_n\rangle$. By then having control over the relative driving phase θ, we can populate the desired collective state on demand, where $\theta = 0$ would drive the system[11] to $|+\rangle$ state and $\theta = \pi$ to $|-\rangle$.

To implement this driving experimentally with our setup, we exploit their spatial proximity and orthogonal polarizations. As the coupled QDs are in close proximity, the double excitation can be applied by a single driving beam, circumventing the requirement for phase stabilization in the case where two individual excitation beams would be needed. As already discussed in Section 3.3, with the magnetic field applied in Faraday configuration, B_z, the Zeeman splitting leads to the crossing of both orthogonally and circularly polarized dipoles, $\sigma_\pm$, of the two QDs[12]. This suggests that by controlling the polarization of the excitation laser, we can effectively determine the relative driving phase θ between the two dipoles.

As the latter argument might not be directly intuitive, we recall the definition of the Rabi frequency from the semi-classical description of light-matter interaction $\Omega_n e^{i\theta_n} = -\frac{E_{0,n}}{\hbar}\langle g_n|\,\vec{\epsilon}_n \cdot \vec{d}_n\,|e_n\rangle$, where $\vec{\epsilon}_n$ is the polarization and $E_{0,n}$ the amplitude of the driving laser field. From here we see that the same polarization of the excitation laser, can induce different Rabi frequencies Ω_n and driving phases θ_n, depending on the dipole $\vec{d}_n$ it addresses. In

[10] $\beta_2 = \beta_3 = 0.8$ and $\Gamma = (\Gamma_2 + \Gamma_3)/2$.
[11] by 50%
[12] Yet, they are efficiently coupled through the optical mode of the PCW.

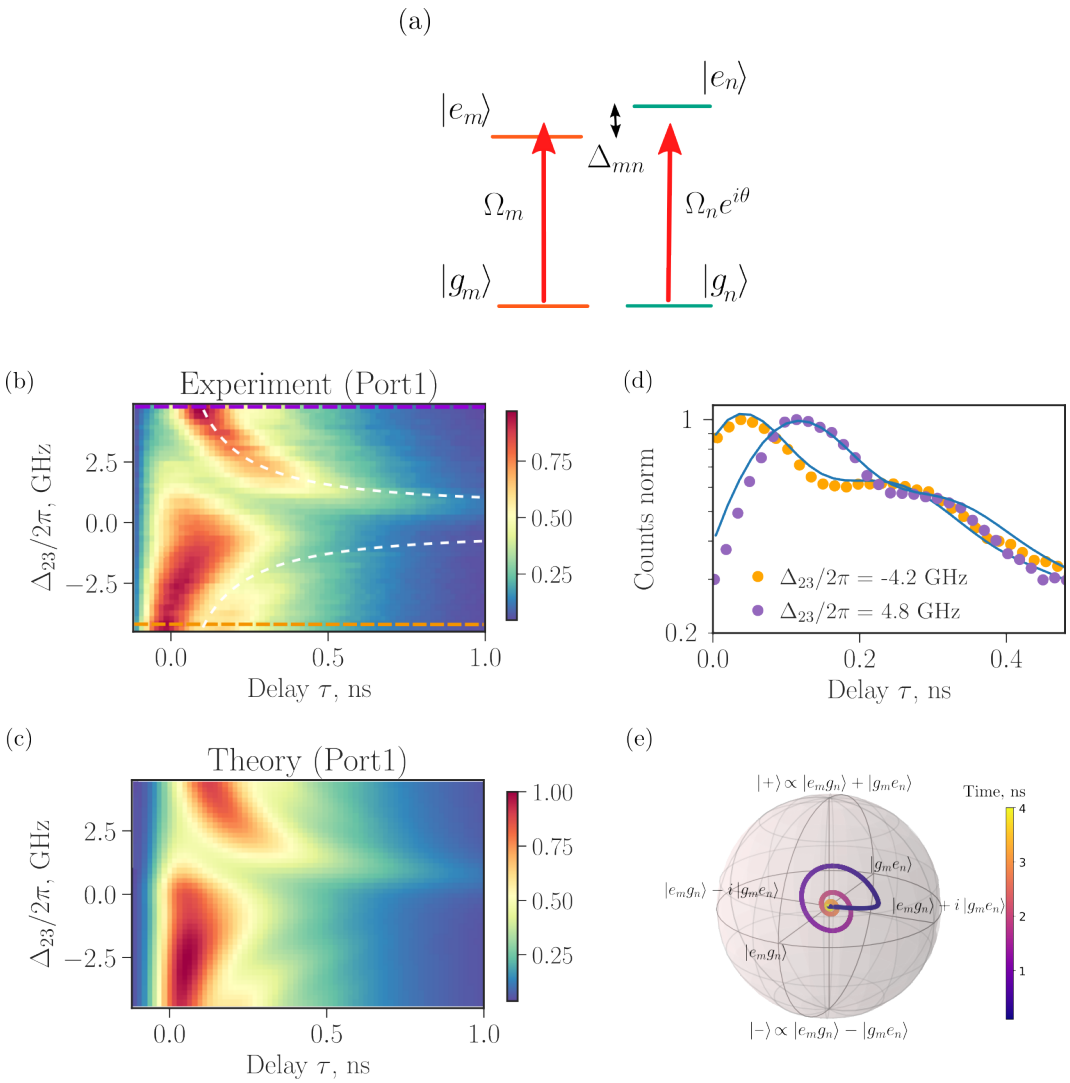

FIGURE 4.7: (a) Excitation scheme driving both QDs at the same time, with a phase difference θ. Controlling θ allows to initialize the system in a collective state. (b) Measured time-resolved intensity of the emission as a function of detunings $\Delta_{23}/2\pi$ and (c) the theoretical equivalent, calculated for the experimental parameters of the pair QD2-QD3 and a $\theta \approx -\pi/2$. (d) Two traces of the lifetimes measured at symmetrical $\Delta_{23}/2\pi$ around zero, showing out-of-phase coherent oscillations of their intensities. (e) Bloch sphere showing the evolution of the quantum state with time from the initially prepared $|e_2 g_3\rangle + i\,|g_2 e_3\rangle$ towards $|+\rangle$ for a negative detuning, $\Delta_{23}/2\pi < 0$, between the emitters.

other words, the relative driving phase $\theta = \theta_m - \theta_n$, is determined by the local polarization projection of the driving field on the two crossing dipoles.

Making use of this information, we return to excite resonantly the QD2-QD3 pair. The same calibration procedure described for the single-emitter excitation in Section 4.3 is followed, but now the polarization of the excitation beam is adjusted to drive both dipoles simultaneously (Rabi oscillations observed similar to Figure 4.4(b)). This results in the driving scheme illustrated in Figure 4.7(a) for off-resonant QD dipoles. We then conducted

lifetime measurements across a range of $\Delta_{23}/2\pi$ centered around the resonance point of the pair, by sweeping again B_z. Figure 4.7(b), shows the intensities of the collective emission from Port 1, normalized over the sum of the counts in each respective time-trace, as collected after the etalon filter and detected by an SNSPD.

From this plot it becomes apparent that, unlike the single-emitter excitation case, the data from driving both QDs exhibit large asymmetry around $\Delta_{23}/2\pi = 0$. Close to zero time delay, $\tau = 0$, for $\Delta_{23}/2\pi < 0$, the emission from the coupled system results in high counts, whereas for a symmetric $\Delta_{23}/2\pi > 0$ the counts appear to be low. This asymmetry continues through time, leading to out-of-phase coherent oscillations of the intensity. To show this more clearly, two time-traces from the experimental data, at almost symmetric detunings around zero, are shown in Figure 4.7(d). The overall asymmetric behavior becomes also apparent when following the white dashed lines in Figure 4.7(b). Even though symmetric around zero $\Delta_{23}/2\pi$, they trace the first minima of the intensities for $\Delta_{23}/2\pi < 0$, and the first maxima for $\Delta_{23}/2\pi > 0$.

To find the driving parameters Ω_2, Ω_3 and θ, we employ the full master equation (1.23) and model the experimental data using the parameters in Table 4.1 for the QD2-QD3 pair. The theoretical calculation, shown in Figure 4.7(c), appears to reproduce well the coherent behavior observed experimentally, for Rabi frequencies $\Omega_2/2\pi = 0.87 \pm 0.06$ GHz, $\Omega_3/2\pi = 1.33 \pm 0.05$ GHz and a relative driving phase $\theta = -(0.48 \pm 0.02)\pi$.

Given the driving parameters, we can now explain the coherent dynamics rising with time in Figure 4.7(b), using the Bloch sphere introduced previously. With the above found parameters, the driving initially populates in-part a state close to $|e_2 g_3\rangle + i\,|g_2 e_3\rangle$[13] as shown in Figure 4.7(e), where the time evolution of the quantum state is traced in Bloch sphere, for $\Delta_{23}/2\pi < 0$. Upon excitation, the system starts to evolve towards the $|+\rangle$ state. The $|+\rangle$ state decays in-part fast, giving the high counts in intensity at short time delays in Figure 4.7(b) for $\Delta_{23}/2\pi < 0$. At the same time, the rest of the population in $|+\rangle$ is transferred to $|-\rangle$, due to the presence of large Δ_{23} between the two emitters. As a result, the intensity counts subsequently drop, since $|-\rangle$ effectively delays the emission. This coherent exchange between the two collective states continues, while the system decays to $|g_2 g_3\rangle$, at the origin of the Bloch sphere. The observed oscillations in the intensity, are therefore again attributed to the exchange of population between $|+\rangle$ and $|-\rangle$, induced by Δ_{23}. Those are here more pronounced than in the single-emitter excitation case, since the system is directly initialized in a state that is not an eigenstate, and thus starts to coherently evolve immediately after its excitation.

For the case where $\Delta_{23}/2\pi > 0$, the reverse behavior is observed. The evolution in the Bloch sphere would be equivalent to the one shown in Figure 4.7(e), but with the time-trace revolving now clockwise, populating first $|-\rangle$ state. That can be understood again in terms of the quantization axis, which would flip its orientation depending in the sign of Δ_{23}.

[13] As mentioned the remaining population is shared between $|g_2 g_3\rangle$ and $|e_2 e_3\rangle$.

For $\Delta_{23}/2\pi > 0$, the quantization axis would have a direction opposite to the one shown in Figure 4.6(b), towards $|g_m e_n\rangle$, causing the state to evolve clockwise in the Bloch sphere. The prepared $|e_2 g_3\rangle + i\,|g_2 e_3\rangle$ state evolving towards $|-\rangle$ initially, results in low counts for $\Delta_{23}/2\pi > 0$ close to $\tau = 0$, in Figure 4.7(b). Subsequently, the emission intensity increases, as the coherent evolution owed to Δ_{23}, transfers population to $|+\rangle$. This reverse evolution with respect to $\Delta_{23}/2\pi < 0$, results in the out-of-phase coherent oscillations of the emission intensity for symmetrical detunings around zero.

The Bloch sphere has been very useful in explaining the dynamics that occur in the single-excitation subspace. With the present excitation scheme of simultaneous drive of both emitters, the doubly excited state $|e_2 e_3\rangle$, which is not represented in this picture, is also populated weakly. However, population of the $|e_2 e_3\rangle$ would not influence the asymmetry in the intensities between positive and negative Δ_{23}, as in both cases $|e_2 e_3\rangle$ will decay with highest probability via the fast channel, through the $|+\rangle$ state.

In short, we have here demonstrated that driving both emitters with the appropriate polarization of the excitation beam, enables the preparation of the system into either $|+\rangle$ or $|-\rangle$, by controlling the detuning Δ_{23} between the emitters. With the current excitation conditions, the population of $|+\rangle$ or $|-\rangle$ occurred after time evolution to this state, due to the presence of Δ_{23}. An interesting next step would then be to deterministically populate either of the two. Initial investigation with the present optical setup showed the ability of mapping different polarizations of the excitation beam to a continuous range of driving θ. This was made possible by analyzing the response of the QDs in RF excitation, to the different angles of the excitation waveplates (Figure 2.5). Selecting then the appropriate waveplate coordinates from the full mapping, would allow to apply a driving with $\theta = 0$ or $\theta = \pi$ and populate $|+\rangle$ or $|-\rangle$, respectively, with small population in $|e_2 e_3\rangle$ and $|g_2 g_3\rangle$ [109]. Furthermore, considering a larger inter-emitter separation x_{mn}, or even driving more than two emitters, would require individual, well phase-locked beams. A robust solution to this could be to employ a Spatial Light Modulator (SLM) to diffract a single light beam, and control the relative excitation phase between the diffracted beam spots by sweeping the grating pattern on the SLM screen. Preliminary exploration of such a device was conducted with the current QDs (Appendix E). Although the proximity of the QD pairs prevented from proper testing[14], the SLM is still considered a promising tool for driving distant QD pairs independently.

[14]The two generated beam spots where partially overlapping, giving rise to interference patterns.

4.5 Summary of the coupling parameters

Parameters	QD2-QD3	QD1-QD2	QD1-QD3
$\{\Gamma_m, \Gamma_n\}/2\pi$, GHz	0.79 , 0.73	0.85 , 0.79	0.9 , 0.65
$\sigma_{sd}/2\pi$, GHz	0.38	0.18	0.33
$\Gamma_{dph}/2\pi$, GHz	0.03	0.03	0.03
ϕ_{mn} , rad	0.05	0.08	0.05
$\Gamma_{mn}/2\pi$, GHz	0.61	0.66	0.61
$J_{mn}/2\pi$, GHz	0.03	0.05	0.03
$\Gamma_+/2\pi$, GHz	1.25	1.36	1.3
$\Gamma_-/2\pi$, GHz	0.27	0.28	0.26

TABLE 4.1: The parameters of the photon-mediated coupling for the three pairs of crossing dipoles, as extracted from modeling with the theory, where Γ_m, Γ_n are the individual decay rates of QD$_m$ and QD$_n$, $\sigma_{sd}/2\pi$ the spectral diffusion linewidth, Γ_{dph} the phonon dephasing rate, ϕ_{mn} the coupling phase, Γ_{mn} the dissipative coupling rate, J_{mn} the dispersive coupling rate, Γ_+ the decay rate of the superradiant state and Γ_- the decay rate of the subradiant state. For all pairs $\sqrt{\beta_m \beta_n} = 0.8$ is used, to obtain a lower bound to the coupling parameters. $\Gamma_\pm$ of QD1-QD3 are calculated using (4.6).

4.6 Summary and Connection

In this Chapter, we demonstrated dipole-dipole photon-mediated coupling, between pairs of QDs, separated by multiple wavelengths. The implementation was enabled by the PCW that the QDs are embedded in and the tuning parameter—the out-of-plane magnetic field— used to bring opposite dipoles of the three QDs to resonance pairwise. The coupling was experimentally observed through the modification of the lifetime measurements when driving in RF a single emitter of a resonant QD pair. In particular, instead of the anticipated single exponential decay of the driven emitter, $\Gamma_3/2\pi = 0.73$ GHz, the emission intensity exhibited a super- and a subradiant component, $\Gamma_+/2\pi = 1.33$ GHz and $\Gamma_-/2\pi = 0.22$ GHz, in the decay, characteristic signatures of coupling between the interacting QDs. The coherent evolution of the collective dynamics was further investigated, with a continues set of lifetime measurements, for a range of detunings, Δ_{23}, between the emitters. The time-resolved dynamics were recorded from both ports of the PCW, and the symmetry in intensity between the two confirmed the predominantly dissipative character of the coupling. This was supported further by modeling the experimental data with the theory, revealing a coupling phase of $\phi_{23} = 0.05\pi$, hence close to the pure dissipative limit condition. This analysis was performed for all three pairs of coupled QDs, where similar coupling parameters were identified, resulting in the same

type of coupling for all crossings. This was attributed to the pre-selection of QDs that are well-coupled to the mode of the waveguide, and consequently with a spatial separation x_{mn} of an integer number of unit-cells. Finally, a first attempt to obtain control over the preparation of a collective state was realized. This was implemented by driving both emitters of the coupled pair with a relative phase, θ and excitation pulse areas Ω_2, Ω_3. Using a single excitation beam to drive both emitters, the θ applied was defined by the local polarization projection of the driving field over the two dipoles of the coupled QD pair. Under this excitation scheme, the super- or subradiant state was populated directly after excitation, depending on the sign of Δ_{23}. However, additional calibration of this excitation method is required to enable population of the collective states on demand.

In the next Chapter, following previous works [51, 52, 54], we probe the collective system with second-order intensity correlation measurements, $g^{(2)}(\tau)$, under continuous excitation, to determine whether coincidence measurements can be used to claim super- and subradiant emission from the coupled system.

5 Anti-dip in photon coincidences from coupled quantum dots

This Chapter is based on the following article (in preparation)

Anti-dip in photon coincidences from coupled quantum dots, C.J. van Diepen, V. Angelopoulou, A. Tiranov, A. Ahmad, O.A. Dall'Alba Sandberg, Y. Wang, L. Midolo, S. Scholz, A. D. Wieck, A. Ludwig, A. Søndberg Sørensen & P. Lodahl

Another approach to observe cooperative emission from a coupled system of quantum emitters, is through second-order intensity correlations, given by

$$g^{(2)}(t,\tau) = \frac{\langle \hat{\alpha}^\dagger(t)\hat{\alpha}^\dagger(t+\tau)\hat{\alpha}(t+\tau)\hat{\alpha}(t)\rangle}{\langle \hat{\alpha}^\dagger(t)\hat{\alpha}(t)\rangle^2}, \tag{5.1}$$

where $\hat{\alpha}^\dagger(t)$ and $\hat{\alpha}(t)$ are the bosonic raising and lowering operators and τ is the correlation time delay. This coherence function measures the degree of correlations in the intensity of a scattered field. In other words, it gives the probability of detecting a photon at time $t+\tau$, given that another one was already detected at time t. To measure $g^{(2)}(\tau)$, a Hanbury Brown Twiss (HBT) experiment is performed [110]. In such a measurement, the emitted field is sent to a 50:50 beamsplitter with one detector on each side. The time correlations of a photon detected in transmission, with respect to photons detected at the reflection of the beamsplitter, are recorded. The setup of the HBT experiment for a pair of coupled quantum dots in a PCW is illustrated in Figure 5.1.

The second-order intensity correlations at $\tau = 0$ for Fock states is given by $g^{(2)}(0) = 1 - 1/N$, where $\langle \hat{\alpha}^\dagger\hat{\alpha}\rangle = N$ is the mean photon number. For a perfect single-photon emitter then, there should be no photon coincidences at zero-time delay, resulting into a dip with $g^{(2)}(0) = 0$, while it can be shown that for a coherent light source $g^{(2)}(0) = 1$. In a system of $N = 2$ off-resonant distinguishable emitters, the coincidence measurements for an ideal system will exhibit a dip at zero-time delay down to $g^{(2)}(0) = 1/2$ for simultaneous driving of both. However, for a pair of indistinguishable emitters, the coincidence at zero-time delay reveals an anti-dip with $g^{(2)}(0) > 1/2$, depending on the decoherence processes, the driving and the relative positions of the detectors. This modification of the correlations can provide insights into the collective character of the interacting emitters.

In the past, this method has been used to probe the collective behavior of two SiV centers in a diamond photonic cavity [111] and two trapped ions

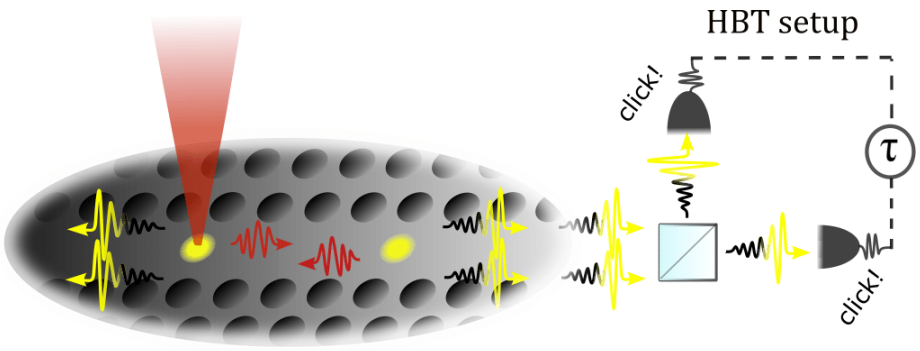

FIGURE 5.1: Illustration of the second-order correlation measurement, for the single-emitter driving. The first of the two QDs (yellow discs) is excited with a CW laser from free space, inside a PCW. When the two QDs are on resonance, they exhibit photon-mediated coupling through the waveguide mode, which results in the emission of photons with modified temporal profile (yellow-black photons). The photons enter the beam-splitter of the HBT setup, that will give the photon statistics.

in free space [112]. The QDs community has also exploited photon coincidences, to declare observation of superradiance. In previous works, QDs exhibit an anti-dip at $\tau = 0$, when brought on resonance, either by strain [52] or thermal tuning [51]. More recently, Z.X. Koong et al. [54] investigated the coupling between a pair of electrically tuned QDs in bulk, that sit approximately a wavelength apart, both with coincidence measurements and time-resolved dynamics. Even though an anti-dip was present in the HBT experiment, the anticipated modification of the lifetime was not observed. Further modeling clarified that zero-time delay coincidences can also arise from correlations induced by measurement or by driving the emitters coherently [55]. These observations led to the conclusion that the zero-time delay anti-dip in second-order intensity correlations, is an indication of cooperative emission, but does not exclusively indicate a direct proof of superradiance. Note that we adhere to the convention where “superradiance" exclusively refers to cases where cooperative emission additionally leads to an increased radiative decay rate of the system, as observed in Chapter 4.

The common element in [51, 52, 100] is that the anti-dip was obtained while driving multiple emitters simultaneously. In this case, the anti-dip can appear due to the detection scheme, which does not allow to distinguish between the two emitters, resulting in measurement-induced cooperativity effects. In this Chapter, we report the observation of photon coincidences from a pair of QDs, when only one of the emitters is driven. We argue that under this excitation scheme, the anti-dip is a direct signature of photon-mediated coupling between the two emitters, associated with superradiant emission. Focusing on the pair of QDs participating in the first crossing of the energy levels in Figure 3.5, we measure the second-order intensity correlations with resonance fluorescence, when the two emitters are detuned and on resonance with each other. We record a transition of $g^{(2)}(0)$ from a dip of

the single emitter, to an anti-dip when brought to resonance. Another feature that becomes apparent during the transition, is the broadening of the dip at longer delay times around zero. This behavior was not present in the previous investigations of the coupling with second-order correlations. By modeling $g^{(2)}(\tau)$, we conclude that it arises from the emission of long-lived single photons, as the broadened dip exhibits a decay rate that matches that of the subradiant state. We further interpret the results by describing the mechanisms that induce the correlations, and support our statements with numerical analysis. Finally, $g^{(2)}(\tau)$ was also probed in resonant transmission. There, the expected correlation peak from two-photon bunching is modified according to the decay dynamics of the coupled system, while tuning the emitters to resonance.

The second-order correlation data discussed in the present Chapter were partially analyzed, modeled, and interpreted at the time of writing of this thesis. We here include the progress made so far, highlight areas of uncertainty, and refer the interested reader to the relevant paper in preparation for more precise conclusions.

5.1 Resonant fluorescence cross-correlation with coupled emitters

For the HBT experiment, we pick up where we left off in the dynamics measurements. We use the same optical path to excite from the top of the waveguide with resonance fluorescence, but this time with a CW laser. The investigation focuses on the QD2-QD3 pair and begins with the driving of a single emitter, specifically of QD3. Prior to the measurement, the optical setup and the excitation scheme had to be adjusted accordingly. We then start by describing the procedure we followed.

5.1.1 Calibration and alignment of optical setup

We begin by optimizing the collection efficiency from Port 1 (Figure 2.4) of the nanostructure. For that, the collection waveplates are calibrated by sending the CW laser from Port 2 through the waveguide, in a transmission measurement. With the bias voltage switched off and the laser locked to about the resonance frequency of QD3 ($\sim$ 318.74 THz), the angles of the HWP and the QWP are scanned and fixed to the values that gave the highest counts in the collection fiber, at the transmission of the PBS (Figure 2.5). Next, the laser is sent through the RF excitation path and is aligned approximately on top of the position of QD3, as determined during the spectroscopy measurements (Chapter 3). Switching off the bias voltage, such that no QD is excited, the laser background is eliminated at the collection by tweaking the angles of the collection waveplates.

We then proceed to refine the alignment of the driving beam on top of the waveguide for QD3. As the QDs are close in proximity, approximately within the diameter of the diffraction-limited beam spot on the sample, proper alignment and waveplate calibration are required to ensure the

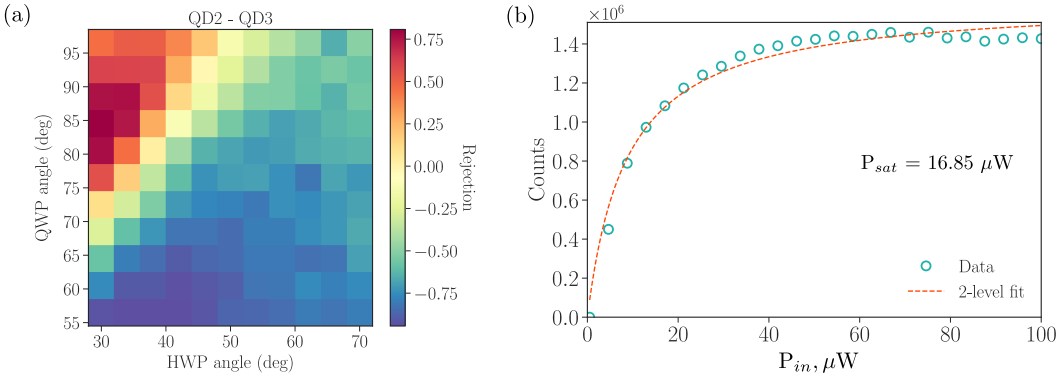

FIGURE 5.2: (a) Calibration of the waveplates in the excitation path, for the pair of QD2-QD3 dipoles. For $B_z = 0.8$ T, far from their crossing, we measure the difference in counts from the two dipoles (Rejection colorbar), for all angle combinations of the HWP and QPW. (b) Saturation measurement of the low frequency dipole of QD3, with the CW laser power, as it is measured before attenuation. The expression used for the fit (dashed line) and the saturation power P_{sat} estimation, is included in the main text.

driving of the low-frequency dipole of QD3 and the suppression of QD2. We begin with iterative beam-walking on top of the position of QD3 to obtain good signal-to-noise ratio (SNR) and a saturation measurement is performed for each iteration. Figure 5.2 (b) shows an indicative saturation curve. The optimal position of the beam is found for high SNR and low saturation power.

Further, the polarization of the excitation beam needs to be calibrated to optimally excite the low-frequency dipole of QD3, while simultaneously suppressing the opposite dipole of QD2. For that, we lock the CW laser frequency to the value that excites both QD2 and QD3 resonantly at the crossing ($\sim$ 318.754 THz). For a low B_z ($\sim$ 0.8 T), such that the crossing dipoles are spectrally separated, we perform voltage scans to find the values for which each QD is resonant with the laser. For these two voltages[1], the excitation HWP and QWP are scanned step-wise, and two 2D maps of the emission from QD2 and QD3 are collected. To find the optimal orientations for HWP and QWP, the difference of these maps is used. An example of this is shown in Figure 5.2(a), where the normalized difference of the counts between the crossing dipoles of QD2 and QD3 is shown. We then select a combination of HWP and QWP that gives a large difference between the two, hence simultaneously high counts from QD3, and, more importantly, good suppression of QD2.

Additional voltage scans and beam-walking are often needed to optimize further the SNR. By iterating over voltage scans, beam walking and waveplate scans, we converge to the alignment that gives a high difference in counts between the two dipoles, $\pm$ 0.98 (Rejection colormap in Figure 5.2(a)) and SNR of 250, sufficient to begin with the longer spectroscopic

[1]We scan around the central voltages for each combination of HWP and QWP to ensure that we trace the counts at the resonant excitation

measurements.

5.1.2 Resonance fluorescence spectra of coupled emitters

The first measurement that would allow to verify single emitter excitation, is to record the resonance fluorescence spectra as a function of detuning between the emitters, $\Delta_{23}/2\pi$. For that, the CW laser is set at the frequency for which the two dipoles come to resonance, and the magnetic field B_z is scanned around the crossing value ($\sim B_z = 1.07$ T). For each B_z, the bias voltage is scanned, such that the QD3 transition is always resonant with the laser frequency.

Figure 5.3(a) shows the result of this scan[2], where the vertical axis is the frequency offset[3] from the crossing value. The white dashed line represents the expected resonance of the laser with QD2, following Figure 3.5, whose excitation is well suppressed throughout the scan. In combination with the counts recorded from the emission of QD3, the plot confirms the direct driving of the low frequency QD3 dipole after calibration.

Here, the feature that stands out in the spectra is the decrease of the fluorescence signal of QD3, at the crossing with QD2 ($\Delta_{23}/2\pi$ = 0). This occurs since the photons emitted by QD3 are coherently reflected by QD2 when the two emitters are on resonance, resulting in the observed extinction in transmission[4] at $\Delta_{23}/2\pi = 0$ [113].

5.1.3 Photon coincidences from single-emitter driving

To measure now the second-order intensity correlations $g^{(2)}(\tau)$, the scattered light collected from Port 1 is send to a 50:50 (fiber) beamsplitter, with one detector[5] on each side, as depicted in Figure 5.1. The coincidence histogram of the clicks between the detection events at the two detectors are analyzed by a time-to-digital converter (time-tagger[6]). The excitation power we send to the emitter is estimated by fitting the saturation measurement shown in Figure 5.2(b) with $\rho_{ee} = \frac{P_{in}/P_{sat}}{1+2P_{in}/P_{sat}+4\Delta^2/\gamma^2}$, where ρ_{ee} the excited state population of the steady state solution for a two-level emitter [87]. The excitation power was $P_{in}/P_{sat} \approx 0.12$, where P_{sat} is the saturation power of QD3. For the transparency of our procedure, we note here that this saturation curve is an indicative measurement on QD3 to get an estimation of the driving frequency from the relation $\Omega_3 = \sqrt{\frac{P_{in}}{P_{sat}}}\Gamma_3$, where Γ_3 is the decay rate of QD3, neglecting here the spectral diffusion of the emitter. This gives an estimated Rabi frequency of $\Omega_3/2\pi = 0.25$ GHz = $0.35\,\gamma_3$, where $\gamma_3 = \Gamma_3/2\pi$ the linewidth of QD3.

[2] An APD was used.

[3] Converting the voltage scan to frequency, from the Stark tuning of Figure 3.4, and taking the offset from the crossing of the two dipoles.

[4] Here the data are collected from Port 2 of the PCW.

[5] SNSPDs were employed.

[6] PicoHarp 300

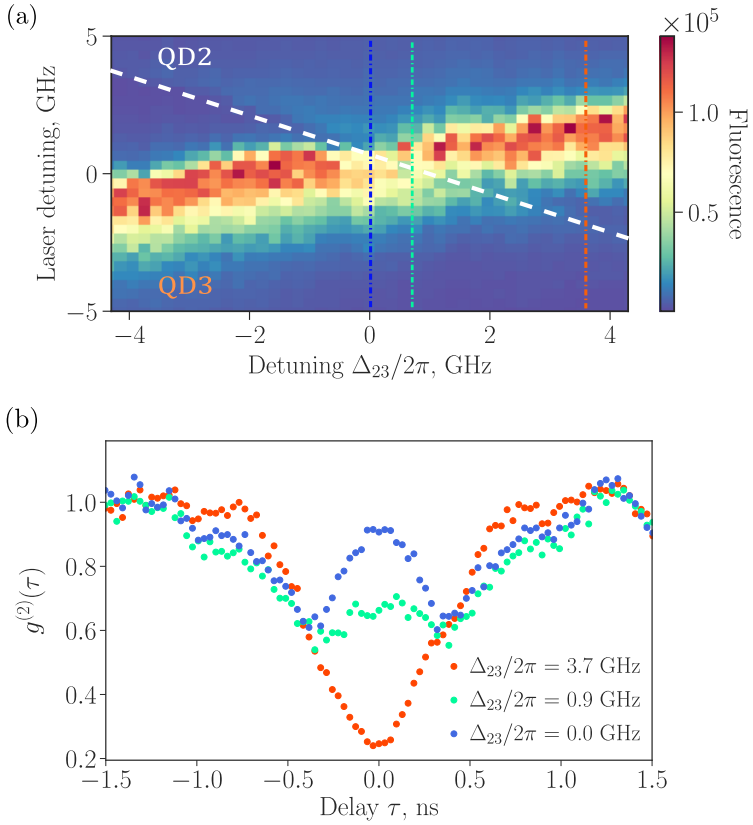

FIGURE 5.3: (a) Resonance fluorescence of QD3, as a function of the detuning between QD2-QD3. The white dashed line traces the expected spectral emission from QD2, whose excitation is prohibited by spacial and polarization selectivity of the laser. (b) Two-photon correlations $g^{(2)}(\tau)$ for three detunings $\Delta_{23}/2\pi$, color-coded with the dot-dashed vertical lines in (a).

The obtained $g^{(2)}(\tau)$ is shown in Figure 5.3(b) for three different detunings between the two QDs, $\Delta_{23}/2\pi$, normalized to photon coincidences at longer times[7] after exciting QD3. Since we drive only one emitter, the characteristic single-emitter dip approaching zero is expected when the two are far from resonance. Indeed, the coincidence counts for a large detuning (red) revealed anti-bunching of the emitted photons, with $g^{(2)}(0) \approx 0.24$. The parameters that could prevent $g^{(2)}(0)$ from reaching lower values, are potentially the imperfect extinction of the laser background in the waveguide, following the relation $g^{(2)}(0) = 2\xi - \xi^2$ where $\xi = 1/$ SNR including the background emission from the sample, [114] and the time-jitter of the detection. Here, after fitting with the IRF of the detectors, we determined that $g^{(2)}(0)$ is within the range $0.12 - 0.15$. Accounting for the SNR, the dip reaches a minimum of approximately $g^{(2)}(0) \approx 0.1$, with the remaining attributed to the coupling to the waveguide. The intermediate detuning (green) is simply shown to highlight the transition of the features as the dipoles are tuned from distinguishable (off-resonance $\Delta_{23}/2\pi \neq 0$) to indistinguishable (on-resonance $\Delta_{23}/2\pi = 0$). When the two QDs are brought

[7] The oscillations that are present at longer times arrive from crosstalk between the two channels of the time-tagger.

to resonance (blue), a clear anti-dip approaching $g^{(2)}(0) \approx 0.94$ is measured, while, at longer delay times ($|\tau| \approx 0.4$ ns), the single-emitter dip gets broader. By modeling $g^{(2)}(\tau)$ with the empirical convolution function of the sum of the standard RF dip with an exponential for the anti-dip [47],

$$g^{(2)}(\tau) = 1 - e^{-\left(\frac{3\Gamma_{dip}}{4}+\frac{\Gamma_{dph}}{2}\right)\tau}\left(\cos(\mu\tau) + \frac{3\Gamma_{dip}+2\Gamma_{dph}}{4\mu}\sin(\mu\tau)\right) + e^{-\Gamma_{adip}\tau} \tag{5.2}$$

where Γ_{dph} is the pure dephasing rate and $\mu = \sqrt{\Omega_3^2 + \left(\frac{\Gamma_{dip}-2\Gamma_{dph}}{4}\right)^2}$, convolved with the IRF of the detection, we obtain the linewidths of $\Gamma_{adip}/2\pi = 1.44 \pm 0.16$ GHz and $\Gamma_{dip}/2\pi = 0.31 \pm 0.03$ GHz. Those appear to be in agreement with $\Gamma_+/2\pi = 1.33$ GHz of super- and $\Gamma_-/2\pi = 0.22$ GHz of subradiance respectively for the QD2-QD3 pair, found from the analysis of the lifetime data (see Table 4.1).

5.1.4 Interpretation of the photon coincidences

The feature of the anti-dip has been observed in all works previously mentioned with QDs [51, 52, 54]. There, since more than one emitters were excited simultaneously, the presence of the anti-dip is attributed to emission from the collective doubly excited state $|ee\rangle$, that is directly populated by the laser excitation. The population of $|ee\rangle$ is a prerequisite for photon coincidences, as it leads to emission of two subsequent photons, which can coincide in time at the two detectors. The novelty of Figure 5.3(b) lies in the single emitter drive. In order to populate $|ee\rangle$ with this excitation scheme, there needs to be a process that would induce interaction between the emitters, such that the driving of the first would also excite the second, i.e. the distant emitters need to be coupled through a shared optical mode.

To understand better the underlying mechanisms that give rise to the features around zero-time delay, we make use of the energy level diagrams in Figure 5.4. Describing one QD as a two-level system with a $|g\rangle$ and an $|e\rangle$ state, a pair of resonant QDs can be represented by a four-level system, as shown in Figure 5.4(a), where m = 3 and n = 2 for the discussed pair. As QD3 is coherently driven with a Rabi frequency $\Omega_3/2\pi$, $|e_3g_2\rangle$ gets populated. The excitation then dissipates with rate Γ_3 and brings the excitation to QD2 through the mode of the waveguide. The population is then in part transferred to $|g_3e_2\rangle$, due to the photon-mediated coupling between the QDs, indicated with the double-sided arrow, representing Γ_{mn}, the dissipative coupling rate. Since QD3 is driven continuously, the doubly excited state $|e_3e_2\rangle$ gets populated. Upon its decay to $|g_3g_2\rangle$, two subsequent correlated photons are emitted from the coupled system.

To discuss in more depth the effects of the dynamics that occur due to the coupling, it is natural to turn to a four-level system in the basis of $|+\rangle = \frac{1}{\sqrt{2}}(|e_3g_2\rangle + |g_3e_2\rangle)$ and $|-\rangle = \frac{1}{\sqrt{2}}(|e_3g_2\rangle - |g_3e_2\rangle)$ of the single excitation subspace, depicted in Figure 5.4(b). As argued in Chapter 4, the coupling between the two emitters is predominantly of dissipative character,

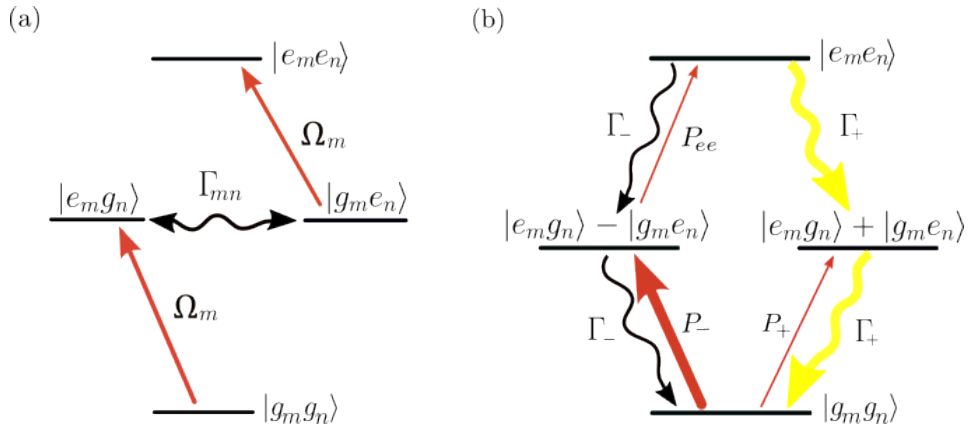

FIGURE 5.4: Energy level diagrams that describe the mechanisms taking place in the system under CW excitation, in (a) the individual-emitters basis and (b) the collective basis. In (a) the QD_m is driven with Ω_m. Through photon mediated interaction (double-sided arrow Γ_{mn}) and continuous drive (red arrows), the doubly excited state $|e_m e_n\rangle$ gets populated. In (b) the drive is shown in terms of pumping rate P, taking into account the big difference between the collective decay rates, $\Gamma_\pm$.

and therefore $|+\rangle$ and $|-\rangle$ are degenerate in energy, but maximally modified in their decay rates, $\Gamma_\pm$. In this picture, the initial state is $|e_3 g_2\rangle = \frac{1}{\sqrt{2}}(|+\rangle + |-\rangle)$. However, we do not in fact drive to $|e_3 g_2\rangle$, as the probabilities to populate $|+\rangle$ and $|-\rangle$ are not equal. That is because the population of $|+\rangle$ and $|-\rangle$, depends on the rate at which each state decays $\Gamma_\pm$ (Table 4.1) with respect to the driving frequency $\Omega_3/2\pi$. Given a weak drive of QD3, with respect to the superradiant decay rate ($\Gamma_- < \Omega_3 < \Gamma_+$), this results into different pumping rates $P_- = \Omega_3^2/\Gamma_-$ and $P_+ = \Omega_3^2/\Gamma_+$ for the two states, indicated by the thickness of the red arrows [27].

More specifically, as the superradiant state decays faster than the applied driving to the system, it will be populated with very low probability, meaning effectively a low pumping rate, P_+. This can be explained by the quantum Zeno effect [79], which suggests that: a state that is measured more frequently than it decays will essentially never decay, since the measurement continuously projects it back to the initial state. In our system, it is the fast decay of the superradiant state which represents the frequent measurement by the environment in terms of the quantum Zeno effect. This means that $|+\rangle$ is hard to excite with a weak drive, as its fast decay projects it continuously back to $|g_3 g_2\rangle$. Therefore, in this subspace, most of the population remains in the collective ground state, $|g_2 g_3\rangle$.

On the other side of the temporal spectrum, is the subradiant state $|-\rangle$, which decays much slower than it gets populated, leading to a high pumping rate $P_- > P_+$. Due to the continuous drive, part of the population will transition to the doubly excited state $|e_3 e_2\rangle$. Here, the quantum Zeno argument used for the population of $|+\rangle$ also holds for $|e_3 e_2\rangle$, resulting in a weak pumping rate $P_{ee} < P_-$ for the doubly excited state. Hence, the population of the system accumulates in the slowly decaying $|-\rangle$.

The population that ends up in $|e_3 e_2\rangle$ will decay with high probability

through the fast channel (yellow arrows in Figure 5.3(b)), or in other words through the two-step Dicke ladder $|e_2e_3\rangle \rightarrow |+\rangle \rightarrow |g_2g_3\rangle$. The two subsequently emitted fast decaying photons give rise to the observed anti-dip. More precisely, the detection of the first photon ($|e_2e_3\rangle \rightarrow |+\rangle$) will project the system to the superradiant state, which will emit the second fast photon right after with high probability. The anti-dip at zero-time delay is then related to the probability that these two photons arrive together at the two detectors, and its decay essentially follows the temporal shape of the second fast decaying photon. The decay rate of the anti-dip, Γ_{adip}, is then directly related to the superradiant decay rate, Γ_+. In addition, the effective two-level system formed by $|g_3g_2\rangle$ and $|-\rangle$, decays by emitting one slow-decaying photon, causing the broadening of the dip at longer delay times. The decay rate of the dip Γ_{dip}, is then linked to the subradiant decay rate, Γ_-. A last small contribution on $g^{(2)}(\tau)$ comes from the single photons emitted with small probability from the decay of $|+\rangle$ to $|g_3g_2\rangle$. These short-lived photons are expected to overall decrease the photon coincidences $g^{(2)}(0)$, and narrow the width of the dip, opposing the broadening from the subradiance.

5.1.5 Numerical simulations for various experimental conditions

Making use of the theory that was developed for the coupled QDs in the waveguide (see Section 1.4), we move on to model the second-order correlations, to probe the effects of the different parameters on the photon statistics and further support our interpretations about the coupled system.

To do so we use the formula for the normalized second-order correlation function (5.1), which can be transformed into

$$g^{(2)}(\tau) = \frac{\mathrm{Tr}\left(\hat{\alpha}(t+\tau)\rho'(t+\tau)\hat{\alpha}^\dagger(t+\tau)\right)}{\mathrm{Tr}\left(\hat{\alpha}(t)\rho(t)\hat{\alpha}^\dagger(t)\right)^2} \tag{5.3}$$

where, $G^{(2)}(\tau) = \mathrm{Tr}\left(\hat{\alpha}(t+\tau)\rho'(t+\tau)\hat{\alpha}^\dagger(t+\tau)\right)$ is derived by the quantum regression theorem [57] and $\rho'(t+\tau)$ comes from $\rho'(t) = \hat{\alpha}(t)\rho(t)\hat{\alpha}^\dagger(t)$ after time evolution $t \rightarrow t+\tau$.

In Figure 5.5(a) we show now the full scan of $g^{(2)}(\tau)$ as a function of detuning $\Delta_{23}/2\pi$, around the crossing of QD2-QD3 dipoles, and compare with its numerical simulation in Figure 5.5(b). The model was calculated for the experimental parameters of Table 4.1 and for driving QD3 dipole with a rate equal to $0.5\gamma_3$. To account for spectral diffusion, the model is averaged over a Gaussian distribution of detunings around the resonant transition of QD3, with standard deviation σ_{sd}. Finally the result is convolved with a Gaussian to include the time-jitter effect.

The modeled $g^{(2)}(\tau)$ shows many similarities to the experimental data. The anticipated transition from the single-emitter dip to the anti-dip is present in both. A common feature that becomes apparent is the asymmetry of the resonance value $\Delta_{23}/2\pi = 0$ GHz (black dashed line in 5.5(a)), with respect to the presence of the anti-dip at small detunings. This asymmetry is

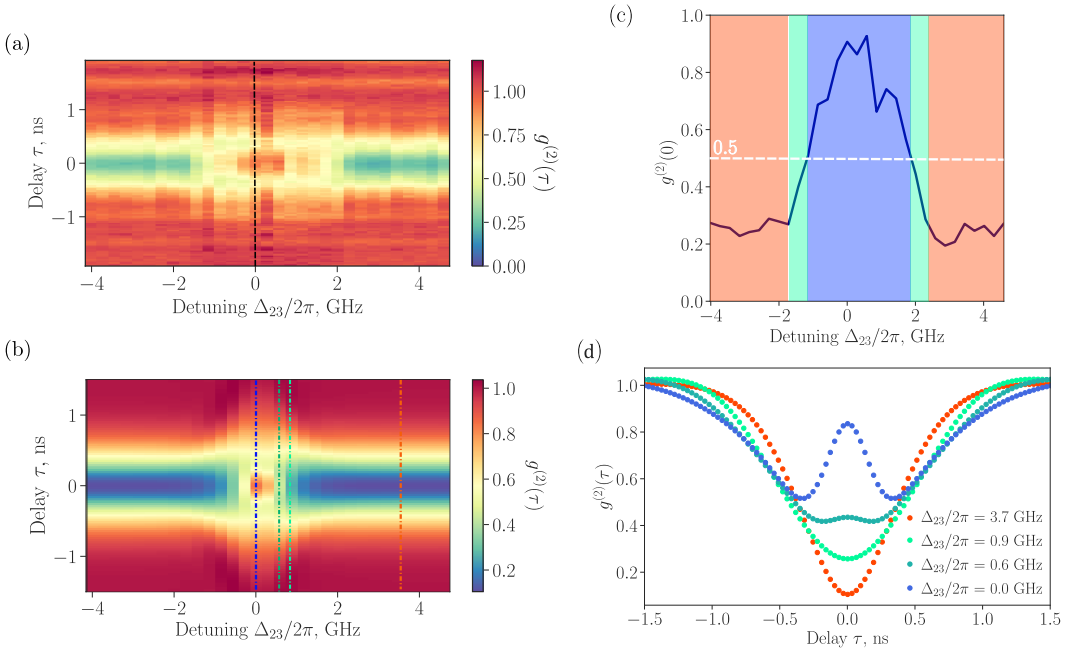

FIGURE 5.5: (a) Experimental data of second order intensity correlations of QD2-QD3, as a function of the detuning $\Delta_{23}/2\pi$. (b) Numerical simulation of the experiment shown in (a), using the model developed for the HBT experiment of the coupled system. (c) $g^{(2)}(0)$ throughout the scan of $\Delta_{23}/2\pi$. (d) Simulation of the second order intensity correlations for four different detunings between QD2-QD3. Their positions on the overall scan (b) are noted with dot-dashed vertical lines. The detunings are chosen to match the $g^{(2)}(\tau)$ traces shown in Figure 5.3(b).

attributed to the small deviation of the coupling phase from the ideal $\phi_{23} = N\pi$ of the dissipative coupling. More specifically, the $\phi_{23} = 0.05$ rad that was found for the spatial separation of QD2 and QD3, causes imperfect interference of the fields from the two emitters at the collection ports. That effect can be compensated by the presence of a small detuning between the emitters. The result is then the appearance of the maximum of the anti-dip at larger $\Delta_{23}/2\pi$ values. It is important to note here as well, that the definition of $\Delta_{23}/2\pi = 0$ GHz from the resonant transmission measurement (Figure 3.5) is again an estimate for the resonance of QD2-QD3. In reality the magnetic field for which the emitters come to resonance, deviates by about 0.04 T in the various measurements done for this crossing. This shift differs depending on the type of driving (CW or pulsed), the excitation scheme (RT or RF), the driving power (Figure A1), as well as on the nuclear spin dragging, caused by the nuclei in the vicinity of the two interacting emitters [19].

Another feature of the experimental data that is though not well reproduced in the theory plot, is the range of detunings for which the anti-dip is present. In the experiment the presence of the anti-dip extends to larger detunings between the emitters ($\Delta_{23}/2\pi \approx 1$ GHz) than in the simulation. This is, for now, attributed to the nuclear spin dragging that the emitters experience, which is not included in the theoretical model we use. Specifically, we note that the dipole of QD3 driven by the laser, undergoes anti-dragging

by the nuclear spin bath. The anti-dragging of the QD transition effectively increases the spectral diffusion of the dipole, broadening the dependence of the anti-dip on the detuning $\Delta_{23}/2\pi$. The nuclear spin is therefore responsible for the abrupt changes observed in the RF spectra of Figure 5.3(a), and limits the value of the anti-dip $g^{(2)}(0)$.

The transition of the experimental $g^{(2)}(0)$, is traced for all detunings in Figure 5.5(c). We divide the plot into three regimes. At large enough detunings, $|\Delta_{23}/2\pi| > |\Gamma_2/2\pi + \Gamma_3/2\pi|$ (orange), $g^{(2)}(\tau)$ give the characteristic single-emitter dip, as only one QD is driven. For a small range of detunings (green), QD2 appears to be excited by the photons emitted by QD3, since the two start to overlap in frequencies due to their respective spectral diffusion. However, as they are still distinguishable, the dip of the second-order coincidences reaches up to $g^{(2)}(\tau) = 0.5$. From there on an anti-dip starts to appear, as the probability of populating the doubly excited state increases with smaller detunings (blue). To explain the gradual increase of the anti-dip with detuning as we move towards the resonant condition, we recall the description of the dynamics that occur in Section 4.3 and make use of a more intuitive expression of the zero-time delay photon coincidences for super- and subradiant emitters[8],

$$g^{(2)}(t,0) = \frac{\Gamma_3^2\,\rho_{ee}(t)}{(\Gamma_3\rho_{ee}(t) + \frac{\Gamma_+}{2}\,\rho_+(t) + \frac{\Gamma_-}{2}\rho_-(t))^2}, \tag{5.4}$$

where ρ_{ee}, ρ_+ and ρ_- are the populations in the doubly excited, the super- and the subradiant states, and $\Gamma_\pm = \Gamma_3 \pm \Gamma_{23}$ from (4.6) while neglecting spectral diffusion. Before continuing the discussion, it is important to highlight that, contrary to the pulsed excitation which revealed coherent oscillations in the population between the super- and the subradiant states, with CW driving the coupled system reaches steady state values for all populations. The presence of detuning $\Delta_{23}/2\pi$, will cause exchange of population between the super- and the subradiant states. Specifically, for detunings in $\Gamma_{23}/2\pi < |\Delta_{23}/2\pi| < \Gamma_+/2\pi$, the anti-dip remains small, as part of the subradiant population is transferred to the superradiant state. As then ρ_+ increases, the anti-dip $g^{(2)}(0)$ decreases. This exchange of population occurs slower as the detuning gets smaller. For $|\Delta_{23}/2\pi| < \Gamma_{23}/2\pi$, where the dissipation starts to dominate, the population starts to accumulate in the subradiant state, and from there it can get re-excited to $|e_3e_2\rangle$. At the resonant condition, the anti-dip reaches its highest value and the dip its maximum width, as there are now less fast single photons that would narrow it down.

Finally, Figure 5.5(d) shows traces of the simulated $g^{(2)}(\tau)$, for the detunings depicted in Figure 5.3(b). The simulation demonstrate a good agreement between the experiment and the theoretical prediction, and validate the experimental parameters extracted by the analysis of the lifetime data in Chapter 4.

To further support the claim that, in the single-emitter excitation regime, the anti-dip in photon coincidences is a clear indication of coupling between

[8]This formula is inspired by [55].

two resonant emitters, we exploit the model to show how $g^{(2)}(\tau)$ is affected by different strengths and types of coupling. For these simulations, the experimental parameters were used as before, but the contributions from spectral diffusion and time-jitter have been neglected, in order to highlight more explicitly the rising effects.

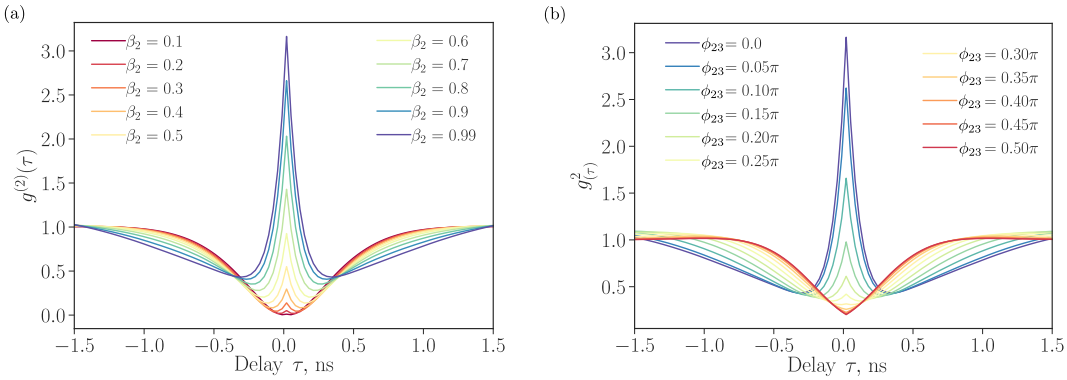

FIGURE 5.6: Simulations of $g^{(2)}(\tau)$ of two indistinguishable emitters for different (a) coupling strengths to the waveguide mode of the non-driven emitter, β_2, and a coupling phase of $\phi_{23} = 0$ rad and (b) coupling phases ϕ_{23} and ideal coupling parameters $\beta_2, \beta_3 = 0.99$ for both QDs.

To probe the effect of the coupling strength on the intensity correlations, we plot $g^{(2)}(\tau)$ with an increasing coupling parameter of QD2 to the waveguide mode, β_2 (Figure 5.6(a)). For all traces the coupling phase is fixed to $\phi_{23} = 0$ rad, to ensure dissipative coupling between the emitters. For the weakest coupling to the waveguide mode, $\beta_2 = 0.1$, the system behaves as if there is only a single emitter in the waveguide and gives the characteristic dip in photon coincidences (dark red). As the coupling of QD2 to the waveguide strengthens, its interaction with QD3 via the shared waveguide mode increases, leading to the gradual emergence of an anti-dip at zero-time delay. In other words, this plot emphasizes that driving a single emitter alone does not yield observable photon coincidences, as we see experimentally, unless there is strong coupling between the emitters through the mode of the waveguide.

To illustrate that the type of coupling is also related to the presence or absence of the anti-dip, in Figure 5.6(b) we simulate the behavior of $g^{(2)}(\tau)$ throughout the transition between the two coupling regimes, i.e. from dissipative ($\phi_{23} = 0$) to dispersive ($\phi_{23} = \pi/2$), by scanning the coupling phase, ϕ_{23} between two emitters with nearly-ideal coupling to the waveguide mode, $\beta_2, \beta_3 = 0.99$. From the outcome, one could conclude that the probability of getting two photons out of the coupled system decreases with increasing ϕ_{23}. Specifically, the anti-dip is completely absent at the dispersive limit, $\phi_{23} = \pi/2$, while it maximizes at the dissipative, $\phi_{23} = 0$. This result would then directly relate the anti-dip emergence to a dissipative character of the coupling between two well coupled emitters. However, we note that further investigation with numerical simulations showed that the presence of an anti-dip from one collection port does not exclusively indicate dissipative coupling. Similar to the argument discussed in Section 4.4, it is

important to consider the photon statistics from both ports of the waveguide, taking into account which QD is driven. Therefore, our experimental data presented here is insufficient to conclude on the type of coupling with certainty.

In both plots of Figure 5.6 the simulations show clear bunching ($g^{(2)}(\tau) > 1$) for $\beta_2 \geq 0.7$ and $\phi_{23} \leq 0.15\pi$, which was not observed experimentally for $\beta_2 = 0.8$ and $\phi_{23} = 0.05\pi$. We attribute the limitation of the anti-dip to a combination of experimental imperfections in our system, such as the pure dephasing, spectral diffusion, the driving power, Ω_3, the limited β-factors and the imbalanced decay rates of the two QDs.

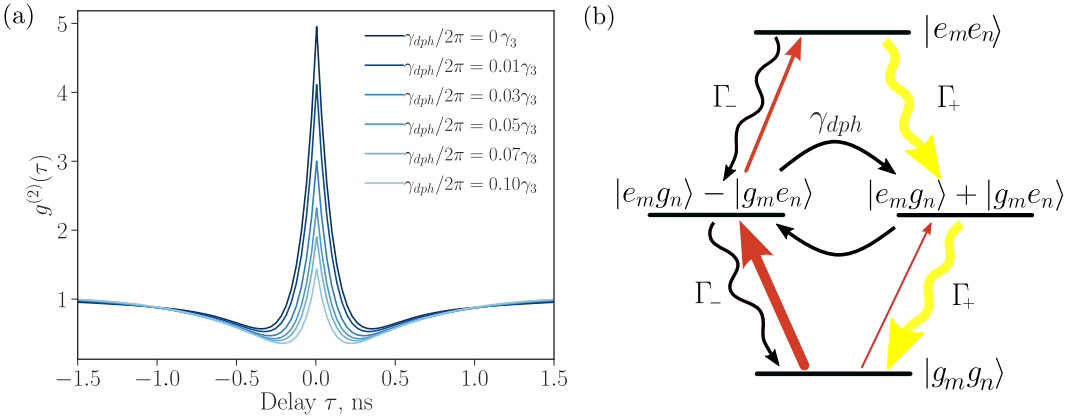

FIGURE 5.7: (a) Simulation of $g^{(2)}(\tau)$ of two indistinguishable emitters as a function of pure dephasing, γ_{dph}, for fixed $\Omega_3/2\pi = 0.5\gamma_3$. (b) Energy diagram showing the effect of pure dephasing to the populations of the collective states.

To clarify the effects that two of these parameters have on the photon coincidences of two resonant emitters, we simulate $g^{(2)}(\tau)$ for different values of pure dephasing, γ_{dph} in Figure 5.7, and driving power Ω_3 in Figure 5.8.

The simulation for different pure dephasing (Figure 5.7(a)) shows that even small amounts of such decoherence will quickly damp the mechanisms that give rise to the anti-dip. The dynamics that γ_{dph} induces are illustrated in Figure 5.7(b). Pure dephasing of the system will cause oscillations between the collective $|+\rangle$ and $|-\rangle$ states, similar to the detuning. As argued before, this results into the emission of more single photons from the decay of $|+\rangle$, which consequently decreases the photon coincidences (seen from (5.4)). However, in contrast to detuning, this process is incoherent, adding time-varying phase to the photon-mediated interaction. This would disrupt the constructive and destructive interference, damping the features that indicate super- and subradiance. The loss of coherence becomes evident in the decreasing width of the dip and the anti-dip, with increasing γ_{dph}.

Finally, the photon coincidences $g^{(2)}(\tau)$ of the cooperative emission for continuous and coherent driving is plotted for different Rabi frequencies $\Omega_3/2\pi$ in Figure 5.8(a). To understand the impact that the different driving has on the coupled system, the populations at the steady state for each $\Omega_3/2\pi$ are also plotted in (b). The first effect of the increasing driving frequency to notice is the decrease of the anti-dip and width of the dip. This

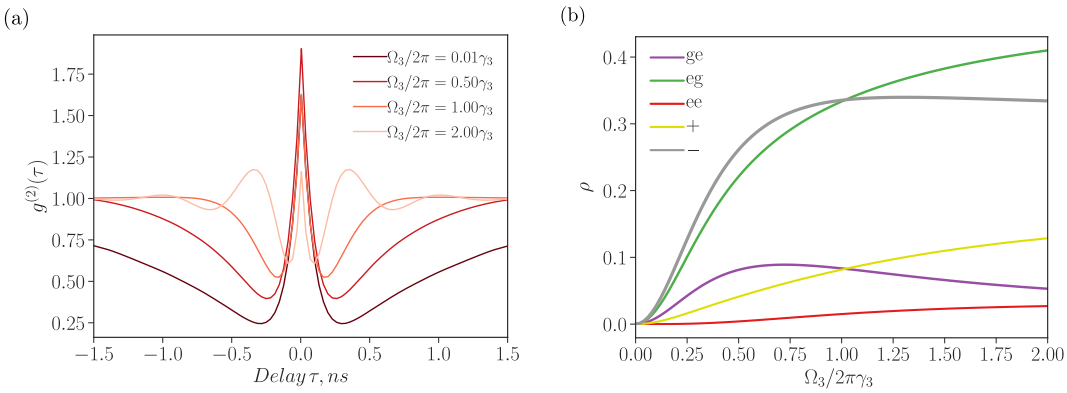

FIGURE 5.8: (a) Simulation of $g^{(2)}(\tau)$ of two indistinguishable emitters as a function of $\Omega_3/2\pi$, for fixed pure dephasing at $\gamma_{dph}/2\pi$ = 0.07 γ_3. (b) Populations of the individual emitters and their collective states, as a function of $\Omega_3/2\pi$.

can be justified, as before, by the increasing population in $|+\rangle$ (ρ_+ yellow line in 5.8(b)). The oscillations (shoulders) of $g^{(2)}(\tau)$ appearing at longer times for high driving frequencies, are indicative of Rabi flopping in the two-level system. Another feature that becomes apparent is that the anti-dip remains the same up to $\Omega_3/2\pi = 0.5\gamma_3$ and decreases for stronger driving. This highlights the fact that to obtain the highest bunching, $\Omega_3/2\pi$ should be low enough such that the superradiant state is hardly excited. For the conditions of the present experiment this seems to occur for Rabi frequencies around $\Omega_3/2\pi = 0.5\gamma_3$. With this low driving frequency the population in the subradiant state, that is the requirement for the emergence of the anti-dip, has been well accumulating (ρ_- gray line), while the superradiant population is still low and the doubly excited state just begins to be populated (ρ_{ee} red line).

As a final remark here, looking at $g^{(2)}(\tau)$ of the lowest simulated $\Omega_3/2\pi$, one could wonder, why the anti-dip exceeds 1 when the doubly excited state is barely populated for $\Omega_3/2\pi < 0.5\gamma_3$. This feature is not the result of two-photon detection, but of how rare these coincidences are. To explain this paradoxical result, we retrieve to the intuitive expression for $g^{(2)}(0)$ (5.4). In the limit of low power, where the population in $|+\rangle$ is very small, the expression could be simplified to $g^{(2)}(0) \approx \frac{1}{\rho_{ee}}$. Therefore, the low population in $|e_3e_2\rangle$ can result in $g^{(2)}(0) > 1$. In fact, the bunching can become infinitely large in the limit of weak driving.

5.1.6 Driving the less noisy emitter

The resonance fluorescence and second-order correlation measurements (as in Figure 5.3) were repeated, while driving QD2 instead. Surprisingly, the anticipated decrease in counts in the resonance fluorescence and the anti-dip at $g^{(2)}(0)$ in resonant conditions between the two emitters, were not observed. The absence of these features is attributed to the response to the noise exhibited by each of the QD2-QD3 dipoles and the post-selective

nature of the $g^{(2)}(\tau)$ measurement.

More specifically, in a HBT experiment there will be no signal in the cases where the laser is off-resonant with the addressed QD. Therefore, the measurement effectively post-selects the cases where the light and the emitter are resonant. Due to the nuclear spin of the solid-state environment, QD2 experiences dragging, which broadens its RT dip, reducing the effect of spectral diffusion. As mentioned previously, QD3 undergoes anti-dragging, which has the opposite effect, complicating the task of maintaining its dipole transition resonant to the laser frequency consistently. This implies that when QD3 is driven, it naturally benefits the post-selection of the cases where its transition is resonant with the laser and with the less noisy QD2 dipole, resulting in more pronounced signatures of the coupling, as depicted in Figure 5.3(b). On the other hand, when QD2 is driven, the probability of having both QD2 and QD3 dipoles in resonance with the laser is low. This results in reduced effects from the photon-mediated coupling on $g^{(2)}(\tau)$, washing out the coupling features.

To support the hypothesis about the noise, further investigation along with numerical simulations are still pending. The experimental results are included in Appendix D.

5.2 Photon coincidences in resonant transmission

The coupled system was probed also in RT, with continuous and coherent driving, sent through the waveguide from Port 2. Using an attenuated beam of the CW laser, with frequency fixed to the value for which the dipoles come to resonance, the magnetic field is scanned along the crossing. The voltage is respectively scanned such that each QD is excited resonantly at all B_z values.

The resonant transmission spectra are depicted in Figure 5.9(a), where the RT dips reach their maximum depth at the crossing resonant frequency. The transmission counts are normalized to the background, collected with bias voltage of 1 V, such that no QDs were driven. We note that the widths of the two dips differ, due to the different contribution of the spectral diffusion on each dipole from the nuclear spin noise at increasing magnetic fields. Specifically, QD3 exhibits more noise compared to QD2, as its dipole is being anti-dragged by the nuclear spin, leading to a shift in its transition away from the laser frequency. On the other hand, the dipole of QD2 undergoes dragging, which imparts a square-like shape to its RT spectra.

For every detuning, a $g^{(2)}(\tau)$ measurement is recorded, while exciting each QD individually, by choosing the bias voltage. Figure 5.9(b) shows three second-order correlation measurements, when driving QD2. The photon coincidences were normalized to the coincidences at long delays. For this excitation scheme, $g^{(2)}(\tau)$ exhibits a bunching peak at zero-time delay for all detunings. The bunching is induced by the nonlinear single photon response of the QD to a weak driving field [103], while its profile is modified according to the altering photon-statistics throughout the scan. The traces in (b) show decreasing bunching from $g^{(2)}(\tau) \approx 4.5$ at large detunings, down

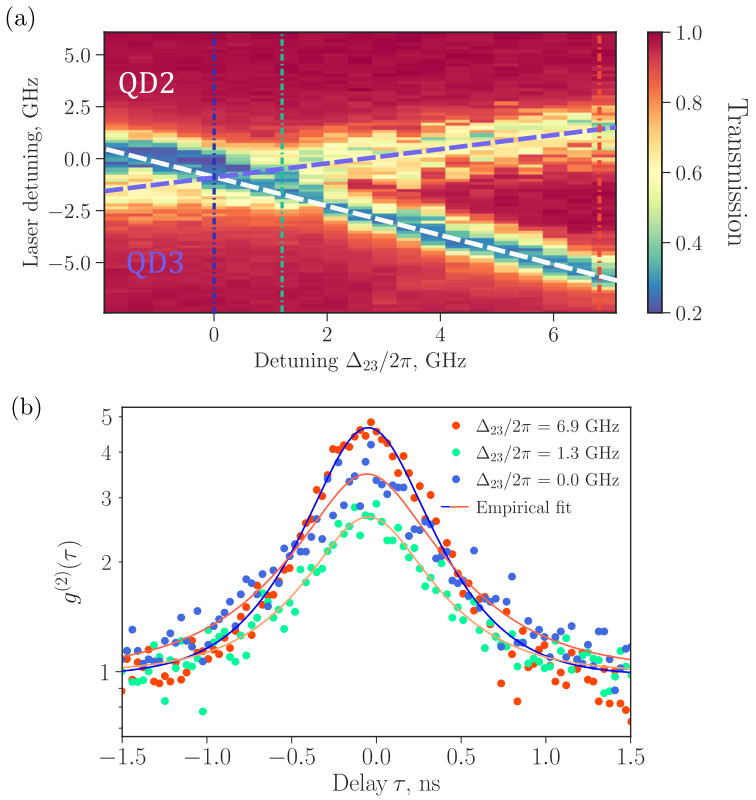

FIGURE 5.9: (a) Resonance transmission measurement, as a function of the detuning between the two crossing dipoles of QD2-QD3. (b) Two-photon correlations for three detunings $\Delta_{23}/2\pi$, color-coded with the dot-dashed vertical lines in (a), when driving QD2. The three traces come from Figure 5.10(a).

to 3.5 at $\Delta_{23}/2\pi = 0$, and broadening of the width that maximizes when the two QDs come to resonance. Plotting the photon coincidences in logarithmic scale and fitting them with a single exponential convolved with a Gaussian to account for IRF (Empirical fit lines in Figure 5.9(b)), facilitates the observation of a widening trend as we move towards $\Delta_{23}/2\pi = 0$ GHz.

5.2.1 Preliminary interpretation using numerical simulations

The experimental results were modeled to get an intuition about the dynamics we recorded. Figure 5.10(a) and (b) show the second-order correlations as a function of detuning from experiment and theory, respectively. In the numerical simulation we have neglected spectral diffusion to emphasize the effects of the coupling. The theoretical plot shows a bunching peak with exponential decay far from the crossing of the dipoles, whereas strong modification is observed for detunings $-0.5 \leq \Delta_{23}/2\pi \leq 0.5$ GHz. There the decay exhibits a bi-exponential behavior, with the maximal width for $\Delta_{23} = 0$ GHz. Further comparison between these 2D maps is not directly possible, due to noise in the experimental data.

The bi-exponential decay with a fast and a slow component can be seen

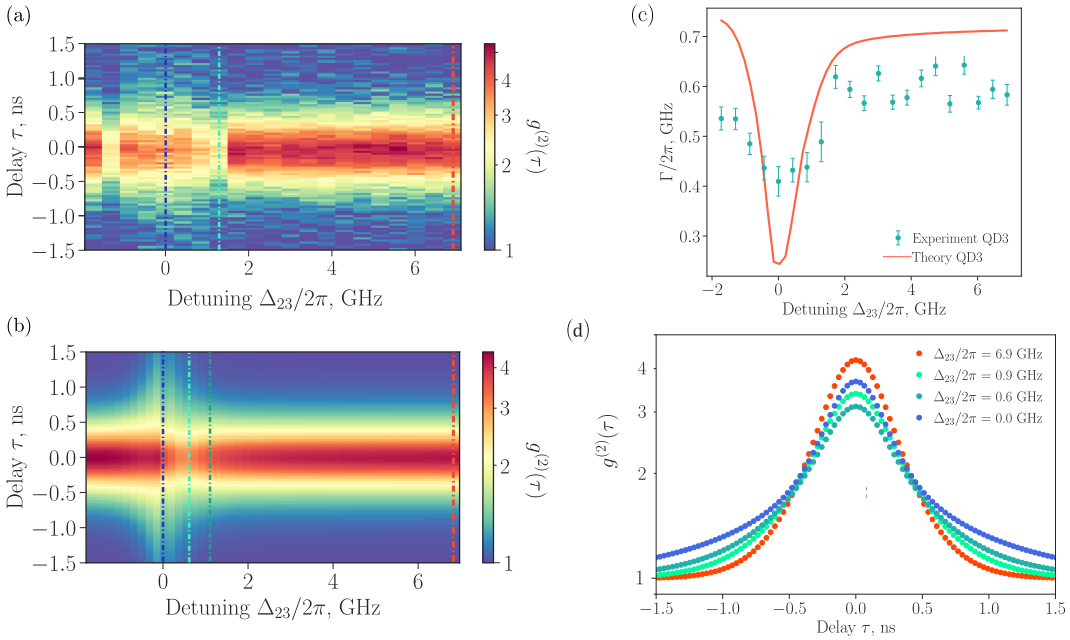

FIGURE 5.10: (a) Two-photon correlations, $g^{(2)}(\tau)$ in transmission mode of the nanostructure, as a function of the detuning, $\Delta_{23}/2\pi$, between two QDs. For each detuning the laser was set in resonance with QD2. (b) Theoretical simulation of (a), using the experimental parameters and neglecting spectral diffusion. (c) The decay rate of the second-order correlation bunching peak, as a function of the detuning between two QDs. The red curve traces the change of the decay rates as derived by the theoretical model. (d) Theoretical simulation of the experimental result shown in 5.9(b). The detunings shown are color-coded in (b).

more clearly in Figure 5.10(d), where four traces from (b) are plotted. Similar to a lifetime measurement, what is recorded in the $g^{(2)}(\tau)$ is the temporal profile of the photon emitted by the coupled system, with a super- and subradiant component, after the detection of a short-lived photon from the decay of $|ee\rangle$ to $|+\rangle$. The theoretical $g^{(2)}(\tau)$ traces were plotted for comparison with the experimental ones of 5.9(b), where apart from the broadening of the width close to $\Delta_{23} = 0$ GHz, owed to the decay of the subradiant state, no fast component is recorded experimentally. A valid argument about the lack of the fast decay from our data, is the limited time resolution of the detection system, as the time-jitter of the SNSPDs used here (200 ps FWHM) was larger than the superradiant decay times (~ 120 ps).

The fitted bunching widths of the experimental $g^{(2)}(\tau)$ for all detunings in Figure 5.10(a), are plotted in (c) (blue points). The widths at large detunings $\approx 0.6 \pm 0.02$ GHz are not compatible with the linewidth of QD3 found in Chapter 4, $\Gamma_3/2\pi = 0.73 \pm 0.02$ GHz. Accordingly, for detunings near resonance the fitted values give a linewidth of $\approx 0.43 \pm 0.02$ GHz which is far from the subradiant linewidth, $\Gamma_-/2\pi = 0.22 \pm 0.02$ GHz found for QD2-QD3. This discrepancy emphasizes the need for a more suitable fitting model. In the same plot we overlay the theoretical widths for the same scan of detunings (red line). These values were extracted by fitting all traces in

Figure 5.10(b) using a bi-exponential function convolved with a Gaussian. The plotted width is of the subradiant component of the decay, $\Gamma_-/2\pi$, to be consistent with the experimentally deducted linewidths. Theory and experiment follow the same trend, with the minimum width found at resonance. However, there is clear deviation in the value of the minima, as well as the range of detunings for which the bunching peak exhibits broadening. These differences are for now attributed to the nuclear spin dragging, inducing additional spectral diffusion, which is not included in the theoretical model.

5.3 Summary

In this Chapter, we demonstrated that the observation of photon coincidences at zero-time delay in second-order intensity correlations from two emitters, can be a proof of photon-mediated coupling, directly associated to superradiance in the case where only a single emitter is driven. The system was initially explored using coherent and continuous drive in resonance fluorescence. We observed an anti-dip at $g^{(2)}(0)$ from the decay through the two-step Dicke ladder, via the superradiant state, as well as broadening of the single emitter dip, that was associated with direct emission from the subradiant state.

Numerical simulations confirmed that observing photon coincidences at zero-time delay with single-emitter excitation is only possible when the emitters are coupled. It was also suggested that the presence of the anti-dip can reveal the type of coupling, based on the photon coincidences from both sides of the PCW. Further, the factors preventing the observation of a bunching peak in resonance fluorescence were discussed. We specifically provided insights through simulations of the effects of pure dephasing and driving power on $g^{(2)}(\tau)$.

Lastly, we investigated photon coincidences in resonance transmission, where preliminary analysis showed modifications of the bunching peak that align with those of the decay rate from the collective emission.

6 Conclusion and Outlook

6.1 Summarizing and reflecting

In the present work we demonstrated photon-mediated coupling between different pairs of QDs, embedded in a nanophotonic waveguide. Direct signatures of super- and subradiant emission dynamics were observed through the modification of the lifetimes when the emitters were tuned to resonance. The demonstration of the coupling extended beyond the subwavelength limit, facilitated by the nanophotonic environment of the PCW, providing broadband spectral operation and long-range coherent interaction between the QDs. The coupling was also observed in second-order intensity correlations, $g^{(2)}(\tau)$, where, by driving a single emitter, we ensured that the emerging features in the $g^{(2)}(\tau)$ are unambiguously associated with super- and subradiance from the waveguide-mediated coupling. This observation was of fundamental scientific interest for the platform, as the demonstration of dipole-dipole coupling lays the groundwork for harnessing multiple QDs for applications in quantum communication and quantum information processing.

Coupling multiple emitters requires spectral and spatial proximity between them, as well as a highly coherent light-matter interface. As these requirements are not easy to fulfill with self-assembled QDs, due to the spectral and spatial inhomogeneities inherent to the growth process, we initially focused on the spectroscopic investigation of the sample.

Owing to the high density of the sample [85], by performing transmission measurements on different PCWs we could find at least two QDs spectrally close and well coupled to the waveguide mode in one out of three nanostructures. The one that was selected contained three QDs, all close to the band-edge of the PCW, particularly favorable for probing the coupling between the QDs. That is because, on the band-edge, the high LDOS enhances the radiative decay rate Γ of the QDs [47], making them less susceptible to fast noise from elastic phonon scattering, inducing pure dephasing. In turn, this improves the likelihood that the pair of dipoles will remain on resonance for the entirety of the measurement, and the coherence needed to observe the coupling effects, will be preserved. In addition to that, a bias voltage, applied across the sample through the p-i-n diode, limits the electronic noise from the environment, inducing spectral diffusion to the emitters.

The three QDs were selected for their high coupling to the waveguide mode, indicated by the depth of the RT dips of the transmission measurement. This suggests that the QDs are positioned at specific locations within

a unit cell of the PCW, resulting in approximately equidistant separations between the adjacent pairs, $|x_{mn}|$. Since their spatial separation defines the type of coupling, this argument was later used to explain why all three pairs of coupled dipoles exhibit the same dissipative character.

With the current device, independent tuning of the QDs was not feasible, limiting the possibility of tuning multiple emitters into resonance. Alternatively, a homogeneous out-of-plane magnetic field, B_z was used as the tuning parameter for the frequencies of the QDs. That, induced opposite energy shifts to the two dipoles of each QD, resulting in the crossing of opposite circularly polarized dipoles, $\sigma_{\pm}$, of different QD pairs. Naturally, the two opposite polarized dipoles would not be able to interact. However, as the QDs are embedded and well-coupled to their nanostructure, the dipole-dipole interaction is mediated by the shared mode of the waveguide. Essentially, the emitters interact with each other through a photon exchange between the projection of their dipoles to the local polarization of the waveguide mode.

While coupling opposite dipoles might initially appear as a limitation to the experiment, in the current structure it proved advantageous, enabling independent or simultaneous driving of the coupled pair with a single excitation beam. Specifically, since the adjacent coupled emitters are positioned $\sim 1\mu$m apart, the diffraction-limited beam spot would address both at the same time from the top of the waveguide. Then, by choosing the polarization of the driving beam with the waveplates in the excitation path, we could either fully suppress one of the dipoles and still drive efficiently the other, for single-emitter excitation, or address both dipoles, for double excitation. The latter enabled preparation of the collective state from a single excitation beam.

The coupling between the pairs of dipoles was investigated through lifetime measurements. This approach was selected over the second-order intensity correlations used in previous studies [51, 52], which has been debated for its ambiguity in providing exclusive proof of superradiant emission from the coupled system [54, 55]. By driving a single emitter of a pair and sweeping the detuning between them, we recorded the anticipated modification of the lifetime. From initially exhibiting a single exponential behavior in the far off-resonance case, resulting in radiative linewidths of $\Gamma_2/2\pi = 0.79$ GHz and $\Gamma_3/2\pi = 0.73$ GHz for one of the pairs, the time-resolved dynamics transitioned to a bi-exponential profile when the dipoles were tuned to resonance. This included a superradiant component with $\Gamma_+/2\pi = 1.33$ GHz and a subrandiant with $\Gamma_-/2\pi = 0.22$ GHz.

The strength of coupling, quantified by the ratio between the two components of the decay Γ_+/Γ_-, was found by fitting to be below 5 for the three pairs. The coupling strength is is limited by a combination of imperfections and decoherences from the system. In particular, the uneven decay rates of the emitters $\Gamma_{m,n}$, any deviation of the coupling phase from the dissipative $\phi_{mn} = N\pi$ limit, the imperfect β-factors, the spectral diffusion and pure dephasing from the environment, as well as the losses in the waveguide, contribute to the reduction of the coupling. Optimizations to the coupling

strength can be made by improving the condition of the sample or calibrating the excitation scheme. We elaborate more on that at the Outlook below.

Looking into the lifetime measurements from the two ports of the PCW, the symmetry in the intensities signifies an inter-emitter separation that corresponds to a coupling phase of $\phi_{mn} \approx N\pi$. By the definition of the coupling rates, $\Gamma_{mn} \propto \cos\phi_{mn}$ and $J_{mn} \propto \sin\phi_{mn}$, this separation determines a predominantly dissipative coupling ($J_{mn} \approx 0$) between the emitters. This was further supported by the estimation of ϕ_{mn} from numerical simulations of the experiment, giving $\phi_{mn} = 0.03 - 0.05$ rad.

The theory developed for the present experiment [57] was used to explain the mechanisms that lead to the coherent evolution of the system. It specifically revealed that in the dissipative coupling regime the coherent dynamics result from an interplay of the detuning among the two coupled emitters, $\Delta_{mn}/2\pi$, inducing population exchange between the super- and subradiant states, and their dissipation, $\Gamma_{mn}/2\pi$, to the collective ground state.

Obtaining understanding over our system, we aimed at preparing the collective state on demand. For that, both emitters should be driven simultaneously, with a well-controlled relative driving phase θ. The first approach that was considered was to use a spatial light modulator (SLM) to diffract a single beam into two. With that, we could drive each QD individually with a driving phase, $\theta_{m,n}$, defined by the displacement of the diffraction pattern on the SLM screen. This method would have been robust to phase drifts between the two beam spots, as they both originate from the same laser and reach the sample following the same path. Yet, it proved sub-optimal for our system, as the proximity of the adjacent pairs led to the overlap of the two beam spots. Consequently, the resulting interference posed challenges in controlling the relative driving phase.

Exploiting the opposite polarizations of the coupling dipoles, we used the polarization of the single excitation beam to introduce the relative driving phase to the emitters. As the waveplates in the excitation path were not mapped to the excitation power and driving phase, this first attempt led to the population of $|e_m g_n\rangle + i\,|g_m e_n\rangle$ where $\theta = -\pi/2$. Instead, $\theta = 0$ and π are needed to populate the super- and subradiant states, respectively. This implies that a full mapping of the excitation waveplates to the relative driving phase and power is required to control the collective excitation.

Though, even with this control, the present excitation scheme would prepare a product state $(|e_m\rangle + |g_m\rangle) \bigotimes (e^{i\theta}\,|e_n\rangle + |g_n\rangle)$, resulting to a maximum population of 50% in the super- and subradiant states. A proposal for increased population of the subradiant state and improved fidelity of the preparation has been suggested [27, 78] and considered for our system. Let us elaborate a bit on that in the Outlook section below.

Finally, the coupled emitters were examined using second-order intensity correlations $g^{(2)}(\tau)$, under continuous driving. Unlike previous works with QDs [51, 52, 54], we drove a single emitter of a pair, eliminating the possibility of any collective feature emerging due to measurement-induced

cooperativity. When the emitters are on resonance with each other, the photon coincidences revealed an anti-dip at zero time delay, $g^{(2)}(0)$. This feature arises from the decay of the doubly excited state, $|e_m e_n\rangle$, to the superradiant, $|+\rangle$, and subsequently to the collective ground state, $|g_m g_n\rangle$, along the two-emitter Dicke ladder. The experimental anti-dip we observed reached a maximum of $g^{(2)}(0) = 0.94$, while simulations for ideal conditions exhibited clear bunching at zero time delay, $g^{(2)}(0) > 1$. We therefore note that the maximum of the anti-dip is reduced due to imperfections and decoherences of the system, similar to the coupling strength ratio Γ_+/Γ_-, and the driving power that we used to perform the experiment. Modeling of the anti-dip with a convolved function of a two-sided exponential with the instrument response function (IRF) revealed a linewidth of $\Gamma_{adip}/2\pi = 1.44 \pm 0.16$ GHz. Comparing it to the superradiant linewidth extracted from the lifetime measurements $\Gamma_+/2\pi = 1.33$ GHz, we find the two to be in good agreement, verifying the interpretation that the anti-dip emerges from the decay of the superradiant state.

In addition, we observed broadening of the width of the single-emitter dip when the QDs were tuned to resonance, a feature that was not present in the previous works. For $|\tau| \geq 0.4$ ns then, $g^{(2)}(\tau)$ could be modeled with a standard RF dip of linewidth $\Gamma_{dip}/2\pi = 0.31 \pm 0.03$ GHz. This approximates the subradiant linewidth $\Gamma_-/2\pi = 0.22$ GHz, implying that the broadening of the dip at longer delay times stems from the decay of the longer-lived subradiant state, $|-\rangle$ to $|g_m g_n\rangle$.

Preliminary analysis and simulations showed that, under this excitation scheme where a single emitter is driven, the presence of the anti-dip and the broadening of the dip can exclusively indicate dissipative coupling between the QDs. However, further investigation revealed that, to certify the type of coupling, photon coincidences from both ports of the PCW are required, similar to the case of the lifetime measurements.

The sensitivity of these collective features to imperfections and decoherences of the system was emphasized when $g^{(2)}(\tau)$ measurements were repeated while driving the less noisy emitter of the pair. In this case, the anti-dip was barely emerging in the photon coincidences from one of the ports of the PCW. The absence of collective features is attributed to the spectral diffusion of the non-driven noisy dipole, making it challenging for the two to remain in resonance throughout the measurement.

Closing, our work marks the first demonstration of dipole-dipole photon-mediated coupling between solid-state quantum dots separated by multiple wavelengths, within a nanophotonic waveguide. Super- and subradiant coherent dynamics of the coupled system were directly observed in the lifetime measurements, and a proof-of-principle preparation of the collective state was realized. We further probed the second-order intensity correlations of the coupled system. Adding to previous investigations [54, 55], we suggest that the emerging anti-dip at zero time delay can be an exclusive signature of superradiance, when only a single emitter is driven. Our findings constitute fundamental research, aiming to serve as the stepping stone

towards multi-emitter applications in quantum technology on-chip.

6.2 Outlook

The understanding and control we obtained over the coupled system of two quantum emitters are foundational steps towards applications in quantum communication networks [32, 33] and photonic quantum computing [26]. Scaling up to multiple QDs opens the door to applications with non-linear optics [115], quantum memories with exponential improvement in photon storage [34], the implementation of photon-photon quantum gates [116], as well as the preparation of multi-photon states for enhanced quantum-metrology [71].

To advance towards these applications, there is considerable room for improving the coupling conditions, exploring strategies for scaling up to multiple emitters, and undertaking various steps to realize photonic cluster states with our coupled QDs [26]. In this context, we discuss below a few consideration that should be taken into account for our system.

6.2.1 Improving the coupling strength

As mentioned previously, the observed coupling strength defined by Γ_+/Γ_- is restricted by different imperfections of the system. Specifically, the uneven decay rates $\Gamma_{m,n}$ of the emitters and arbitrary coupling phase ϕ_{mn}, the imperfect β-factors, and decoherence from the solid-state environment, such as spectral diffusion and pure dephasing, along with the waveguide losses, contribute jointly to mitigating the effects of the coupling.

To address these imperfections, we can explore optimizations to our methodology and system. The non-unity β-factors can be improved with optimally-positioned QDs within the waveguide. This could be achieved through the deterministic fabrication of nanostructures around pre-localized QDs, as it has been demonstrated before [98, 117]. The spectral diffusion, induced by charge noise from material impurities and free charges in the p- and n-doped regions, could be reduced by employing higher-quality materials and improving the quality of the p-i-n gate. To tackle the fast source of decoherence, namely the pure dephasing due to phonon noise from the environment, would require Purcell enhancement of the spontaneous decay rate of the emitters and the use of stronger cooling systems, operating at mK temperatures. Finally, the losses in the waveguide which restrict the spatial range of the coupling, are measured to be 7 dB/mm and attributed to scattering losses due to the sidewall roughness [85]. The currently proposed method to address this fabrication imperfection involves the re-flow of an electron-sensitive resist, that would smooth out the sidewalls [118]. Another parameter that can impact the coupling strength is the driving pulse duration. Specifically, calibrating the excitation beam to obtain a long but weak drive over the emitters, is expected to improve the coupling. We delve into the latter in more detail in Section 6.2.3 below.

6.2.2 Scaling-up to multiple coupled quantum dots

Up to now, when considering scaling up to multiple QDs, we have been relying on their moderate density and the broadband nanostructures [97]. However, in the limited amount of PCWs that were tested for this thesis, the number of well-coupled QDs within the same waveguide did not exceed three. Consequently, to investigate protocols requiring many-body systems [34, 116], deterministic positioning of nanostructures appears to be imperative [98, 117].

The second challenge in scaling up our platform for multi-emitter coupling, comes with the inhomogeneous broadening in the emission frequency of the QDs, imposing the need for individual tuning. To tune more emitters into resonance, a novel device allowing simultaneous and independent control of different regions of the waveguide, has been under examination [104]. Figure 6.1 shows the present design of a nanostructure containing individual electrodes for DC-Stark tuning of the different QDs, with a trench etched across the PCW to electrically isolate the two sides. This will ensure independent electrical control over the two parts of the nanostructure.

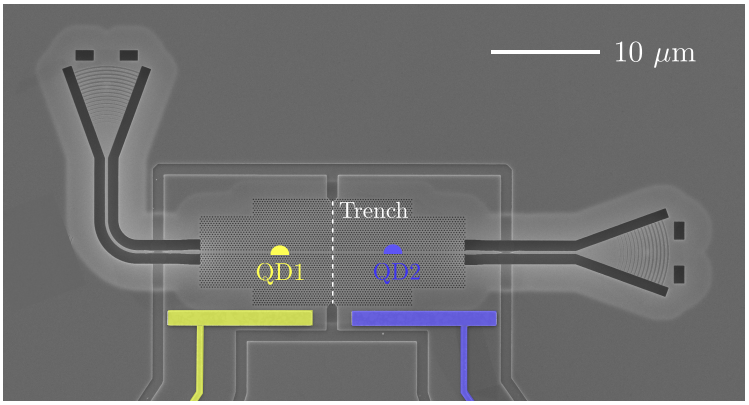

FIGURE 6.1: SEM image of the new generation trenched PCW. The trench in the middle (white dashed line) electrically isolates the two sides of the waveguide. The electrodes on each side (yellow and blue), color-coded to the QDs, are used for independent electrical tuning of their emission frequencies.

Finally, another parameter that can hinder the up-scaling of coupled emitters is the disparate noise from charge carriers, that would be shifting the emitters off resonance. This can be mitigated through active feedback to the DC-voltage applied to the QDs [119].

6.2.3 Towards the generation of photonic cluster states from two coupled quantum dots

As a final consideration for our coupled system of two QDs, we now shift the focus on the steps towards achieving deterministic generation of advanced photonic cluster states, for measurement-based quantum computing protocols.

To generate highly-entangled multi-photon states with our platform, we need to realize spin-spin entanglement between different emitters. This can be achieved by exploiting the waveguide-mediated dissipative coupling [78, 120]. The reason we consider spins rather than neutral excitons is that the former constitutes a more stable matter qubit, retaining its quantum coherence over much longer timescales, and can be as well coherently manipulated [19]. However, before proceeding to introduce spins to our system, the immediate step following our experimental work is to obtain control over the generation of entanglement between the two QDs.

6.2.3.1 Generating dipole-dipole entanglement on demand

Recently, collective excitation to super- and subradiant states from two ports on the sidewall of a waveguide was realized with superconducting qubits [46]. To populate the collective states on demand with our system, the current excitation scheme with the single beam should be further calibrated and optimized.

For the calibration, the driving power of the two emitters and relative driving phase θ should be well controlled. Given the opposite polarization and close proximity of the crossing dipoles, we propose to employ the collective excitation scheme by a single beam discussed in Section 4.4. To this, we now need to incorporate well-controlled polarization of the excitation beam, for a well-defined relative driving phase θ. This can be implemented by direct detailed mapping of the excitation quarter and half waveplates to a relative driving power and phase θ between the two QDs[1]. The above method has already yielded successful outcomes [109], where lifetime measurements for a continuous scanning of θ between 0 and π, showed clear transition from a fast decay of the superradiant state $|+\rangle$, to a long-lived of the subradiant $|-\rangle$.

To extend the collective excitation to any pair of emitters with larger spatial separation and with even parallel polarizations, the SLM becomes once more appealing. By programming a pattern on the SLM, the shape, amplitude and phase of the beam can be manipulated according to the needs of the excitation.

As mentioned previously, even with a well-defined relative phase, the excitation scheme used in Section 4.4 can maximally populate the addressed super- or subradiant state by 50%, while the other half is shared between $|g_m g_n\rangle$ and $|e_m e_n\rangle$. To prepare deterministically an entangled state with increased population, the collective excitation scheme has to be modified. For this purpose, we will exploit the waveguide-mediated dissipative coupling between the two QDs [78, 120], which results into different decay times for the super- and subradiant states. This difference essentially implies that it is easier to pump in the subradiant state than out of it with a calibrated pulse duration, which would lead to increased population in the subradiant state.

[1]Note that individual calibration for each emitter is required for every position of a beam spot, as the local polarization of the PCW dictates the optimal excitation conditions.

To maximize the selective population of the subradiant state, we need to apply collective driving to the system, with a relative driving phase of $\theta = \pi$ and a pulse duration in the order of few hundreds of ps for our QDs ($\Omega \sim \Gamma_- \ll \Gamma_+$)[2]. Experimentally, the pulse length can be controlled using a CW laser and an electro-optic modulator (EOM) with a pulse generator. With this dissipative generation of entanglement, a state fidelity of $F_{|-\rangle} = \langle -|\,\rho\,|-\rangle \sim 1 - \Gamma_-/\Gamma_+$ is possible [78]. From here, it becomes clear that for a deterministic generation of entanglement ($F_{|-\rangle} > 0.5$), the coupling strength should be $\Gamma_+/\Gamma_- > 2$, a requirement that is well-satisfied by our current system of QDs.

To characterize the entanglement, a protocol that was used before for distant atomic ensembles can be employed [121]. This requires a quantum state tomography for the single excitation subspace[3] to lower-bound the concurrence[4], together with photon coincidence measurements to verify negligible population in the doubly excited state.

6.2.3.2 Independent spin-spin tuning

The next step towards generating large-scale multi-photon states, involves introducing spin to each of the two entangled QDs and establishing spin-photon entanglement for each one. A single spin in a QD can be implemented by adding a charge carrier in its potential well. This can be done either by bringing in an electron to the conduction band, or removing one from the valance band, leaving a hole behind. Experimentally this can be done by applying a bias voltage across the p-i-n diode of the sample. This might cause the energy levels of the conduction band to shift down, below the fixed Fermi level E_f, allowing an electron to tunnel in the QD from the back contact.

For spin-spin entanglement there are two requirements we need to satisfy: (1) individual control over the optical transitions to tune the QDs to resonance and (2) independent spin control. For the first, the new generation of trenched devices (Figure 6.1) for independent electrical tuning of the optical transitions is under development. Considering the independent spin control, we can learn from the recently demonstrated generation of spin-photon entanglement with our platform [122]. This requires both coherent spin control and optical cyclicity[5] from the emitter. The spin control can be enabled by an in-plane magnetic field (Voigt configuration) that will Zeeman-split the spin-up and -down states, allowing for all-optical spin manipulation. The required cyclicity in the optical transitions has been demonstrated to be induced in Voigt configuration by the PCW [123]. Finally, as we want to

[2]The exact duration required depends on the coupled system and needs to be calibrated for each pair individually.

[3]For the read-out of the subradiant state, an off-resonant, high power short pulse should be applied on the system. This would cause an AC-Stark shift that would introduce a phase and transfer the population to the superradiant state. From there the system would decay fast and the emission would be finally detected.

[4]Concurrence C, is a qualitative measure of entanglement. If C > 0 the system is entangled.

[5]High probability of decaying back to the initial spin state.

implement independent spin control over the two emitters, a second optical excitation path should be installed in the current optical setup.

Obtaining the above described toolbox would allow the generation of spin-spin entanglement in our QD system. A potential protocol developed for this purpose for ultracold atoms in nanoplasmonic lattices [27], uses the collective excitation scheme discussed in Section 6.2.3.1. There the driving to the subradiant state is combined with a mixing of the symmetric (triplet) states, to ensure that the subradiant (singlet) is a unique steady state.

Achieving spin-spin entanglement with QDs would pave the way for generating complex cluster states [26] as a universal resource for measurement-based quantum computing on chip. The steps towards this milestone are discussed almost philosophically above. There is no doubt that it will take great effort and persistence to realize a large-scale multi-photon entanglement source with our platform. From advancing the state-of-the-art nanostructures and pushing the limits of our current experimental conditions, to refining the pulse driving sequences, there are numerous challenges to undertake towards this goal. Though, often enough in physics, challenge is all it takes to keep moving forward.

A Power tuning

The resonant emission frequency of a QD is dependent on the power used to excite it. In the figure A1 the transmission counts of QD2 are shown as a function of voltage and excitation power. The frequency of the emission appears to be shifting to larger values with increasing power. For this, a CW laser was sent through the waveguide from Port 2 and the collected photons from Port 1 were detected by an APD.

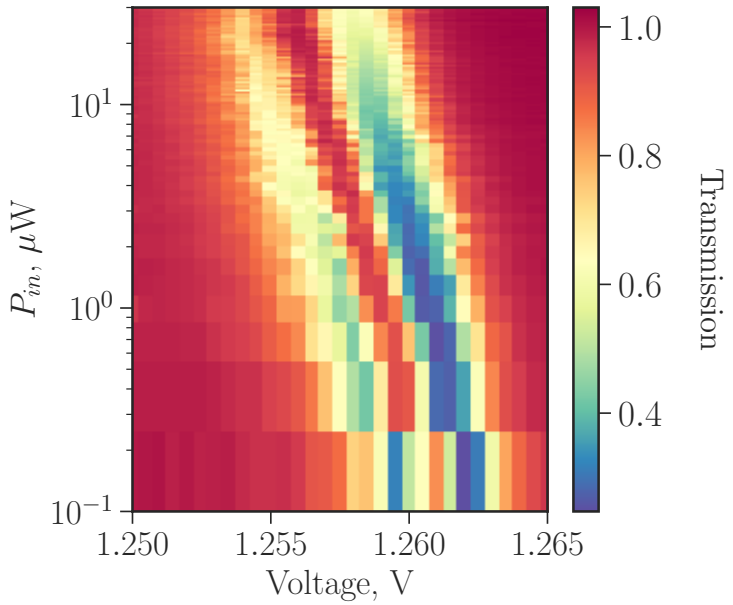

FIGURE A1: Transmission measurement, tracing the power-tuning of QD2 as a function of voltage.

B Decay dynamics with excitation through higher-energy states

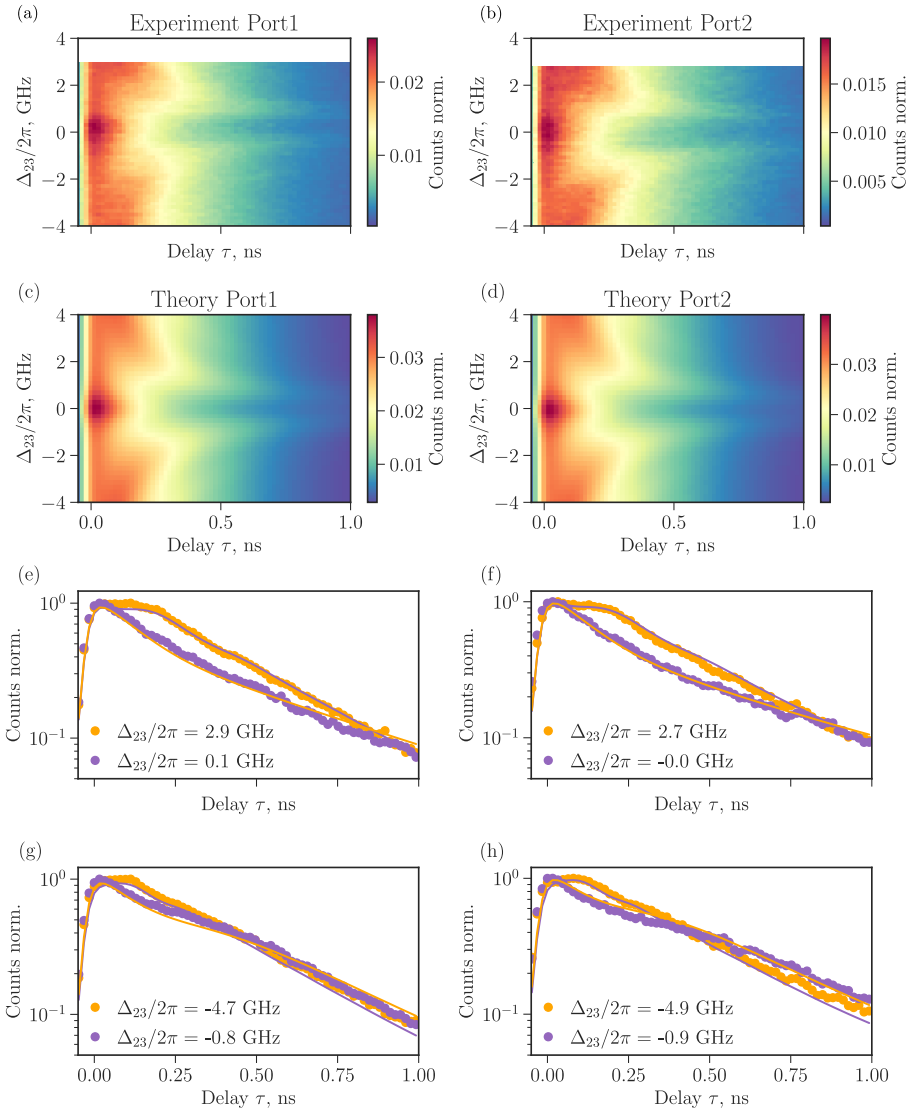

FIGURE B1: Decay dynamics with excitation through higher-energy states of QD3 for different detunings with QD2 around their resonance at 1.067T. (a) Experimental data of the time-resolved decay dynamics while driving QD3, for a complete scan of detunings, Δ_{23}, with collection from Port 1 and (b) Port 2. Each time-trace is normalized to the sum of the counts in that trace. (c) and (d) Theoretical calculation of the experiment by the developed theory, using the parameters from Table 4.1. (e-h) Individual time-traces of the decay dynamics for different detunings Δ_{23}. We observe additional modulation on top of the decay for large Δ_{23} (orange), owed to the exchange of population between the super- and subradiant states. The time-traces close to the on-resonance condition, $\Delta_{23}/2\pi = 0$, consist of two components corresponding to super- and subradiant emission. The solid lines are fits to the decays using the parameters included in Table 4.1.

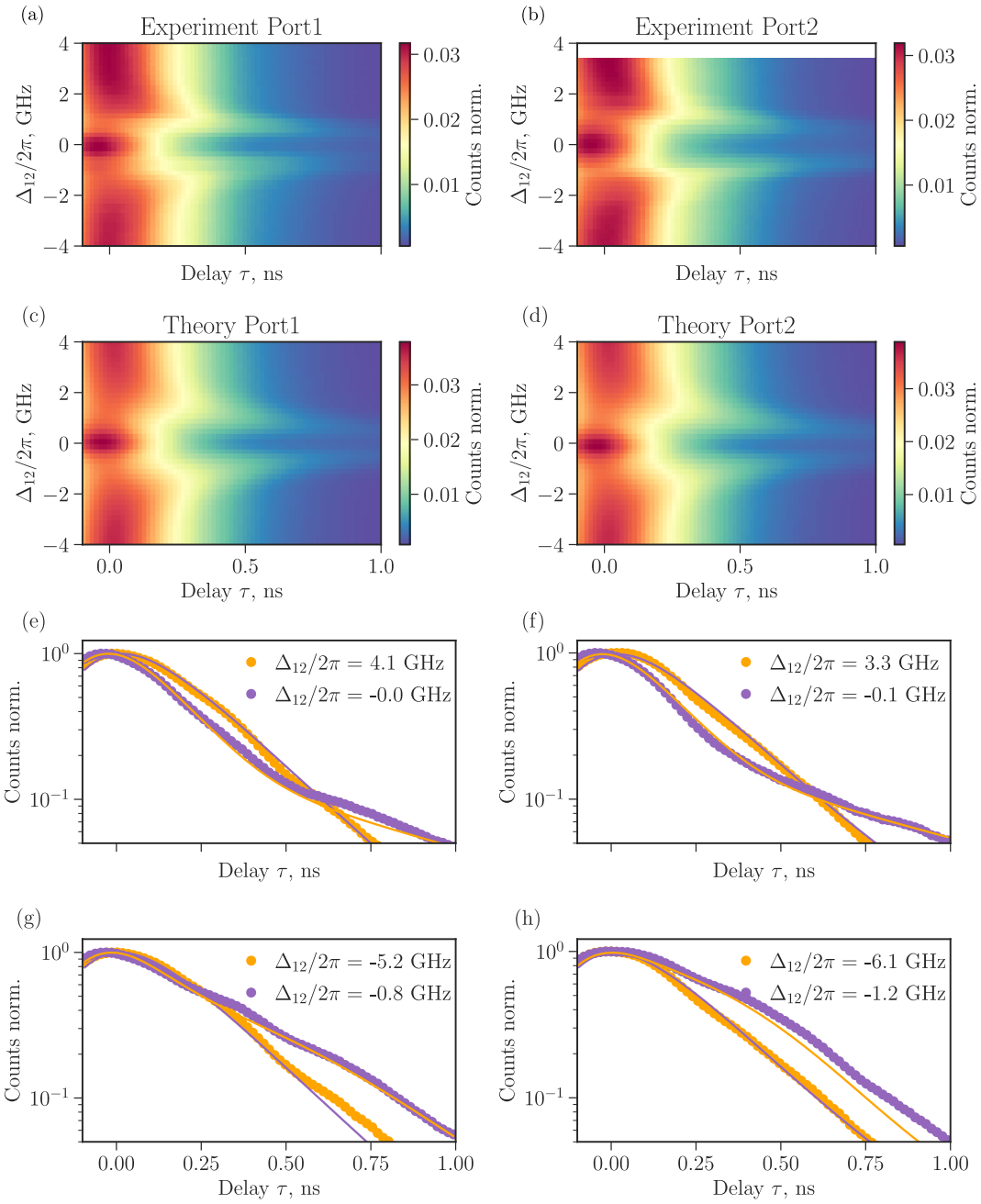

FIGURE B2: The same experiment as in figure B1 realized for driving QD2 while varying the detuning to QD1, around their resonance at 2.13 T.

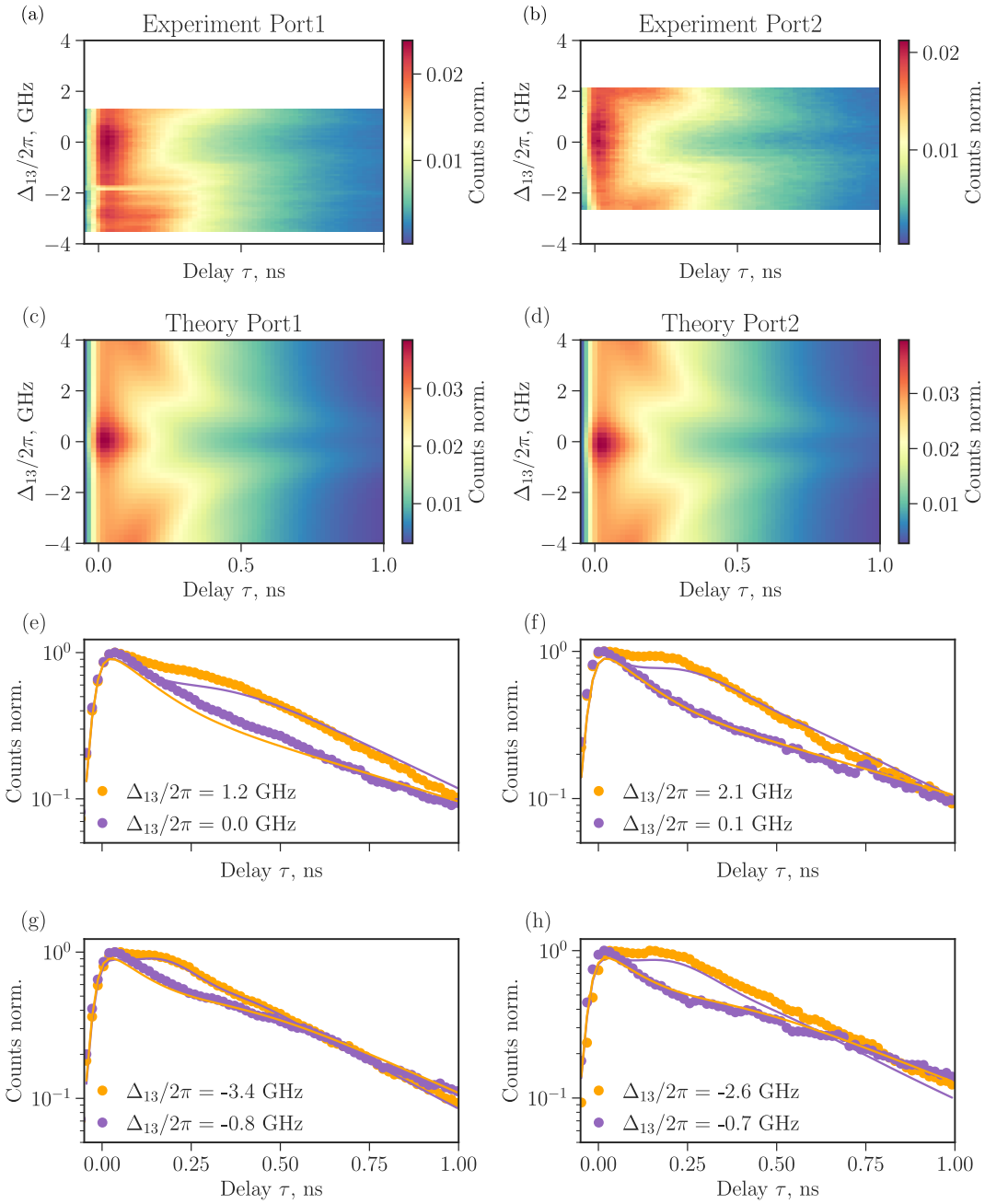

FIGURE B3: The same experiment as in figure B2 realized for driving QD1 while varying the detuning to QD3, around their resonance at 3.33T.

C Decay dynamics with resonant excitation

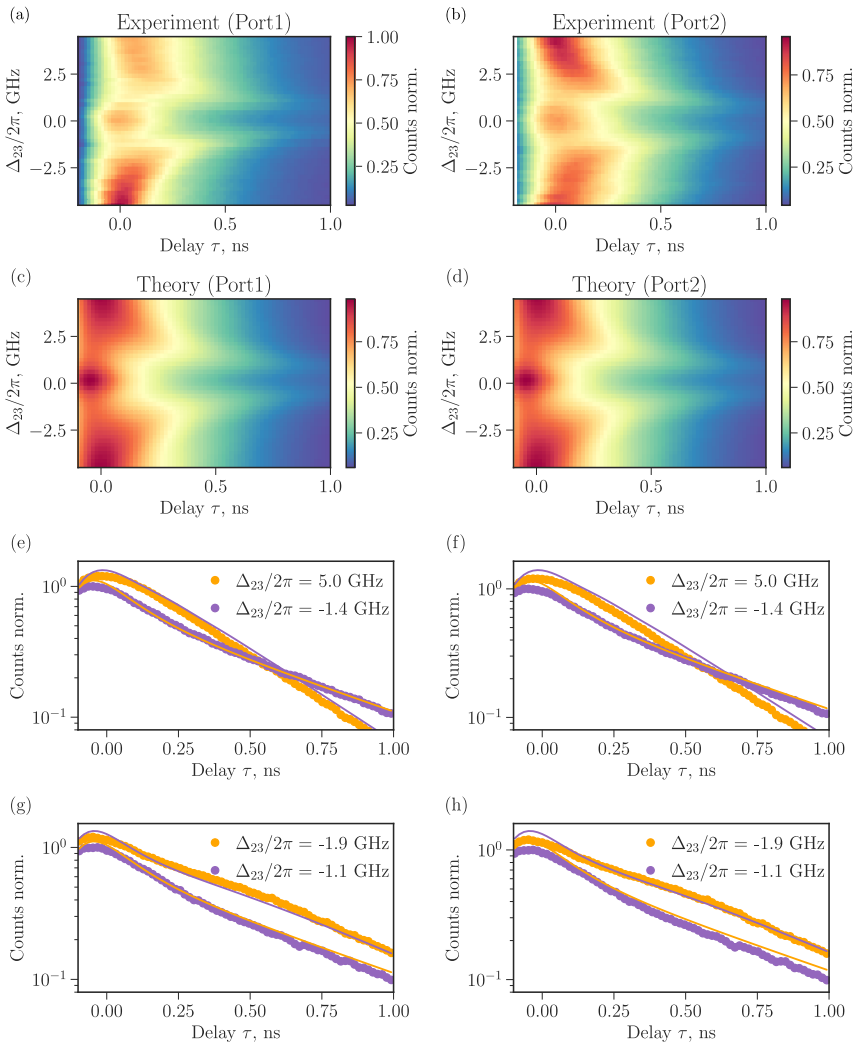

FIGURE C1: Decay dynamics with resonant excitation of QD3 for different detunings with QD2 around their resonance at 1.067T. (a) Experimental data of the time-resolved decay dynamics while driving QD3, for a complete scan of detunings, Δ_{23}, with collection from Port 1 and (b) Port 2. Each time-trace is normalized to the sum of the counts in that trace. (c) and (d) Theoretical calculation of the experiment by the developed theory, using the parameters from Table 4.1. (e-h) Individual time-traces of the decay dynamics for different detunings Δ_{23}. We observe additional modulation on top of the decay for large Δ_{23} (orange), owed to the exchange of population between the super- and subradiant states. The time-traces close to the on-resonance condition, $\Delta_{23}/2\pi = 0$, consist of two components corresponding to super- and subradiant emission. The solid lines are fits to the decays using the parameters included in Table 4.1.

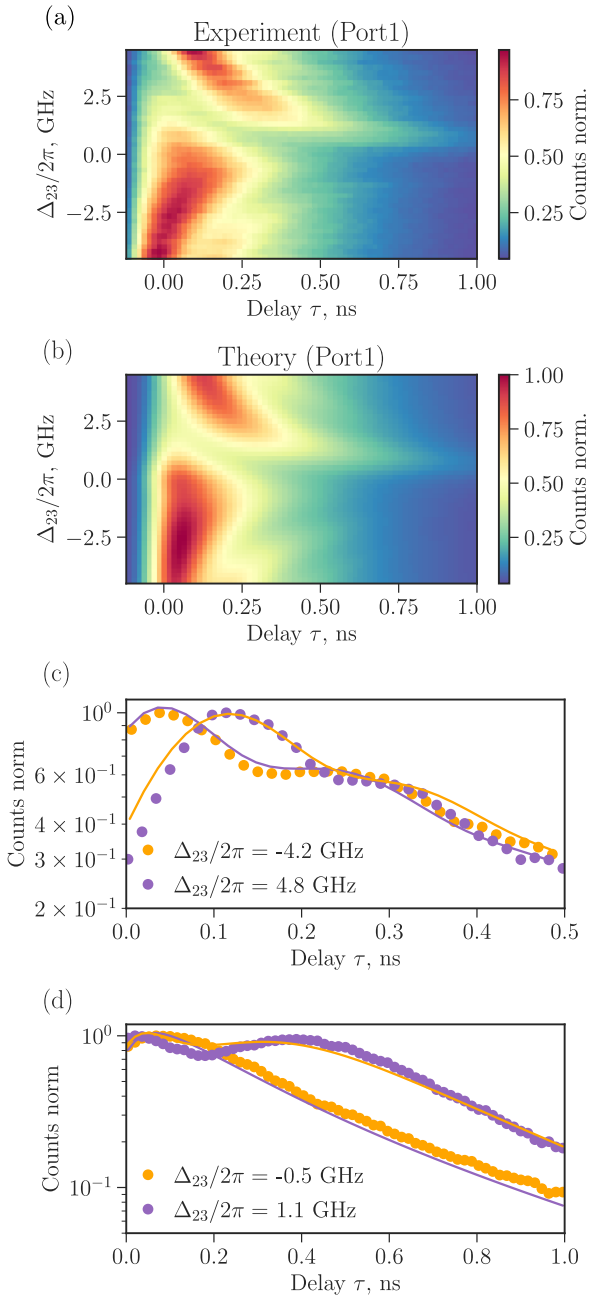

FIGURE C2: Decay dynamics with resonant excitation of both QD2 and QD3 around their resonance at 1.067T. (a) Experimental data of the time-resolved dynamics while driving QD2-QD3, for a complete scan of the detuning between them, while collecting from Port 1. (b) The theoretical calculation of the experiment by the developed theory. (c-d) Individual time-traces of the decay dynamics for different detunings Δ_{23}. The solid lines are fits to the decays using the parameters in table 4.1 and the extracted Rabi frequencies $\Omega_{2,3}$ and relative driving phase θ, as included in the main text (see section 4.4).

D Photon coincidences driving the less noisy emitter

Repeating the same experiment by driving QD2 this time, and suppressing QD3 with the excitation waveplates, the second order correlations revealed only a single dip at all detunings (Figure D1(b)), while the resonance fluorescence measurement (D1(a)) also did not show the prominent decrease in counts at the crossing point, as in Figure 5.3(a).

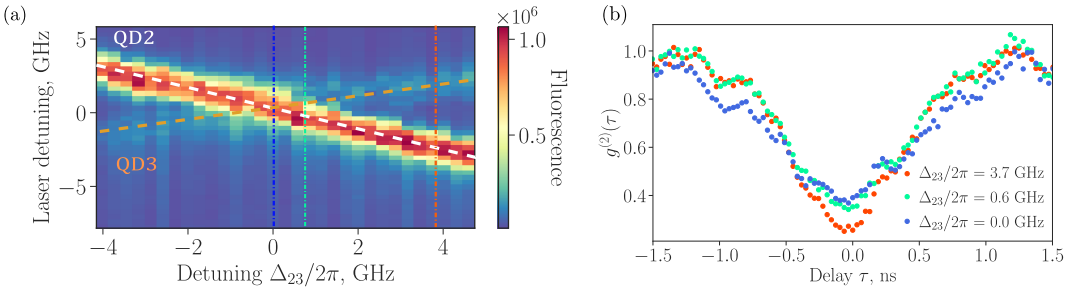

FIGURE D1: Collection from Port 1. (a) Resonance fluorescence of the neutral exciton of QD2, as a function of the detuning between the two crossing dipoles QD2-QD3, while collecting from Port 1. The white dashed line traces the expected spectral emission from QD3, whose excitation is prohibited by the polarization of the laser. (b) Two-photon correlations $g^{(2)}(\tau)$ for three detunings, color-coded with the dot-dashed vertical lines in (a).

One hypothesis that could explain this outcome, is based on how the two different dipoles are experiencing the semiconductor environment. From Figure 3.5 it becomes apparent that the low frequency dipole of QD3 is more “noisy" than the high frequency dipole of QD2. This could potentially be explained by spectral diffusion. For long-scale measurements ($> 1s$) this decoherence process can affect the result, as the resonance frequency of QD3 will be shifting in time around the original value, making it more difficult to bring the two dipoles on resonance with each other. However, when exciting QD3, the beam spot focused on top of the QD position, will dictate the charge environment, keeping it more stable. This then should decrease spectral diffusion, enabling us to have the crossing dipoles on resonance for longer, and observe the effects of their coupling more pronounced than in the opposite case.

Aiming to investigate further, the experiment was conducted again, using the other collection port (Port 2), for which a weak anti-dip feature was present at zero-time delay (Figure D2(b)).

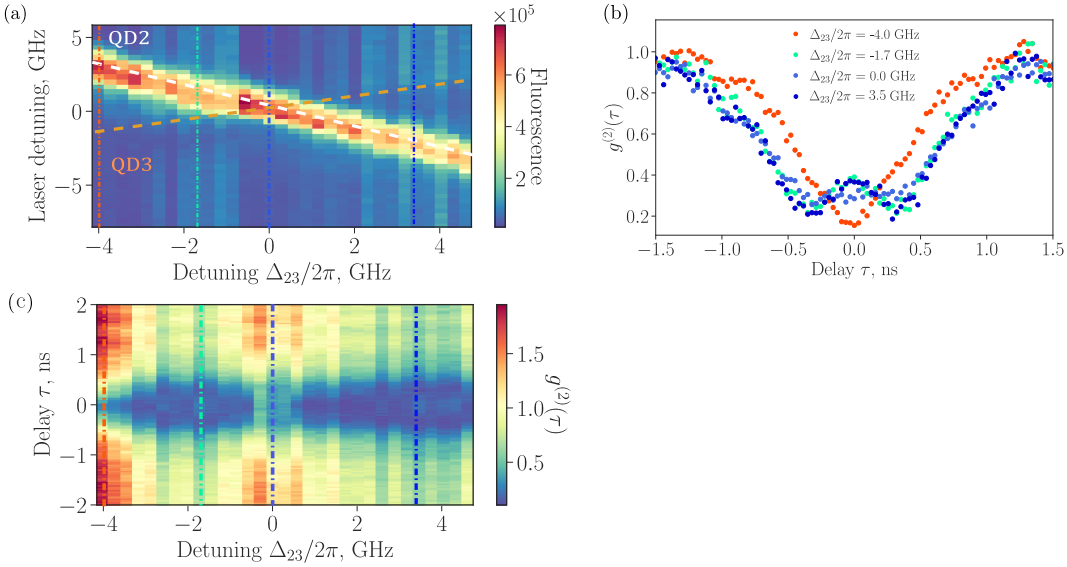

FIGURE D2: Collection from Port 2. (a) Resonance fluorescence of the neutral exciton of QD2, as a function of the detuning between the two crossing dipoles QD2-QD3, while collecting from Port 1. The white dashed line traces the expected spectral emission from QD3, whose excitation is prohibited by the polarization of the laser. (b) Two-photon correlations $g^{(2)}(\tau)$ for three detunings, color-coded with the dot-dashed vertical lines in (a).

E Preliminary characterization of the spatial light modulator (SLM)

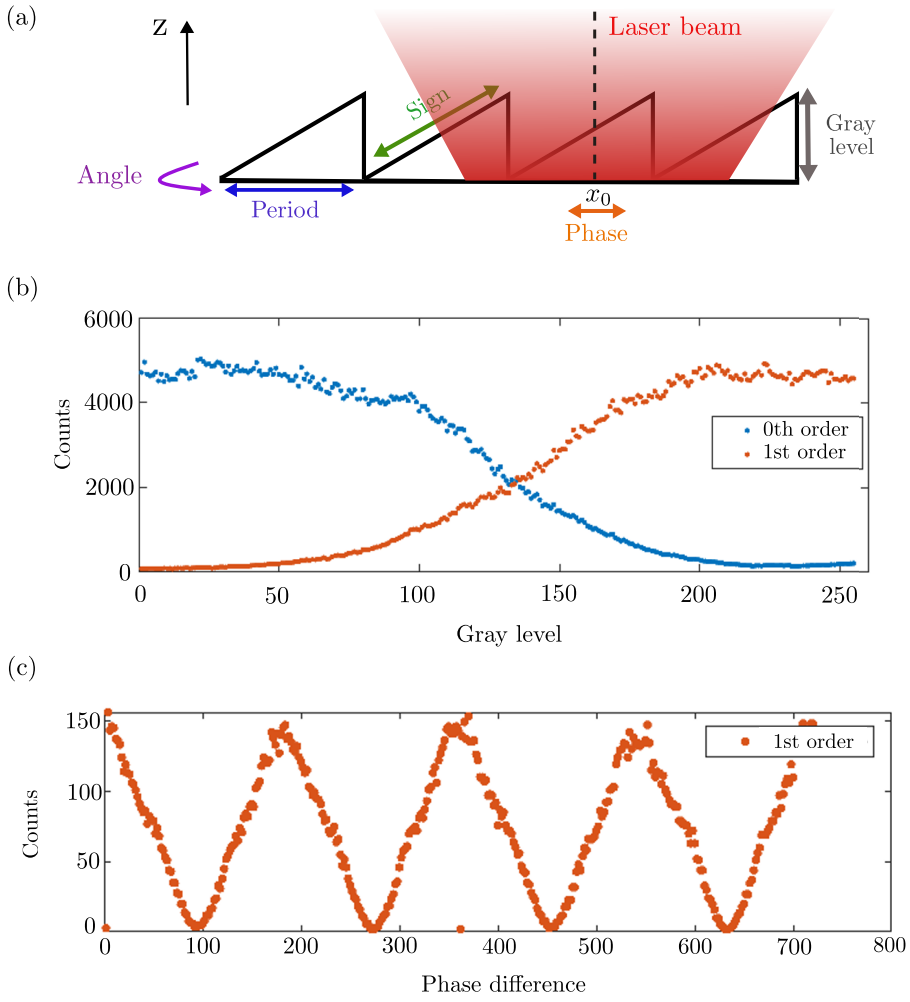

FIGURE E1: (a) Blazed grating pattern. By programming the pattern on the SLM screen, the period (spacing between the subsequent blazes of the grating), sign (orientation), angle around z, gray level (amplitude of grating) and phase (added by the relative position x_0 of the grating pattern with respect to the beam spot) can be controlled. (b) Intensity of the 0th and 1st diffracted order, for period 13.5 and phase 0 (as defined in: M_SLM). The beam spot continuously transitions from being only reflected on the SLM (0th order) to be fully diffracted (1st order) for the maximum of the gray level (250). Particularly interesting for the future work is the gray level for which the two orders show equal intensity. (c) Intensity modulation of the 1st order diffracted beam, by shifting the grating pattern on the SLM screen, for period 13.5 and gray level 50.

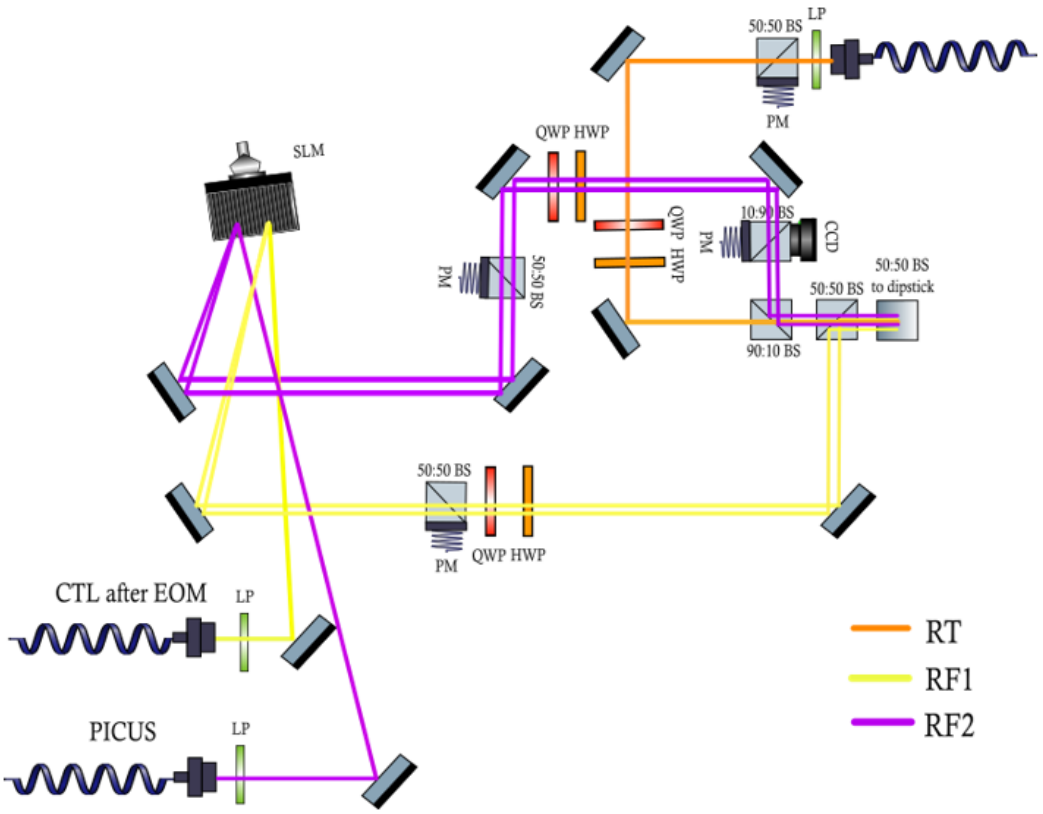

FIGURE E2: Optical setup on top of the breadboard (corresponds to Figure 2.5), with the SLM installed. The setup is adjusted to host two RF paths, for the implementation of the entanglement protocol discussed in Section 6.2.3.1. After preparation to the subradiant state with good fidelity, by the CTL+EOM path, the PICUS laser should apply a short, high-power, off-resonant pulse to induce AC Stark shift and transfer the population to the superradiant state for the readout.

Bibliography

[1] M. **PLANCK**. "On the Law of Distribution of Energy in the Normal Spectrum". *Annalen der Physics* **4**.553 (1901). DOI: 10.1002/andp.19013090310 (cited on p. 1).

[2] G. N. **LEWIS**. "The Conservation of Photons". *Nature* (1926). DOI: 10.1038/118874a0 (cited on p. 1).

[3] A. **EINSTEIN**. "Uber einen die Erzeugung und Verwandlung desLichtes bettrefenden heuristischen Gesichtpunkt". *Annalen der Physik17* (1905). DOI: 10.1002/andp.19053220607 (cited on p. 1).

[4] A. **EINSTEIN**. "Zur Theorie der Lichterzeugung und Lichtabsorption". *Annalen der Physik20* (1906). DOI: 10.1002/andp.19063250613 (cited on p. 1).

[5] L. de **BROGLIE**. "Recherches sur la théorie des quanta, Thèse de doctorat,Paris". *Annales de Physique* **3** (1924), 22–128. DOI: 10.1002/andp.19063250613 (cited on p. 1).

[6] A. **ASPECT**, J. Dalibard, and G. Roger. "Experimental Test of Bell's Inequalities Using Time-Varying Analyzers". *Phys. Rev. Lett.* **49** (25 1982), 1804–1807. DOI: 10.1103/PhysRevLett.49.1804 (cited on p. 1).

[7] B. **HENSEN** et al. "Loophole-free Bell inequality violation using electron spins separated by 1.3 kilometres". *Nature* **526** (7575 2015), 682–6. DOI: 10.1038/nature15759 (cited on p. 1).

[8] J. S. **BELL**. "On the Einstein Podolsky Rosen paradox". *Physics Physique Fizika* **1** (3 1964), 195–200. DOI: 10.1103/PhysicsPhysiqueFizika.1.195 (cited on p. 1).

[9] D. J. **P.** and M. G. J. "Quantum technology: the second quantum revolution". *Phil. Trans. R. Soc.* **A.3611655–1674** (2003). DOI: 10.1098/rsta.2003.1227 (cited on p. 1).

[10] R. **FEYNMAN**. "Simulating physics with computers". *Theor Phys* **Int J 21** (1982), 467–488. DOI: 10.1007/BF02650179 (cited on p. 2).

[11] L. **GROVER**. "From Schrö"dinger's equation to the quantumsearch algorithm". *Pramana* **56** (2001), 333. DOI: 10.1007/s12043-001-0128-3 (cited on p. 2).

[12] P. W. **SHOR**. "Polynomial-Time Algorithms for Prime Factorization and Discrete Logarithms on a Quantum Computer". *SIAM Journal on Computing* **26**.5 (1997), 1484–1509. DOI: 10.1137/S0097539795293172 (cited on p. 2).

[13] J. **O'BRIEN**, A. Furusawa, and J. Vucković'. "Photonic quantum technologies". *Nature Photonics* **3** (2009), 687–695. DOI: 10.1038/nphoton.2009.229 (cited on p. 2).

[14] D. P. **DIVINCENZO**. "The Physical Implementation of Quantum Computation". *Fortschritte der Physik* **48** (2000), 9–11. DOI: 10.1002/1521-3978(200009)48:9/11<771::AID-PROP771>3.0.CO;2-E (cited on p. 3).

[15] R. **KNILL** E.and Laflamme and G. Milburn. "A scheme for efficient quantum computation with linear optics." *Nature* **409** (2001), 46–52. DOI: 10.1038/35051009 (cited on p. 3).

[16] I. **AHARONOVICH**, D. Englund, and M. Toth. "Solid-state single-photon emitters". *Nature Photon* **10** (2016), 631–641. DOI: 10.1038/nphoton.2016.186 (cited on p. 3).

[17] P. **LODAHL**, A. Ludwig, and R. J. Warburton. "A deterministic source of single photons". *Physics Today* **75**.3 (2022), 44–50 (cited on p. 3).

[18] R. **UPPU**, F. T. Pedersen, Y. Wang, C. T. Olesen, C. Papon, X. Zhou, L. Midolo, S. Scholz, A. D. Wieck, A. Ludwig, and P. Lodahl. "Scalable integrated single-photon source". *Sci. Adv.* **6** (50 2020), eabc8268. DOI: 10.1126/sciadv.abc8268 (cited on pp. 3, 33–35).

[19] R **WARBURTON**. "Single spins in self-assembled quantum dots". *Nature Mater* **12** (2013), 483–493. DOI: 10.1038/nmat3585 (cited on pp. 3, 34, 84, 99).

[20] N. H. **LINDNER** and T. Rudolph. "Proposal for Pulsed On-Demand Sources of Photonic Cluster State Strings". *Phys. Rev. Lett.* **103** (11 2009), 113602. DOI: 10.1103/PhysRevLett.103.113602 (cited on p. 3).

[21] R. **RAUSSENDORF** and H. J. Briegel. "A One-Way Quantum Computer". *Phys. Rev. Lett.* **86** (22 2001), 5188–5191. DOI: 10.1103/PhysRevLett.86.5188 (cited on p. 3).

[22] S. **BARTOLUCCI**, P. Birchall, H. Bombín, H. Cable, C. Dawson, M. Gimeno-Segovia, E. Johnston, K. Kieling, M. Nickerson N.and Pant, F. Pastawski, T. Rudolph, and C. Sparrow. "Fusion-based quantum computation". *Nat Commun* **14** (912 2023). DOI: 10.1038/s41467-023-36493-1 (cited on p. 3).

[23] S. **PAESANI** and B. J. Brown. "High-Threshold Quantum Computing by Fusing One-Dimensional Cluster States". *Phys. Rev. Lett.* **131** (12 2023), 120603. DOI: 10.1103/PhysRevLett.131.120603 (cited on p. 3).

[24] P. **HILAIRE**, L. Vidro, H. S. Eisenberg, and S. E. Economou. "Near-deterministic hybrid generation of arbitrary photonic graph states using a single quantum emitter and linear optics". *Quantum* **7** (2023). DOI: 10.22331/q-2023-04-27-992 (cited on p. 3).

[25] M. **VARNAVA**, D. E. Browne, and T. Rudolph. "Loss Tolerance in One-Way Quantum Computation via Counterfactual Error Correction". *Phys. Rev. Lett.* **97** (12 2006), 120501. DOI: 10.1103/PhysRevLett.97.120501 (cited on p. 3).

[26] S. E. **ECONOMOU**, N. Lindner, and T. Rudolph. "Optically Generated 2-Dimensional Photonic Cluster State from Coupled Quantum Dots". *Phys. Rev. Lett.* **105** (9 2010), 093601. DOI: 10.1103/PhysRevLett.105.093601 (cited on pp. 4, 68, 97, 101).

[27] M. **GULLANS**, T. G. Tiecke, D. E. Chang, J. Feist, J. D. Thompson, J. I. Cirac, P. Zoller, and M. D. Lukin. "Nanoplasmonic Lattices for Ultracold Atoms". *Phys. Rev. Lett.* **109** (23 2012), 235309. DOI: 10.1103/PhysRevLett.109.235309 (cited on pp. 4, 82, 95, 101).

[28] H. **KIMBLE**. "The quantum internet". *Nature* **453** (2008), 1023–1030. DOI: 10.1038/nature07127 (cited on p. 4).

[29] H.-J. **BRIEGEL**, W. Dür, J. I. Cirac, and P. Zoller. "Quantum Repeaters: The Role of Imperfect Local Operations in Quantum Communication". *Phys. Rev. Lett.* **81** (26 1998), 5932–5935. DOI: 10.1103/PhysRevLett.81.5932 (cited on p. 4).

[30] L. **DUAN**, M. Lukin, J. Cirac, and P. Zoller. "Long-distance quantum communication with atomic ensembles and linear optics". *Nature* **414** (2001), 413–418. DOI: 10.1038/35106500 (cited on p. 4).

[31] K. **AZUMA**, K. Tamaki, and H. Lo. "All-photonic quantum repeaters". *Nat Commun* **6** (2015), 6787. DOI: 10.1038/ncomms7787 (cited on p. 4).

[32] D. **BUTERAKOS**, E. Barnes, and S. E. Economou. "Deterministic Generation of All-Photonic Quantum Repeaters from Solid-State Emitters". *Phys. Rev. X* **7** (4 2017), 041023. DOI: 10.1103/PhysRevX.7.041023 (cited on pp. 4, 97).

[33] J. **BORREGAARD**, H. Pichler, T. Schröder, M. D. Lukin, P. Lodahl, and A. S. Sørensen. "One-Way Quantum Repeater Based on Near-Deterministic Photon-Emitter Interfaces". *Phys. Rev. X* **10** (2 2020), 021071. DOI: 10.1103/PhysRevX.10.021071 (cited on pp. 4, 97).

[34] A. **ASENJO-GARCIA**, M. Moreno-Cardoner, A. Albrecht, H. J. Kimble, and D. E. Chang. "Exponential Improvement in Photon Storage Fidelities Using Subradiance and "Selective Radiance" in Atomic Arrays". *Phys. Rev. X* **7** (3 2017), 031024. DOI: 10.1103/PhysRevX.7.031024 (cited on pp. 4, 10, 18, 20, 21, 68, 97, 98).

[35] R. H. **DICKE**. "Coherence in Spontaneous Radiation Processes". *Phys. Rev.* **93** (1 1954), 99–110. DOI: 10.1103/PhysRev.93.99 (cited on pp. 4, 8, 13, 17).

[36] M. **GROSS** and S. Haroche. "Superradiance: An essay on the theory of collective spontaneous emission". *Physics Reports* **93**.5 (1982), 301–

396. DOI: https://doi.org/10.1016/0370-1573(82)90102-8 (cited on pp. 4, 8, 10–12).

[37] R. G. **DEVOE** and R. G. Brewer. "Observation of Superradiant and Subradiant Spontaneous Emission of Two Trapped Ions". *Phys. Rev. Lett.* **76** (12 1996), 2049–2052. DOI: 10.1103/PhysRevLett.76.2049 (cited on pp. 4, 10).

[38] J. **RUI**, D. Wei, A. Rubio-Abadal, S. Hollerith, J. Zeiher, D. M. Stamper-Kurn, C. Gross, and I. Bloch. "A subradiant optical mirror formed by a single structured atomic layer". *Nature* **583** (2020), 369–374. DOI: 10.1038/s41586-020-2463-x (cited on p. 4).

[39] G. **FERIOLI**, A. Glicenstein, L. Henriet, I. Ferrier-Barbut, and A. Browaeys. "Storage and Release of Subradiant Excitations in a Dense Atomic Cloud". *Phys. Rev. X* **11** (2 2021), 021031. DOI: 10.1103/PhysRevX.11.021031 (cited on pp. 4, 9, 10, 68).

[40] A. **GLICENSTEIN**, G. Ferioli, A. Browaeys, and I. Ferrier-Barbut. "From superradiance to subradiance: exploring the many-body Dicke ladder". *Opt. Lett.* **47**.6 (2022), 1541–1544. DOI: 10.1364/OL.451903 (cited on pp. 4, 9, 10).

[41] M. **SCHEIBNER**, T. Schmidt, L. Worschech, F. A., G. Bacher, T. Passow, and D. Hommel. "Superradiance of quantum dots". *Nature Phys* **3** (2007), 106–110. DOI: 10.1038/nphys494 (cited on p. 4).

[42] A. F. van **LOO**, A. Fedorov, K. Lalumière, B. C. Sanders, A. Blais, and A. Wallraff. "Photon-Mediated Interactions Between Distant Artificial Atoms". *Science* **342**.6165 (2013), 1494–1496. DOI: 10.1126/science.1244324 (cited on pp. 4, 5, 10, 57).

[43] C. **BRADAC**, M. Johnsson, M. Breugel, B. Baragiola, R. Martin, M. Juan, G. Brennen, and T. Volz. "Room-temperature spontaneous superradiance from single diamond nanocrystals". *Nat Commun* **8** (2017), 1205. DOI: 10.1038/s41467-017-01397-4 (cited on p. 4).

[44] R. E. **EVANS**, M. K. Bhaskar, D. D. Sukachev, C. T. Nguyen, A. Sipahigil, M. J. Burek, B. Machielse, G. H. Zhang, A. S. Zibrov, E. Bielejec, H. Park, M. Lončar, and M. D. Lukin. "Photon-mediated interactions between quantum emitters in a diamond nanocavity". *Science* **362**.6415 (2018), 662–665. DOI: 10.1126/science.aau4691 (cited on pp. 4, 5, 10).

[45] G. **FERIOLI**, A. Glicenstein, F. Robicheaux, R. T. Sutherland, A. Browaeys, and I. Ferrier-Barbut. "Laser-Driven Superradiant Ensembles of Two-Level Atoms near Dicke Regime". *Phys. Rev. Lett.* **127** (24 2021), 243602. DOI: 10.1103/PhysRevLett.127.243602 (cited on pp. 4, 10).

[46] M. **ZANNER**, T. Orell, C. M. F. Schneider, R. Albert, S. Oleschko, M. L. Juan, M. Silveri, and G. Kirchmair. "Coherent control of a multi-qubit dark state in waveguide quantum electrodynamics".

Nat. Phys. **18** (2022), 538–543. DOI: 10.1038/s41567-022-01527-w (cited on pp. 5, 10, 99).

[47] P. **LODAHL**, S. Mahmoodian, and S. Stobbe. "Interfacing single photons and single quantum dots with photonic nanostructures". *Rev. Mod. Phys.* **87** (2 2015), 347–400. DOI: 10.1103/RevModPhys.87.347 (cited on pp. 5, 21, 23, 27, 31, 32, 45, 61, 67, 81, 93).

[48] X.-L. **CHU**, V. Angelopoulou, P. Lodahl, and N. Rotenberg. "Subradiant states for imperfect quantum emitters coupled by a nanophotonic waveguide". *Phys. Rev. A* **106** (2022). DOI: 10.1103/PhysRevA.106.053702 (cited on pp. 5, 10, 20, 58).

[49] A. **GONZALEZ-TUDELA**, D. Martin-Cano, E. Moreno, L. Martin-Moreno, C. Tejedor, and F. J. Garcia-Vidal. "Entanglement of Two Qubits Mediated by One-Dimensional Plasmonic Waveguides". *Phys. Rev. Lett.* **106** (2 2011), 020501. DOI: 10.1103/PhysRevLett.106.020501 (cited on p. 5).

[50] D. **DZSOTJAN**, A. S. Sørensen, and M. Fleischhauer. "Quantum emitters coupled to surface plasmons of a nanowire: A Green's function approach". *Phys. Rev. B* **82** (7 2010), 075427. DOI: 10.1103/PhysRevB.82.075427 (cited on pp. 5, 18).

[51] J.-H. **KIM**, S. Aghaeimeibodi, C. J. K. Richardson, R. P. Leavitt, and E. Waks. "Super-Radiant Emission from Quantum Dots in a Nanophotonic Waveguide". *Nano Lett.* **18** (2018), 4734-4740. DOI: 10.1021/acs.nanolett.8b01133 (cited on pp. 5, 73, 76, 81, 94, 95).

[52] J. Q. **GRIM**, A. S. Bracker, M. Zalalutdinov, S. G. Carter, A. C. Kozen, M. Kim, C. S. Kim, J. T. Mlack, M. Yakes, B. Lee, and D. Gammon. "Scalable in operando strain tuning in nanophotonic waveguides enabling three-quantum-dot superradiance". *Nat. Mat.* **18** (2019), 963–969. DOI: 10.1038/s41563-019-0418-0 (cited on pp. 5, 10, 73, 76, 81, 94, 95).

[53] J. Q. **GRIM**, I. Welland, S. G. Carter, A. S. Bracker, A. Yeats, C. S. Kim, M. Kim, K. Tran, I. Vurgaftman, and T. L. Reinecke. "Scattering laser light from two resonant quantum dots in a photonic crystal waveguide". *Phys. Rev. B* **106** (8 2022), L081403. DOI: 10.1103/PhysRevB.106.L081403 (cited on p. 5).

[54] Z. X. **KOONG**, M. Cygorek, E. Scerri, T. S. Santana, S. I. Park, J. D. Song, E. M. Gauger, and B. D. Gerardot. "Coherence in cooperative photon emission from indistinguishable quantum emitters". *Sci. Adv.* **8** ((11) 2022). DOI: 10.1126/sciadv.abm8171 (cited on pp. 5, 9, 73, 76, 81, 94–96).

[55] M. **CYGOREK**, E. D. Scerri, T. S. Santana, Z. X. Koong, B. D. Gerardot, and E. M. Gauger. "Signatures of cooperative emission in photon coincidence: Superradiance versus measurement-induced cooperativity". *Phys. Rev. A* **107** (2 2023), 023718. DOI: 10.1103/PhysRevA.107.023718 (cited on pp. 5, 9, 10, 16, 76, 85, 94, 96).

[56] A. **TIRANOV**, V. Angelopoulou, C. J. van Diepen, B. Schrinski, O. A. D. Sandberg, Y. Wang, L. Midolo, S. Scholz, A. D. Wieck, A. Ludwig, A. S. Sørensen, and P. Lodahl. "Collective super- and subradiant dynamics betweendistant optical quantum emitters". *Science* **379** (2023), 389–393. DOI: 10.1126/science.ade932 (cited on pp. 7, 21, 61, 66).

[57] O. A. **DALL' ALBA SANDBERG**. *Quantum: Illuminated, Theory of light-matter interaction for quantum enhanced technologies*. 2023, PhD Thesis (cited on pp. 7, 18, 21, 64, 83, 95).

[58] M. G. **BENEDICT**, A. M. Ermolaev, V. A. Malyshev, I. V. Sokolov, and E. D. Trifonov. *Super-Radiance: Multiatomic Coherent Emission*. CRC Press, 1996 (cited on pp. 8–10).

[59] S. **MASSON** and A. Asenjo-Garcia. "Universality of Dicke superradiance in arrays of quantum emitters". *Nat Commun* **13** (2022), 2285. DOI: https://doi.org/10.1038/s41467-022-29805-4 (cited on pp. 9, 10, 22).

[60] D. R. **PASCHOTTA**. *Superfluorescence*. URL: https://www.rp-photonics.com/superfluorescence.html (cited on p. 9).

[61] R. T. **SUTHERLAND** and F. Robicheaux. "Collective dipole-dipole interactions in an atomic array". *Phys. Rev. A* **94** (1 2016), 013847. DOI: 10.1103/PhysRevA.94.013847 (cited on pp. 9, 10).

[62] W. **GUERIN**, M. O. Araújo, and R. Kaiser. "Subradiance in a Large Cloud of Cold Atoms". *Phys. Rev. Lett.* **116** (8 2016), 083601. DOI: 10.1103/PhysRevLett.116.083601 (cited on p. 9).

[63] D. **DAS**, B. Lemberger, and D. D. Yavuz. "Subradiance and superradiance-to-subradiance transition in dilute atomic clouds". *Phys. Rev. A* **102** (4 2020), 043708. DOI: 10.1103/PhysRevA.102.043708 (cited on p. 9).

[64] A. **CIPRIS**, N. A. Moreira, T. S. do Espirito Santo, P. Weiss, C. J. Villas-Boas, R. Kaiser, W. Guerin, and R. Bachelard. "Subradiance with Saturated Atoms: Population Enhancement of the Long-Lived States". *Phys. Rev. Lett.* **126** (10 2021), 103604. DOI: 10.1103/PhysRevLett.126.103604 (cited on p. 9).

[65] K. **LALUMIÈRE**, B. C. Sanders, A. F. van Loo, A. Fedorov, A. Wallraff, and A. Blais. "Input-output theory for waveguide QED with an ensemble of inhomogeneous atoms". *Phys. Rev. A* **88** (2013). DOI: 10.1103/PhysRevA.88.043806 (cited on pp. 10, 20–22, 58).

[66] A. **GOBAN**, C.-L. Hung, J. D. Hood, S.-P. Yu, J. A. Muniz, O. Painter, and H. J. Kimble. "Superradiance for Atoms Trapped along a Photonic Crystal Waveguide". *Phys. Rev. Lett.* **115** (6 2015), 063601. DOI: 10.1103/PhysRevLett.115.063601 (cited on p. 10).

[67] M. O. **SCULLY** and A. A. Svidzinsky. "The Super of Superradiance". *Science* **325**.5947 (2009), 1510–1511. DOI: 10.1126/science.1176695 (cited on p. 10).

[68] J. A. **MLYNEK**, A. A. Abdumalikov, C. Eichler, and A. Wallraff. "Observation of Dicke superradiance for two artificial atoms in a cavity with high decay rate". *Nat. Com.* **5** (2014). DOI: 10.1038/ncomms6186 (cited on p. 10).

[69] J. G. **BOHNET**, Z. Chen, J. M. Weiner, D. Meiser, M. J. Holland, and J. K. Thompson. "A steady-state superradiant laser with less than one intracavity photon". *Nature* **484** (2012), 78–81. DOI: 10.1038/nature10920 (cited on p. 10).

[70] I. E. **PROTSENKO**, A. V. Uskov, E. C. André, J. Mørk, and M. Wubs. "Quantum Langevin approach for superradiant nanolasers". *New Journal of Physics* **23**.6 (2021), 063010. DOI: 10.1088/1367-2630/abfd4c (cited on p. 10).

[71] V. **PAULISCH**, M. Perarnau-Llobet, A. González-Tudela, and J. I. Cirac. "Quantum metrology with one-dimensional superradiant photonic states". *Phys. Rev. A* **99** (4 2019), 043807. DOI: 10.1103/PhysRevA.99.043807 (cited on pp. 10, 97).

[72] M. **TANG**, S. A. Schäffer, A. A. Jørgensen, M. R. Henriksen, B. T. R. Christensen, J. H. Müller, and J. W. Thomsen. "Cavity-immune spectral features in the pulsed superradiant crossover regime". *Phys. Rev. Res.* **3** (3 2021), 033258. DOI: 10.1103/PhysRevResearch.3.033258 (cited on p. 10).

[73] A. T. **BLACK**, J. K. Thompson. "On-Demand Superradiant Conversion of Atomic Spin Gratings into Single Photons with High Efficiency". *Phys. Rev. Lett.* **95** (13 2005), 133601. DOI: 10.1103/PhysRevLett.95.133601 (cited on p. 10).

[74] A. **ALBRECHT**, L. Henriet, A. Asenjo-Garcia, P. B Dieterle, O. Painter, and D. E Chang. "Subradiant states of quantum bits coupled to a one-dimensional waveguide". *New J. Phys.* **21** (13 2019), 025003. DOI: 10.1088/1367-2630/ab0134 (cited on pp. 10, 21).

[75] G. **FACCHINETTI**, S. D. Jenkins, and J. Ruostekoski. "Storing Light with Subradiant Correlations in Arrays of Atoms". *Phys. Rev. Lett.* **117** (24 2016), 243601. DOI: 10.1103/PhysRevLett.117.243601 (cited on p. 10).

[76] M. **MIRHOSSEINI**, E. Kim, X. Zhang, A. Sipahigil, P. B. Dieterle, A. J. Keller, A. Asenjo-Garcia, D. E. Chang, and O. Painter. "Cavity quantum electrodynamics with atom-like mirrors". *Nature* **569** (13 2019), 692–697. DOI: 10.1038/s41586-019-1196-1 (cited on p. 10).

[77] J. **TREBBIA**, Q. Deplano, P. Tamarat, and B. Lounis. "Tailoring the superradiant and subradiant nature of two coherently coupled

quantum emitters". *Nat. Commun.* **13** (13 2022), 133601. DOI: 10.1038/s41467-022-30672-2 (cited on p. 10).

[78] M. J. **KASTORYANO**, F. Reiter, and A. S. Sørensen. "Dissipative Preparation of Entanglement in Optical Cavities". *Phys. Rev. Lett.* **106** (9 2011), 090502. DOI: 10.1103/PhysRevLett.106.090502 (cited on pp. 14, 95, 99, 100).

[79] E. C. G. **SUDARSHAN** and B. Misra. "The Zeno's paradox in quantum theory". *J. Math. Phys.* **18** (13 1977), 756–763. DOI: 10.1063/1.523304 (cited on pp. 14, 82).

[80] T. **GRUNER** and D.-G. Welsch. "Green-function approach to the radiation-field quantization for homogeneous and inhomogeneous Kramers-Kronig dielectrics". *Phys. Rev. A* **53** (3 1996), 1818–1829. DOI: 10.1103/PhysRevA.53.1818 (cited on p. 18).

[81] A. **ASENJO-GARCIA**, J. D. Hood, D. E. Chang, and H. J. Kimble. "Atom-light interactions in quasi-one-dimensional nanostructures: A Green's-function perspective". *Phys. Rev. A* **95** (3 2017), 033818. DOI: 10.1103/PhysRevA.95.033818 (cited on pp. 18, 19, 22).

[82] R. **RÖHLSBERGER**, K. Schlage, B. Sahoo, S. Couet, and R. Rüffer. "Collective Lamb Shift in Single-Photon Superradiance". *Science* **328**.5983 (13 2010), 1248–1251. DOI: 10.1126/science.1187770 (cited on p. 20).

[83] K. **MØLMER**, Y. Castin, and J. Dalibard. "Monte Carlo wavefunction method in quantum optics". *J. Opt. Soc. Am.* **B 10** (13 1993), 524–538. DOI: 10.1364/JOSAB.10.000524 (cited on p. 24).

[84] D. **NAJER**. *A coherent light-matter interface with a semiconductor quantum dot in an optical microcavity*. 2019. DOI: .. URL: https://edoc.unibas.ch/71293/1/najer_thesis_EDOC.pdf (cited on p. 28).

[85] C. **PAPON**. *Photonic circuits with multiple quantum dots -Towards scalable operation of deterministic single-photon sources*. 2023. DOI: .. URL: https://nbi.ku.dk/english/theses/phd-theses/camille-papon/ (cited on pp. 28, 45, 48, 61, 93, 97).

[86] M. **BAYER**, G. Ortner, O. Stern, A. Kuther, A. A. Gorbunov, A. Forchel, P. Hawrylak, S. Fafard, K. Hinzer, T. L. Reinecke, S. N. Walck, J. P. Reithmaier, F. Klopf, and F. Schäfer. "Fine structure of neutral and charged excitons in self-assembled In(Ga)As/(Al)GaAs quantum dots". *Phys. Rev. B* **65** (19 2002), 195315. DOI: 10.1103/PhysRevB.65.195315 (cited on pp. 29, 48).

[87] M. **HAYHURST APPEL**. *A Quantum Dot Source of Time-Bin Multi-Photon Entanglement*. 2021. DOI: .. URL: https://nbi.ku.dk/english/theses/phd-theses/martin-hayhurst-appel/ (cited on pp. 30, 38, 39, 79).

[88] M. **ARCARI**, I. Söllner, A. Javadi, S. Lindskov Hansen, S. Mahmoodian, J. Liu, H. Thyrrestrup, E. H. Lee, J. D. Song, S. Stobbe,

and P. Lodahl. "Near-Unity Coupling Efficiency of a Quantum Emitter to a Photonic Crystal Waveguide". *Phys. Rev. Lett.* **113** (9 2014), 093603. DOI: 10.1103/PhysRevLett.113.093603 (cited on pp. 31, 33).

[89] S. **HUGHES**, L. Ramunno, J. F. Young, and J. E. Sipe. "Extrinsic Optical Scattering Loss in Photonic Crystal Waveguides: Role of Fabrication Disorder and Photon Group Velocity". *Phys. Rev. Lett.* **94** (3 2005), 033903. DOI: 10.1103/PhysRevLett.94.033903 (cited on p. 32).

[90] A. **JAVADI**, S. Mahmoodian, I. Söllner, and P. Lodahl. "Numerical modeling of the coupling efficiency of single quantum emitters in photonic-crystal waveguides". *Opt. Soc. Am. B* **35** (13 2018), 514–522. DOI: 10.1364/JOSAB.35.000514 (cited on pp. 32, 45, 67).

[91] F. **LIU**, A. Brash, J. O'Hara, L. Martins, C. Phillips, R. Coles, B. Royall, E. Clarke, C. Bentham, N. Prtljaga, I. Itskevich, L. Wilson, M. Skolnick, and A. Fox. "High Purcell factor generation of indistinguishable on-chip single photons". *Nat Nanotechnol* **13** (9 2018), 835–840. DOI: 10.1038/s41565-018-0188-x (cited on p. 33).

[92] M. C. **LÖBL**, S. Scholz, J. R. I. Söllner, T. Denneulin, A. Kovács, B. E. Kardynał, A. D. Wieck, A. Ludwig, and R. J. Warburton. "Excitons in InGaAs quantum dots without electron wetting layer states." *Commun Phys* **2** (93 2019), 133601. DOI: 10.1038/s42005-019-0194-9 (cited on p. 33).

[93] Y. **WANG**. *Novel nanofabrication methods and processes for quantum photonic integrated circuits*. 2021. DOI: .. URL: https://nbi.ku.dk/english/theses/phd-theses/ying-wang/Ying-Wang__compressed_.pdf (cited on p. 35).

[94] X. **ZHOU**, I. Kulkova, T. Lund-Hansen, S. Lindskov Hansen, P. Lodahl, and L. Midolo. "High-efficiency shallow-etched grating on GaAs membranes for quantum photonic applications". *Appl. Phys. Lett.* **13** (25 2018), 251103. DOI: 10.1063/1.5055622 (cited on p. 35).

[95] R. J. **YOUNG**, R. M. Stevenson, A. J. Shields, P. Atkinson, K. Cooper, D. A. Ritchie, K. M. Groom, A. I. Tartakovskii, and M. S. Skolnick. "Inversion of exciton level splitting in quantum dots". *Phys. Rev. B* **72** (11 2005), 113305. DOI: 10.1103/PhysRevB.72.113305 (cited on p. 35).

[96] F. **THILDE-PEDERSEN**. *Deterministic Single and Multi-Photon Sources with quantum dots in Planar Nanostructures*. 2020. DOI: .. URL: https://nbi.ku.dk/english/theses/phd-theses/freja-thilde-pedersen/FrejaThildePedersen.pdf (cited on pp. 39–41).

[97] F. **PEDERSEN**, Y. Wang, C. T. Olesen, S. Scholz, A. D. Wieck, A. Ludwig, M. C. Löbl, R. J. Warburton, L. Midolo, R. Uppu, and P. Lodahl. "Near Transform-Limited Quantum Dot Linewidths in a Broadband Photonic Crystal Waveguide". *ACS Photonics* **7** (9 2020), 2343–2349. DOI: 10.1021/acsphotonics.0c00758 (cited on pp. 45, 98).

[98] T. **PREGNOLATO**, X.-L. Chu, R. Schott, A. D. Wieck, A. Ludwig, P. Lodahl, and N. Rotenberg. "Deterministic positioning of nanophotonic waveguides around single self-assembled quantum dots". *APL Photonics* **5** (13 2020), 086101. DOI: 10.1063/1.5117888 (cited on pp. 45, 97, 98).

[99] D. **SCHUH**, J. Bauer, E. Uccelli, R. Schulz, A. Kress, F. Hofbauer, J. Finley, and G. Abstreiter. "Controlled positioning of self-assembled InAs quantum dots on (110) GaAs". *Physica E: Low-dimensional Systems and Nanostructures* **26** (1-4 2001), 72–76. DOI: 10.1016/j.physe.2004.08.026 (cited on p. 45).

[100] B. **GERARDOT**, G. Subramanian, S. Minvielle, H. Lee, J. Johnson, W. Schoenfeld, D. Pine, J. Speck, and P. Petroff. "Self-assembling quantum dot lattices through nucleation site engineering". *Journal of Crystal Growth* **236** (4 2002), 72–76. DOI: 10.1016/S0022-0248(02)00849-7 (cited on pp. 45, 76).

[101] M. K. **YAKES**, L. Yang, A. S. Bracker, T. M. Sweeney, P. G. Brereton, M. Kim, C. S. Kim, P. M. Vora, D. Park, S. G. Carter, and D. Gammon. "Leveraging Crystal Anisotropy for Deterministic Growth of InAs Quantum Dots with Narrow Optical Linewidths". *Nano Letters* **13** (10 2013), 4870–4875. DOI: 10.1021/nl402744s (cited on p. 45).

[102] H. **THYRRESTRUP**, G. Kiršanskė, H. Le Jeannic, P. T., L. Zhai, L. Raahauge L.and Midolo, N. Rotenberg, A. Javadi, R. Schott, A. D. Wieck, A. Ludwig, M. C. Löbl, I. Söllner, R. J. Warburton, and P. Lodahl. "Quantum Optics with Near-Lifetime-Limited Quantum-Dot Transitions in a Nanophotonic Waveguide". *Nano Letters* **18** (10 2018), 1801–1806. DOI: 10.1021/acs.nanolett.7b05016 (cited on pp. 45, 46).

[103] H. **LE JEANNIC**, T. Ramos, S. F. Simonsen, T. Pregnolato, Z. Liu, R. Schott, A. D. Wieck, A. Ludwig, N. Rotenberg, J. J. García-Ripoll, and P. Lodahl. "Experimental Reconstruction of the Few-Photon Nonlinear Scattering Matrix from a Single Quantum Dot in a Nanophotonic Waveguide". *Phys. Rev. Lett.* **126** (2 2021), 023603. DOI: 10.1103/PhysRevLett.126.023603 (cited on pp. 46, 89).

[104] X.-L. **CHU**, C. Papon, N. Bart, A. D. Wieck, A. Ludwig, L. Midolo, N. Rotenberg, and P. Lodahl. "Independent Electrical Control of Two Quantum Dots Coupled through a Photonic-Crystal Waveguide". *Phys. Rev. Lett.* **131** (3 2023), 033606. DOI: 10.1103/PhysRevLett.131.033606 (cited on pp. 48, 98).

[105] J. H. **PRECHTEL**, F. Maier, J. Houel, A. V. Kuhlmann, A. Ludwig, A. D. Wieck, D. Loss, and R. J. Warburton. "Electrically tunable hole g factor of an optically active quantum dot for fast spin rotations". *Phys. Rev. B* **91** (16 2015), 165304. DOI: 10.1103/PhysRevB.91.165304 (cited on p. 48).

[106] M. **MINKOV** and V. Savona. "Long-distance radiative excitation transfer between quantum dots in disordered photonic crystal waveguides". *Phys. Rev. B* **88** (8 2013), 081303. DOI: 10.1103/PhysRevB.88.081303 (cited on p. 61).

[107] O. A. D. **SANDBERG**, B. Schrinski, A. Tiranov, V. Angelopoulou, C. J. van Diepen, P. Lodahl, and A. S. Sørensen. "Master equation description of collective super- and subradiance from coupled quantum dots". *In preparation* **95** (13 2005), 133601. DOI: 10.1103/PhysRevLett.95.133601 (cited on p. 63).

[108] V. E. **ELFVING**, S. Das, and A. S. Sørensen. "Enhancing quantum transduction via long-range waveguide-mediated interactions between quantum emitters". *Phys. Rev. A* **100** (5 2019), 053843. DOI: 10.1103/PhysRevA.100.053843 (cited on p. 68).

[109] C. J. van **DIEPEN** and et al. *In preparation*. 2024. DOI: 10.1103/PhysRevLett.95.133601. URL: https://link.aps.org/doi/10.1103/PhysRevLett.95.133601 (cited on pp. 71, 99).

[110] R. **BROWN** and R. Twiss. "Correlation between Photons in two Coherent Beams of Light". *Nature* **177** (13 1956), 27–29. DOI: 10.1038/177027a0 (cited on p. 75).

[111] A. **SIPAHIGIL** et al. "An integrated diamond nanophotonics platform for quantum-optical networks". *Science* **354**.6314 (13 2016), 847–850. DOI: 10.1126/science.aah6875 (cited on p. 75).

[112] S. **WOLF**, S. Richter, J. von Zanthier, and F. Schmidt-Kaler. "Light of Two Atoms in Free Space: Bunching or Antibunching?" *Phys. Rev. Lett.* **124** (6 2020), 063603. DOI: 10.1103/PhysRevLett.124.063603 (cited on p. 76).

[113] X.-L. **CHU**, C. Papon, N. Bart, A. D. Wieck, A. Ludwig, L. Midolo, N. Rotenberg, and P. Lodahl. "Independent Electrical Control of Two Quantum Dots Coupled through a Photonic-Crystal Waveguide". *Phys. Rev. Lett.* **131** (3 2023), 033606. DOI: 10.1103/PhysRevLett.131.033606 (cited on p. 79).

[114] S. **KAKO**, C.Santori, K. Hoshino, S. G Otzinger, Y. Yamamoto, and Y. Arakawa. "A gallium nitride single-photon source operating at 200 K". *Nat. Mat.* **5** (13 2006), 887–892. DOI: https://doi.org/10.1038/nmat1763 (cited on p. 80).

[115] D. **CHANG**, V. Vuletić, and M. Lukin. "Quantum nonlinear optics — photon by photon". *Nature Photon* **8** (13 2014), 685–694. DOI: 10.1038/nphoton.2014.192 (cited on p. 97).

[116] B. **SCHRINSKI** and A. S. Sørensen. "Polariton interaction in one-dimensional arrays of atoms coupled to waveguides". *Phys. Rev. Lett.* **95** (13 2021), 133601. DOI: 10.48550/arXiv.2110.15878 (cited on pp. 97, 98).

[117] H. **OLLIVIER** et al. "Reproducibility of High-Performance Quantum Dot Single-Photon Sources". *ACS Photonics* **7** (4 2020), 133601. DOI: 10.1021/acsphotonics.9b01805 (cited on pp. 97, 98).

[118] R. **BENEVIDES**, M. Ménard, G. S. Wiederhecker, and T. P. M. Alegre. "Ar/Cl2 etching of GaAs optomechanical microdisks fabricated with positive electroresist". *Opt. Mater. Express* **10**.1 (13 2020), 57–67. DOI: 10.1364/OME.10.000057 (cited on p. 97).

[119] J. **HANSOM**, C. H. H. Schulte, C. Matthiesen, M. J. Stanley, and M. Atatüre. "Frequency stabilization of the zero-phonon line of a quantum dot via phonon-assisted active feedback". *Appl. Phys. Lett.s* **105** (13 2014), 172107. DOI: 10.1063/1.49010457 (cited on p. 98).

[120] D. **MARTÍN-CANO**, A. González-Tudela, L. Martín-Moreno, F. J. García-Vidal, C. Tejedor, and E. Moreno. "Dissipation-driven generation of two-qubit entanglement mediated by plasmonic waveguides". *Phys. Rev. B* **84** (23 2011), 235306. DOI: 10.1103/PhysRevB.84.235306 (cited on p. 99).

[121] C. **CHOU**, H. de Riedmatten, D. Felinto, S. Polyakov, S. van Enk, and H. Kimble. "Measurement-induced entanglement for excitation stored in remote atomic ensembles". *Nature* **438** (13 2005), 828–832. DOI: 10.1038/nature04353 (cited on p. 100).

[122] M. H. **APPEL**, A. Tiranov, S. Pabst, M. L. Chan, C. Starup, Y. Wang, L. Midolo, K. Tiurev, S. Scholz, A. D. Wieck, A. Ludwig, A. S. Sørensen, and P. Lodahl. "Entangling a Hole Spin with a Time-Bin Photon: A Waveguide Approach for Quantum Dot Sources of Multiphoton Entanglement". *Phys. Rev. Lett.* **128** (23 2022), 233602. DOI: 10.1103/PhysRevLett.128.233602 (cited on p. 100).

[123] M. H. **APPEL**, A. Tiranov, A. Javadi, M. C. Löbl, Y. Wang, S. Scholz, A. D. Wieck, A. Ludwig, R. J. Warburton, and P. Lodahl. "Coherent Spin-Photon Interface with Waveguide Induced Cycling Transitions". *Phys. Rev. Lett.* **126** (1 2021), 013602. DOI: 10.1103/PhysRevLett.126.013602 (cited on p. 100).